Πανεπιστήμιο Κρήτης
Σχολή Θετικών και Τεχνολογικών Επιστημών
Τμήμα Φυσικής

Μ.Π.Σ

Μικροηλεκτρονικής- Οπτοηλεκτρονικής

‘ Πολυφασματικός Διαχωρισμός τρισδιάστατων εικόνων φθορισμού ’

Σημαντηράκη Μαρία

Ηράκλειο 2009

University of Crete

Physics Department

Master of:

Microelectronic- Optoelectronic

"Multispectral Decomposition of 3D Fluorescence Tomography Data"

Maria Simantiraki

Heraklion 2009

Advisor: Giannis Zacharakis

Supervisor: Jorge Lorenzo Ripoll.

Abstract

Fluorescence Molecular Tomography (FMT) is a well established method of acquiring three dimensional fluorescence images. Based on the principles of the diffuse optical tomography (DOT) it extracts tomographic images from non contact measurements, when investigated sample carries at least one fluorescence target. In the case of two or more fluorophores the spectrum that will be recorded by the detection channel is a linear combination of the individual components.

In this study we present the different unmixing strategies that can be followed in order to separate the fluorescence signal of two overlapping fluorophores. Many of the most useful proteins such as GFP or DsRed have strongly overlapping emission spectra and hence it is not easy to separate them only with the use of filters. However, with the use of tissue-like phantoms with overlapping spectra, we would try to separate them in two different ways and two different modes. Generally, the unmixing processing is a linear algorithm that determine the contribution of each one of the fluorophore that exist simultaneously in the under examination sample, to the total signal. Therefore, in this way we can isolate the signal that we want to examine from the other signals that exist in the same detection area.

In order to do the unmixing process we have used two different dyes CFSE and Atto590, since we already know that their spectral is overlapping. We excited them at two wavelengths (514.5nm and 488nm), and continuously, using a spectrograph and the FMT setup we tried to separate the mixed signal that we recorded. The first way was by applying the unmixing algorithm in the already reconstruction data and the other way was by applying firstly the unmixing algorithm and them reconstructed the raw data. In both cases we used two different kinds of algorithms referring to the spectral strengths that are used. In this way we found that the unmixing in the reconstructed data is the most accurately way of unmixing.

Περίληψη

Η βασική μέθοδος για να αποκτήσουμε images σε τρεις διαστάσεις είναι με την χρήση της fluorescence molecular tomography (FMT). Μια μέθοδος από απόσταση που χρησιμοποιεί ως βάση τις αρχές της οπτικής τομογραφίας διάχυσης (DOT) και φθορίζουσες ουσίες ως μέσο ανίχνευσης. Στην περίπτωση που υπάρχουν όμως δυο χρωστικές ταυτόχρονα στο δείγμα, το σήμα το οποίο θα καταγράψει η κάμερα μας στο κανάλι ανίχνευσης θα περιέχει σήμα και από τις δυο χρωστικές.

Στην εργασία αυτή θα παρουσιάσουμε διαφορετικές μεθόδους που μπορούμε να χρησιμοποιήσουμε για να διαχωρίσουμε το φθορίζον σήμα που προέρχεται από δυο χρωστικές. Γενικά πολλές από τις γνωστές πρωτεΐνες όπως το GFP ή το Ds Red έχουν φθορίζοντα φάσματα, τα οποία αν χρησιμοποιηθούν μαζί αλληλεπικαλύπτονται. Γι'αυτο το λόγο είναι και πολύ δύσκολο να τις ξεχωρίσουμε μόνο με την χρήση των φίλτρων. Για να μπορέσουμε να τις διαχωρίσουμε θα χρησιμοποιήσουμε κατάλληλα δείγματα που ονομάζονται phantoms τα οποία θα αποτελούνται από χρωστικές με παρόμοιες ιδιότητες που το φάσμα τους επίσης επικαλύπτεται. Γενικά, η μέθοδο του διαχωρισμού είναι ένας γραμμικός αλγόριθμος με τον οποίο μπορούμε να ορίσουμε την συνεισφορά στο ολικό σήμα κάθε μιας χρωστική ουσίας που βρίσκεται ταυτόχρονα στο υπό εξέταση δείγμα. Έτσι με αυτόν τον τρόπο μπορούμε να απομονώσουμε το σήμα που μας ενδιαφέρει από τα αλλά σήματα που υπάρχουν ταυτόχρονα στο κανάλι ανίχνευσης.

Για τα πειράματα μας έχουμε χρησιμοποιήσει δυο διαφορετικές χρωστικές το CFSE και το Atto590, καθώς ξέρουμε ότι τα φάσματα τους αλληλεπικαλύπτονται. Εν συνεχεία με την χρήση του φασματογράφου και της διάταξης FMT, προσπαθήσαμε να διαχωρίσουμε τις χρωστικές με δυο διαφορετικούς τρόπους. Ο πρώτος τρόπος έχει να κάνει με την εφαρμογή του γραμμικού αλγόριθμου στα ήδη αναδιαμορφωμένα δεδομένα. Ο δεύτερος τρόπος απαιτεί την εφαρμογή του γραμμικού αλγόριθμου για διαχωρισμό στα raw δεδομένα που πήραμε στο εργαστήριο, και μετά έχουμε την ανάλυση αυτών των ήδη διαχωρισμένων δεδομένων, ώστε να τα διαμορφοποιησουμε ξανά.

Table of Contents

Chapter 1

Introduction

Fluorescence molecular tomography (FMT) has developed a lot over the last years and is being considered as an important tool for detecting and analyzing the fluorescence signal, which exists inside small animal models. FMT is the technique that resolves molecular signatures in deep tissues by combining and implicating the theory of the diffuse theory with the use of fluorescent probes or markers [1, 2]. In the case of the FMT, the subject that carries the fluorescence probe is being exposed to light from different positions of the source and the emitted light is captured by detectors, such as a CCD camera. The value of the intensity and the path-length of the exciting photons provide very useful information on the optical properties of the excited tissue by means of a model-based interpretation in which photon propagation is described by the diffusion theory [3].

The development of all diagnostic imaging systems has required the use of tissue like objects that mimic the properties of the animal tissues in order to test and calibrate the systems, before their use with animal models [4]. These objects are called phantoms and reproduce the optical properties of biological tissues [5, 6]. However, the biggest limitation of this is the spectral overlap among the fluorescence probes which are simultaneously in the sample. The technique which helps us to overpass this problem is the spectral unmixing (in our case multi-spectral unmixing).

Generally, multi-spectral optical imaging is a relatively new approach in the biomedical field which combines the advantages of two already established optical modalities, optical imaging and optical spectroscopy [7]. The development in the use of the instruments, the variety of the fluorescent dyes, and the progress in the computer software that could be used for numerical analysis has helped and allowed the development of different approaches for multicolor analysis in which the spectrum of a dye mixture can be expressed as a linear combination of the component fluorophore spectra. Therefore, signal intensity of each dye can be expressed from a single composite spectrum [8].

In this thesis we first describe the system with which we can measure simultaneously the fluorescence image and its fluorescence spectrum for each source. Furthermore, we present and test the two different ways of unmixing the multispectral images, which are the unmixing in the reconstruction data and in the raw data. Last but not least, each of these two unmixing methods is being carried out using different kind of algorithms that have to do with the way of calculating the spectral strengths that we are going to use.

1.1 FMT principle

A schematic representation of an ideal non-contact fluorescence imaging setup is shown in Figure 1. A laser beam of wavelength λ_a illuminates a subject which contains specific fluorophores. The light propagates inside the medium and excites the fluorophores, which then emit light at different wavelengths λ_b. The emitted light is captured by a lens which is focused on the sample and recorded by a CCD camera. Different wavelengths are distinguished by appropriate bandpass filters placed in front of the camera lens [9-12].

The setup is comprised of three main components: the source, the subject and the detector. The most common illumination source is a laser beam X_{inc} in the position r, pointing at a direction s, t is the time dependency of the laser intensity and λ_a is the excitation wavelength. The medium of volume V is turbid, optically inhomogeneous and contains fluorophores with concentrations $N_t(r)$. The absorption coefficient expressed as $\mu_a(r)$ and the scattering coefficient as $\mu_s^{'}(r)$. These optical properties in addition to the fluorescent concentration should be constant during an experiment (or change in a time scale much longer than the propagation of the light). Finally, the term X_{prop} expresses the excitation and emission light that emerges from the surface of the sample.

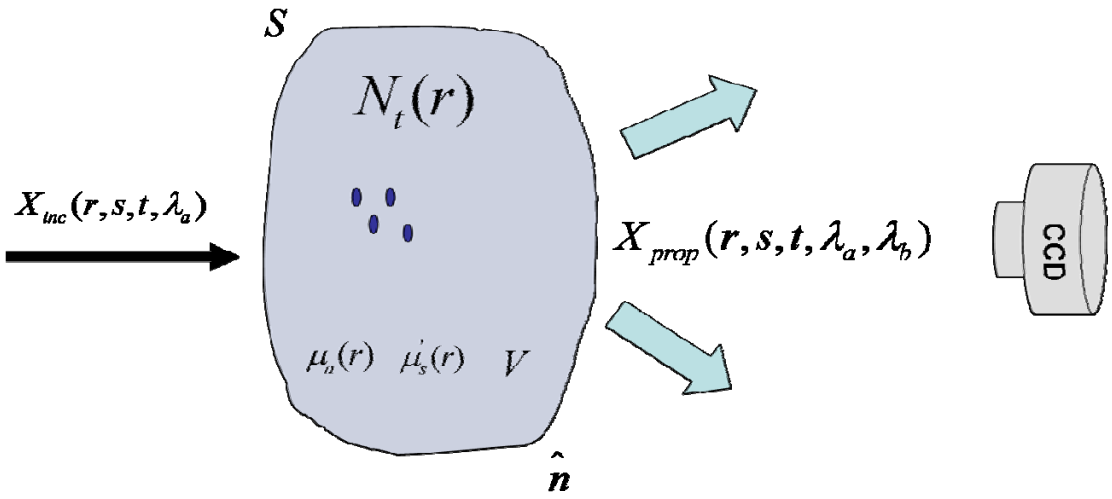

Figure 1 Schematic of the main idea of the FMT setup.

In order to solve the problem of reconstructing the map of fluorescence concentration $N_t(r)$ from the interior of a turbid medium, we have to divide it in two parts that are being called: the forward problem and the inverse problem. In the forward problem we know the distribution of the fluorescence concentration $N_t(r)$ in the volume V, the optical properties of the object $\mu_a(r)$, and $\mu_s'(r)$, and the source distribution X_{inc}, and we try to find out the light at any position of the medium X_{prop}, and consequently on the surface of the sample S as well. In a similar way, in the inverse problem we consider as known values the distribution of the light source X_{inc}, and the measurement of light distribution X_{prop} on the surface S. Therefore the optical properties of the sample $\mu_a(r)$, and $\mu_s'(r)$, and the distribution of the fluorophores $N_t(r)$ within V have to be derived. According to these we can obtain the tomographic image by solving the inverse problem, which demands solving the forward problem several times for each possible configuration. Table 1 shows a summary of the main idea of the solutions to the problem concerning the two parts of it.

Inverse Problem

$$N_t(r) = f^{-1}[X_{inc}(r,s,t,\lambda_a); X_{prop}(r,s,t,\lambda_a,\lambda_b)]$$

Forward Problem

$$X_{prop}(r,s,t,\lambda_a,\lambda_b) = f[X_{inc}(r,s,t,\lambda_a); N_t(r)]$$

Table 1 Forward and Inverse problem in the FMT.

In this thesis, the first two chapters describe the theoretical basis of extracting the tomographic images from non-contact measurements. More specifically, in chapter 2 the forward problem is presented, where the propagation of the excitation and fluorescent light inside a turbid medium is described. Also, there is a short reference to the contribution of the boundaries in order to extract the expression for the propagation of light. Chapter 3 deals with the inverse problem, the method used for extracting the fluorescence reconstruction, and with the theory of the multispectral imaging. Chapter 4 describes the materials and the experimental setup that were used. In addition, the data collection and acquisition are presented. The different ways of unmixing and the results of the study are presented in chapter 5 and chapter 6 respectively. Finally, in chapter 7 the results are discussed as well as some ideas for future studies.

Chapter 2

Theory I

Forward Problem

In this chapter we are going to explain more analytically how the forward problem is used to extract the tomographic images from the non-contact measurements. Light propagation in scattering and absorption media will be also discussed.

2.1 Theories of light propagation

The propagation of light in biological tissue can be explained with the use of the following two theories: the wave theory (Maxwell equations) and the transport theory. On the one hand, in the wave theory, firstly we have to solve the Maxwell equations for the investigated sample, and then by knowing and introducing the dielectric constant $\varepsilon(r)$ in each case, we can define the optical properties of our sample. Unfortunately, in practice, due to the complexity of the problem, it is not always easy to solve this kind of problem. On the other hand, in transport theory, light can be considered as energy, which is propagating thought a medium that contains particles. This problem is solved with the radiative transfer equation (RTE) according to which the propagating light has gains and losses due to the scattering and absorption process that take place in the sample [13, 14].

The Radiative transfer Equation (RTE) which describes the photon propagation in high scattering media, is given by the equation:

$$\frac{n}{c}\frac{\partial I(r,s)}{\partial t} = -s\nabla I(r,s) - \mu_t I(r,s) + \frac{\mu_t}{4\pi}\int_{4\pi} p(s,s')I(r,s')d\Omega' + \varepsilon(r,s) \qquad (2.1)$$

where n is the refractive index of the medium and c the speed of light in vacuum, μ_t is the transport coefficient, $\varepsilon(r,s)$ is the power radiated by the medium per unit volume and per unit solid angle in direction $\hat{s}$, $p(s,s')$ is the

phase function $d\Omega'$ is a differential solid angle in the direction ŝ′, and finally $I(r,s)$ is the specific intensity, which is defined as the average power flux at the position **r** which flows in the direction **ŝ** and has units of W cm^{-2} sr^{-1} (where sr represents unit of solid angle).

Generally, the RTE equation can be considered as a conservation equation for the average intensity. The first term in the right hand describes the loss in **r** and in the direction **ŝ,** the second term the loss due to factors such as the absorption and the scattering, the third term has to do with any gain due to scattering from other directions into the **ŝ** and the last term the gains due to any source in **r**.

The flux concentration can be calculated by the Equation (2.1) if we divide it over all 4π solid angle and is:

$$\frac{1}{c}\frac{\partial U(r)}{\partial t} + \nabla J(r) + \mu_a U(r) = E(r) \qquad (2.2)$$

Where $U(r) = \int_{4\pi} I(r,s)d\Omega$ is the average intensity, $J(r) = \int_{4\pi} I(r,s)sd\Omega$ is the total flux intensity and $E(r) = \int_{4\pi} \varepsilon(r,s)d\Omega$ is the source term that represents the power generated per unit volume.

2.2 Optical parameters

The most important parameters used to describe and understand light propagation are referred below [15].

μ_t : the transport coefficient or total attenuation coefficient and describes the probability that a photon gets either scattered or absorbed per unit length of its travel in the medium and is defined as:

$$\mu_t = \mu_a + \mu_s \qquad (2.3)$$

where μ_a is the absorption coefficient and μ_s is the scattering coefficient.

From the scattering coefficient we can define the scattering mean free path length which describes the mean distance that a photon can travel between two scattering events and is defined as:

$$l_{sc} = 1/\mu_s \qquad (2.4)$$

In the same way, the absorption path length can be defined as:

$$l_a = 1/\mu_a \qquad (2.5)$$

where l_a describes the average distance that a photon can travel before it is absorbed. In other words, represents the distance at which the light intensity decreases by a factor of e.

The parameter that characterizes the scattering properties of a medium is the scattering phase function $p(s,s')$, which gives as the probability of a photon that propagates in direction s to be scattered into a direction s'. Moreover, we should mention the reduced scattering coefficients μ'_s which takes into account the anisotropy of the scattered light and is defined as:

$$\mu_s^{'} = \mu_s(1-g) \qquad (2.6)$$

where g is the anisotropy factor that can be defined as:

$$g = \frac{\int_{4\pi} p(\hat{s}\hat{s}')\hat{s}\hat{s}'d\Omega'}{\int_{4\pi} p(\hat{s}\hat{s}')d\Omega'} \qquad (2.7)$$

and express the anisotropy of the scattered light on interaction with the particle and takes values from -1 to 1 depending if we have complete backscattering or forward scattering. The value $g = 0$ represents isotropic scattering.

The diffusion coefficient D is defined as:

$$D = \frac{1}{3\mu_s^{'}} = \frac{1}{3\mu_s(1-g)} = \frac{I_{tr}}{3} \qquad (2.8)$$

Finally, we can define and for this case the transport mean free path length, which is:

$$I_{tr} = \frac{1}{\mu_s^{'}} = \frac{I_{sc}}{1-g} \qquad (2.9)$$

and represents the average distance that a photon travel before its direction is completely randomized by series of scattering events.

The reduced scattering coefficient represents the mean random walk step. For example, in the case of a fully isotropic scattering where $g = 0$ we take $l_{tr} = l_{sc}$ which means that the radiation can be scattered to any direction after travelling one scattering mean free path. In the case of a fully anisotropic scattering where $g = 1$ and $l_{tr} = \infty$, the radiation travels large distances without changing its direction.

2.3 The diffusion Equation

There are several variations for the expression of the diffusion equation depending on the parameters considered [16, 17]. To begin with, lets assume that there is a high concentration of the scatterers inside the medium, so as the propagating light can be considered as highly incoherent and diffuse. We will also assume that the medium is illuminated by isotropic sources and its variation of the total flux occurs in a time scale much larger that the time between the scattering events. Taking all this into consideration, we can say that in the case of an infinite homogenous medium with constant values of the diffusion coefficient D and the absorption coefficient μ_a, we can write the diffusion equation as:

$$\frac{1}{c}\frac{\partial U(r)}{\partial t} - D\nabla^2 U(r) + \mu_a U(r) = E(r) \qquad (2.10)$$

One solution for the equation can be the following, if we suppose that we have a continuous source of photons at some point r_s:

$$U(r) \propto \exp[-\frac{|r - r_s|}{L_d}] \qquad (2.11)$$

where L_d is defined as the diffusion length and is calculated as:

$$L_d = \sqrt{\frac{D}{\mu_a}} \qquad (2.12)\,.$$

2.3.1 Solutions of the diffusion equation for infinite homogenous media

Although FMT has to do with objects that have certain dimensions, it is useful to start the analysis for the case of an infinite medium, and then put the contribution of the boundaries of the object.

If we look again in the simple schematic figure of an experimental setup (Figure 1), we can see two sources of lights. The first source is the laser emitting at a certain wavelength λ_a in order to illuminate the medium. The second is the fluorescence molecules that after being excited by the excitation light of the laser, emits light at a different wavelength λ_b. Taking these two parameters into consideration, we will first derive an expression for the propagation of the excitation light by applying the excitation source term in the diffusion equation and then defining the fluorescence term [18, 19].

2.3.2 The excitation source term

We can consider a continuous wave (cw) laser source which can irradiate the sample as shown in Figure 1. We can define the source within a scattering medium by considering a point source which is located at $z = l_{tr}$ inside the medium. In this way, we can write the source term with the help of the delta function as:

$$E(r,t) \rightarrow S_0 \delta(r) \qquad (2.13)$$

We used the delta function because it implies isotropic emission of light of strength S_0. By putting the Equation (2.13) in the diffusion equation (2.10), we obtain a modified Helmholtz equation which has the form:

$$\nabla^2 U(r) + \kappa_0^2 U(r) = \frac{S_0 \delta(r)}{D} \qquad (2.14)$$

where κ_0 is the wavenumber and is defined as:

$$\kappa_0 = i\sqrt{\frac{\mu_a}{D}} \qquad (2.15)$$

Now, by the use of the Green's functions in an infinite medium:

$$\nabla^2 G(\kappa|r-r_s|)+\kappa_0^2 G(\kappa|r-r_s|)=-4\pi\delta(r-r_s) \qquad (2.16)$$

the Helmholtz equation can be solved. The solution is:

$$G(\kappa|r-r_s|)=\frac{\exp(i\kappa_0|r-r_s|)}{|r-r_s|} \qquad (2.17)$$

Therefore, in the case of a point source, the distribution of the average intensity in an infinite homogeneous medium is given by the equation:

$$U(r)=\frac{S_0}{4\pi D}\frac{\exp(i\kappa_0|r-r_s|)}{|r-r_s|} \qquad (2.18)$$

We can also write it in a more general way of a source term with a spatial distribution $E(r,t)\rightarrow S(r)$ as:

$$U^{exc}(r)=\frac{1}{4\pi D}\int_V \frac{S(r)\exp(i\kappa_0|r-r_s|)}{|r-r_s|}dV \qquad (2.19)$$

2.3.3 The fluorescence source term

Next step is to find the expression for the propagating emitted fluorescence light. The incident light with wavelength λ_a will propagate inside the medium in a diffuse way, and will excite the fluorescent particles which will then emit photons of a different wavelength λ_b which will also be diffused. In this case, we have to solve the diffusion Equation (2.10) by applying the appropriate expression for the fluorescence source term. We describe the fluorescence process with a two-level system and we assume that the surrounding medium has no gain.

The number of the excited molecules per unit volume can be calculated by the expression:

$$\frac{\partial N_e(r,t)}{\partial t} = -\Gamma N_e(r,t) + \sigma^{fluo} U^{exc}(r,t)[N_t(r,t) - 2N_e(r,t)] \qquad (2.20)$$

where $N_e(r,t)$ is the number of fluorescence molecules per unit volume in the excited state for time t and at the position r. $N_t(r,t)$ is the total number of the fluorescent molecules per unit volume, σ^{fluo} is the absorption cross section of a molecule, $U^{exc}(r,t)$ is the excitation average intensity and Γ is the total radiative decay rate from the excited state into the ground state.

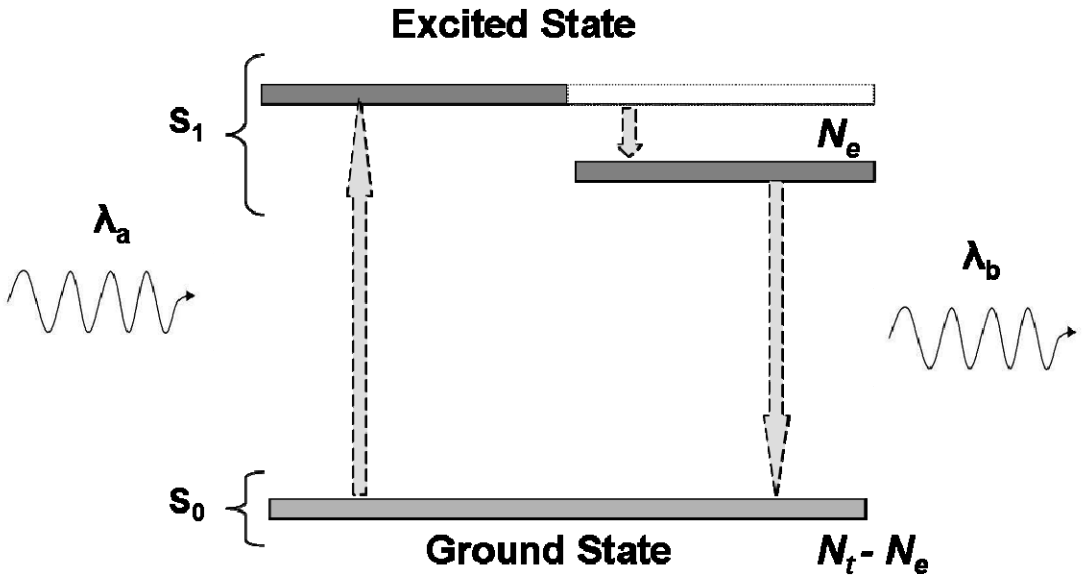

Figure 2.1 Emission in a two stage system

In the case of the experimental setup that we are going to use in the lab, we can reach a steady state situation as we use a continuous wave excitation source, which means $\frac{\partial N_e}{\partial t} = 0$. For this case, the equation (2.20) can give us the solution for the emitted molecules density number, which is:

$$N_e(r,r_s) = \frac{\sigma^{fluo} N_t(r,r_s)}{\Gamma + 2\sigma^{fluo} U^{exc}(r,r_s)} U^{exc}(r,r_s) \qquad (2.21)$$

If we also assume $\Gamma >> 2\sigma^{fluo} U^{exc}(r,r_s)$, which is happened in our experiments because the intensities we use are in the order of $\sim mW/cm^2$, the Equation (2.21) can be simplified as:

$$N_e(r,r_s)=\frac{\sigma^{fluo}N_t(r,r_s)}{\Gamma}U^{exc}(r,r_s) \qquad (2.22)$$

The source term of the fluorescence light which represents the number fluorescent photons emitted per unit volume and per second will be:

$$S^{fluo}(r,r_s)=\Gamma n N_e(r,r_s)=n\sigma^{fluo}N_t(r,r_s)U^{exc}(r,r_s) \qquad (2.23)$$

where n is the fluorescence quantum yield.

We can determine the propagation of the fluorescence light as the contributions over all fluorophores as:

$$U^{fluo}(r)=\frac{\sigma^{fluo}n}{4\pi D_b}\sum_{i=1}^{N}N_t(r)U^{inc}(r_1,r_s)\frac{\exp(-\kappa_b|r_i-r_1|)}{|r_i-r_1|}\Delta V_1 \qquad (2.24)$$

where $\kappa_b=\sqrt{\frac{\mu_a^{\lambda_b}}{D^{\lambda_b}}}$, with μ_a and D referring to the second emitted wavelength λ_b. It would be useful to write the Equation (2.24) in the term of the Green's Function:

$$U^{fluo}(r)=\frac{\sigma^{fluo}n}{4\pi D_b}\sum_{i=1}^{N}N_t(r)U^{inc}(r_1,r_s)G(-\kappa_{0b}|r_i-r_1|)\Delta V_1 \qquad (2.25)$$

,where $\kappa_{0b}=i\kappa_b$.

Now, we can obtain from Equation (2.25) if we put the excitation source term from the Equation (2.19):

$$U^{fluo}(r)=\frac{\sigma^{fluo}nS_0}{16\pi^2 D_a D_b}\sum_{i=1}^{N}\frac{\exp(-\kappa_a|r_1-r_s|)}{|r_1-r_s|}N_t(r_1)\frac{\exp(-\kappa_b|r_i-r_1|)}{|r_i-r_1|}\Delta V_1 \qquad (2.26)$$

As we can see from the last expression the quantum yield is a superposition of the two fields with different wavenumbers κ_a and κ_b that correspond to the excitation and the emission wavelength respectively.

Finally, we can write the Equation (2.26) in a more general way with the help of the Green's function as:

$$U^{fluo}(r) = \frac{\sigma^{fluo} n S_0}{16\pi^2 D_{exc} D_{fluo}} \sum_{i=1}^{N} G_{exc}(r_1, r_s) N_t(r_1) G_{fluo}(r_i, r_1) \Delta V_1 \qquad (2.27)$$

2.4 The Born approximation for the excitation term

Until now, the expressions that have been referred, deal with a weakly absorbing spatial distribution of the fluorophores. In the Born approximation we do not consider non-linear effects due to the existence of the other fluorophores in the excitation intensity. We assume that there is only a little fluorescence's absorption, which does not affect the intensity of the propagating excitation light. In this way, we can write that the average intensity of the incident light in the fluorophores is the same as in the absent of fluorescent and absorbing sources.

$$U^{exc}(r, r_s) \approx U^{inc}(r, r_s) \qquad (2.28)$$

2.5 Boundary conditions for planar interfaces

In order to solve the forward problem, we also have to take into consideration the shape of the volume of the sample, because the incident photons will also interact with the surface of the subject. Depending on the sample, the surface of the object is not always planar. In order to find a solution on the surface of the medium, there are specific conditions that have to be fulfilled and these are called boundary conditions [20].

In the diffusion approximation the exact condition of an index mismatched boundary, is that the component of the flux normal to the interface, pointing from the non-scattering medium into the turbid medium have to be zero:

$$J_{in}(r) = 0 \qquad (2.29)$$

If the turbid medium is bounded by a transparent medium with their refractive indices substantially different, we must take into consideration all the possible Fresnel reflections at the interfaces from the flux inside the turbid

medium. Therefore, we must assume that also all the flux traversing the interface is toward the non-diffusive medium which means:

$$J_{out}(r) = J_n(r) \qquad (2.30)$$

In order to solve the problem, two assumptions have to be made. Firstly, all the incident photons are initially scattered at a depth z_0, where

$$z_0 = I_{tr} = \frac{1}{(1-g)\mu_s} \qquad (2.31)$$

Secondly, we have to specify the boundary conditions in the surface of the subject. So, in order to be sure that there is a continuously light propagation in the surface, we can assume that the average intensity is $U(r) = 0$ for $z = 0$. This gives us the opportunity to add a negative image source of photons to the infinite medium problem as shown in Figure 3.1?. According to these, the average intensity for the reflectance geometry will be:

$$U(r) = \frac{S_0}{4\pi D_c}\left[\frac{\exp(-i\kappa r_0)}{r_0} - \frac{\exp(-i\kappa r_c)}{r_c}\right] \qquad (2.32)$$

where $r_0 = \sqrt{|z - z_0|^2 + p^2}$ and $r_c = \sqrt{|z + z_0|^2 + p^2}$.

The boundary condition can be expressed as an equation that relates the average intensity $U(r)$ with the flux density $J(r)$ at the interface with the form of:

$$U(r) = C_{nd} J(r)\hat{n} = C_{nd} J_n(r) \qquad (2.33)$$

where $\hat{n}$ is the surface normal pointing outwards from the medium, J is the flux vector, J_n is the total flux traversing the interface and C_{nd} is a coefficient related to the refractive index mismatch between both media. In this way we can express then flux density for the reflection geometry as:

$$J(r) = \frac{S_0}{4\pi c C_{nd} D}\left[\frac{\exp(-i\kappa r_0)}{r_0} - \frac{\exp(-i\kappa r_c)}{r_c}\right] \qquad (2.34)$$

In a similar way, we present the expression of the average intensity and the flux density for the transmission geometry. The extra boundary condition

which is used is that the average intensity $U(r)=0$ also for $z=d$., where d is the thickness of the finite slab. So, for this case we take for the average intensity the expression:

$$U(r)=\frac{S_0}{4\pi Dc}\sum_{m=1}^{M}[\frac{\exp(-i\kappa R_0(m))}{R_0(m)}] \qquad (2.35)$$

where $R_0(m)=\sqrt{(2floor(\frac{m}{2})(d+z_0)+(-1)^{m-1}(z-z_0)^2+p^2}$, where $floor(x)$ is the nearest integer of x toward minus infinity, and $0<z<d$. The expression for the flux density will be:

$$J(r)=\frac{S_0}{4\pi cDC_{nd}}\sum_{m=1}^{M}[\frac{\exp(-i\kappa R_0(m))}{R_0(m)}] \qquad (2.36)$$

Depending on the geometry the appropriate equations are used.

Chapter 3

Theory II

Inverse Problem

Having described the forward problem and in order to proceed to the reconstruction of the fluorescent spatial distribution, we have to solve also for the inverse problem which is presented in this chapter. Furthermore, the principles of multispectral imaging being the main core of our experiments are described in detail.

3.1 The normalised Born approximation

The normalized Born algorithm has been proposed for accurate reconstruction of fluorescent, scattering or absorption heterogeneities in diffuse media. The main idea of the algorithm is the use of the excitation measurements in order to specify the intrinsic properties of the subject. Therefore, the fluorescent heterogeneities are determined by dividing the fluorescence signal measured at wavelength λ_b by the incident excitation measurement at wavelength λ_a [21]

Therefore, according to the Equation (2.18) the incident photon field detected at a position r_d is given by the expression:

$$U^{inc}(r_s, r_d) = QE^{\lambda a}\Theta_f^{exc}\Theta_d(r_d)U^{exc}(k^{\lambda a}\left|r_s - r_d\right|) \qquad (3.1)$$

where $QE^{\lambda a}$ is the detector quantum efficiency at wavelength λa, Θ_f is the attenuation caused by the emission filter used in order to collect the excitation light, $\Theta_d(r_d)$ accounts for the detector gain and $k^{\lambda a}$ denotes the wavenumber for the optical properties of the medium at wavelength λa.

In an analogous way, the fluorescent light at a position r_d can be

expressed as:

$$U^{fluo}(r_s, r_d) = QE^{\lambda b}\Theta_{\phi}^{fluo}\Theta_d(r_d)\frac{\sigma^{fluo}n}{4\pi D_{fluo}}\sum_{i=1}^{N}U^{exc}(k^{\lambda a}\left|r_i - r_s\right|)N_t(r)G_{fluo}(k^{\lambda b}\left|r_d - r_i\right|)\Delta V \qquad (3.2)$$

where $QE^{\lambda b}$ is the detector quantum efficiency at the emission wavelength λb, Θ_f is the attenuation caused by the emission filter used in order to collect the emission light, $k^{\lambda b}$ denotes the wavenumber for the optical properties of the medium at wavelength λb and $G(k^{\lambda b}\left|r_d - r_i\right|)$ is the Green's function solution to the diffusion equation in a slab and describes the propagation of the emission photon wave from the fluorophore to the detector in a slab configuration.

In order to find solution for the Equation (3.2), we have to determine all the position dependent factors $\Theta_d(r_d)$ for each detector. Then, the normalized Born measurement U^{NB} can be derived by the division of the fluorescent light at a position r_d divided by the incident one.

$$U^{NB}(r_s, r_d) = \frac{U^{fluo}(r_s, r_d)}{U^{inc}(r_s, r_d)} = \qquad (3.3)$$

$$= a\frac{\sigma^{fluo}n}{4\pi D_{fluo}U^{exc}(\kappa^{\lambda b}\left|r_s - r_d\right|)}\sum_{i=1}^{N}U^{exc}(k^{\lambda a}\left|r_i - r_s\right|)N_t(r)G_{fluo}(k^{\lambda b}\left|r_d - r_i\right|)\Delta V$$

Where $a = \frac{QE^{\lambda b}\Theta_f^{fluo}}{QE^{\lambda a}\Theta_f^{exc}}$ is a calibration factor and can be determined experimentally. Generally, the normalized Born algorithm normalizes the fluorescent signal measured to the intrinsic properties and the heterogeneities of the subject.

3. 2 Weight Matrix

The normalized Born approximation in fact, is a way to normalize the data measured in the experiment. In order to extract a tomographic image, we

have to discretize the medium into N volume elements the voxels. In the same way, we can discretize the detecting area into M detector points. We need to find the reconstruction of the fluorescent source spatial distribution defined as $f(r)$. Assuming that the function in each voxel $f(r)$ is constant and that the centre of each voxel is given by r_j, we can write that $f_j = f(r_j)$ will be also constant for all j voxel.

The contribution of each voxel can be correlated to the measurement of each detector though the expression:

$$\sum_{j=1}^{N} w_{ij} f_j = p_i \qquad i = 1,2,3,.....,M \qquad (3.4)$$

where w_{ij} is the weighting factor that represents the contribution of the j th voxel to the i th detector point.

The Equation (3.19) can be expanded in matrixform as:

$$\begin{bmatrix} p_1 \\ p_2 \\ p_3 \\ . \\ . \\ . \\ p_M \end{bmatrix} = \begin{bmatrix} w_{11} & w_{12} & w_{13} & . & . & . & w_{1N} \\ w_{21} & w_{22} & w_{23} & . & . & . & w_{2N} \\ w_{31} & w_{32} & w_{33} & . & . & . & w_{3N} \\ . & . & . & & & & . \\ . & . & . & & & & . \\ . & . & . & & & & . \\ w_{M1} & w_{M2} & w_{M3} & . & . & . & w_{MN} \end{bmatrix} \times \begin{bmatrix} f_1 \\ f_2 \\ f_3 \\ . \\ . \\ . \\ f_N \end{bmatrix} \qquad (3.5)$$

where the p_i matrix represents the signal that can reach the detector, the f_j matrix represents the distribution of the fluorescent sources in each point of r inside the volume V, and the w_{ij} matrix represents the contribution of each voxel to the signal, which is measured from each detector point. w_{ij} is called weight matrix. In order to solve the above system, we have to invert the weight matrix w_{ij} hence the inverse problem.

3.3 The algebraic reconstruction technique (ART)

The inversion of the weight matrix can be performed in many ways, depending on the size of the matrix [22]. For matrices with large dimensions,

as in our case, algebraic methods are used in order to be solved, as numerical inversion is very difficult. The algebraic reconstruction technique (ART) is an iterative technique that can deal with such kind of matrices and is based on the method of projections.

When there is a problem with N variables, the signal that has been measured by the CCD camera can be described by a system of N equations. This system will give N degrees of freedom to the fluorescence source distribution pattern. In this way, the imaging target instead of being represented by a matrix in the form of $(f_1, f_2, f_3, ..., f_N)$ can be considered as a single point in a N - dimensional space. In that space each of the above equations represents a hyperplane. When a unique solution to these equations exists, the intersection of all the hyperplanes is a single point giving that solution.

We can see in Figure 3.1 the simple case of only two variables f_1 and f_2, for which we have the following two equations:

$$\begin{aligned} p_1 &= w_{11} f_1 + w_{12} f_2 \\ p_2 &= w_{21} f_1 + w_{22} f_2 \end{aligned} \qquad (3.6)$$

Each equation represents a line in a two dimensional space (f_1, f_2). The solution of the system of Equation (3.6) is given by the intersection of the two lines. In order to find a solution, we first start by a initial guess (f_1^0, f_2^0), projecting this initial guess on the first line, projecting the resulting point on the second line, and then projecting back into the first and so on until the intersection point is reached, The projection from the one line to the other and then back consist of one iteration. If there is a unique solution, the iterations will always converge to that point.

In practice, the extraction of a tomographic image with the inverse method does not have only one solution. There are many different configurations of the fluorophores that can give the same results. This has to do with the number of the volume elements in comparison to those of the detector points.

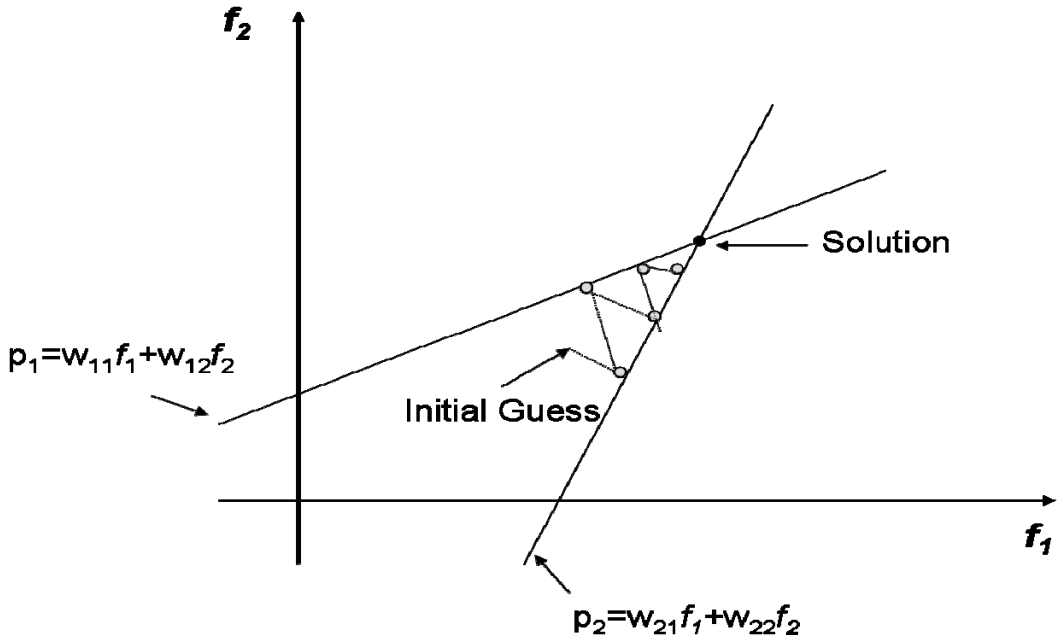

Figure 3.1 Graphical representation of the ART technique for a well defined system of two variables.

According to these we can refer to the following cases:

1) If $M = N$ then the system has a unique solution, and we have a well defined problem to deal with.
2) If $M > N$ has not only one solution, since the problem is over determined, because there are more equations than the unknowns.
3) Finally, if $M < N$ the problem is under determined. There are fewer equations than the number of unknowns, and in this way the problem has an infinite number of solutions.

3.4 Spectral imaging

Spectral imaging is a method that combines the advantages of two applied modalities: imaging and spectroscopy. The combination of these requires the creation of a 3D data set that contains many images of the same object, where its one of them is measured at a different wavelength. This means that the total acquisition of time will be longer than the usually one. In this chapter we will make a short introduction of these two modalities, as we are based on them in order to process our data [23, 24].

3.4.1 Optical Imaging

Optical imaging (or molecular optical imaging) is based on the detection of light and is a technique of acquiring spatial and temporal data information from objects in order to obtain information about their chemical and physical characteristics. Until now, digital imaging is the most applicable method where data are being recorded by a digital camera such as a charged coupled device (CCD camera) [25].

The quality of the image determinates the amount of information that can be extracted from it. The most common parameters that characterize an optical image are:

- The spatial resolution that determines the closest distinguishable features. It depends mainly on the wavelength, the numerical aperture of the objective lens, the magnification that we use, and the pixel size of the array detector.
- The lowest detectable signals that depend on the quantum efficiency of the detector, the noise of the system, the numerical aperture of the lens, and the quality of the optics.
- The dynamic range of the acquired data that determines the number of different levels of intensities that can be detected in one image. This depends on the maximal possible number of electron at each pixel and on the lowest detectable signal.
- Finally, the exposure time and the binning of the CCD pixels are also important.

In reality, there are more imperfections that can reduce the quality of the image such as the non-specific staining, bleaching or autofluorescence. This, however, should be distinguished from the physical limitations set by the electro-optical system itself and the nature of light.

3.4.2 Optical spectroscopy

Spectroscopy is the study of the interaction between radiation and matter as a function of wavelength. It is often used to describe different phenomena, mainly happening in the visible light range. A spectrum is a collection of light

intensities at different wavelengths. Therefore, spectroscopy tries to acquire and explain the spectral characteristics of matter [26, 27].

The structure of molecules is directly related to spectroscopy. In fact, the spectrum is a direct measurement of the energy levels of the investigated molecules. In fluorescence measurements, the fluorophores are themselves the source of light. In order to measure the spectrum, the light is dispersed into its different wavelength components and the intensity at each pixel is measured. Again, there are some parameters that can characterize the quality of the signal, which are:

- The spectral resolution that determines the closest wavelengths that can be distinguished,
- The spectral range in which the spectra can be measured.
- The lowest detectable signal and the dynamic range.

The spectral information that can be obtained allows detecting and distinguishing among many different fluorophores even if they have a similar color or overlapping spectra. In many cases there is the need of observing simultaneously more than one dye in order to identify a number of proteins or tissues. Also, there are many different dyes with the same color and by using a simple coloring technique perhaps they can not be distinguished.

3.5 Czerny-Turner Spectrograph

A spectrograph is an instrument used to separate and measure the wavelengths present in electromagnetic radiation, and to measure the relative amounts of radiation at each wavelength. Light entering a spectrograph can be split or dispersed into a spectrum by using a prism or a diffraction grating. A diffraction grating is an optical element that separates polychromatic light into its constituent wavelengths (colors). Incident polychromatic light will be reflected from the grating at a slightly different angle.[33]

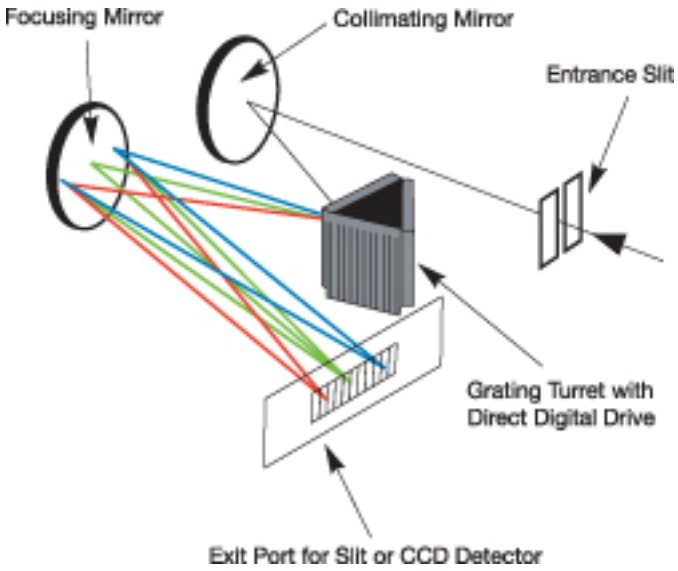

Figure 3.2 Schematic of Czerny Turner spectrograph

The Czerny-Turner spectrograph used in our experimental setup employs a pair of concave mirrors and a plane grating as the dispersive element. As we can see from the Figure 3.2, the first mirror collimates the light passing from the entrance slit and directs it on the grating. The second mirror gathers the light from the grating and directs the multiple images on to the detector where is being recorded by the CCD camera. The range of the wavelengths that can be detected can be varied by rotating the plane grating angle to select the required diffracted images.

Chapter 4

Materials and Methods

In this chapter we are going to describe the experimental setup and the samples measured for the purpose of this project. The samples used are tissue-like phantoms as we can control their geometry and their optical properties to mimic the properties of animal tissues.

Moreover, we will present the function of the Fluorescence Molecular Tomography (FMT) system and the spectrograph which we have combined to perform multispectral studies and experiments.

4.1 Tissue-like phantoms

The development of diagnostic imaging systems has required the use of tissue-like objects (or phantoms) that mimic the properties of the animal tissue in order to test and calibrate the systems, before their use in animal models [6]. Phantoms can reproduce the optical properties of biological tissues, and have similar behavior when illuminated by light.

To be more specific, they model the geometry and the optical parameters of physiological structures that are relevant for the transport of light [4, 28]. The physical parameters of a phantom should be stable for a period of time and do not dependent on the environment. Furthermore, their components should be compatible with each other concerning the chemical stability and their spectroscopic properties. Finally, their preparation should be simple and fast.

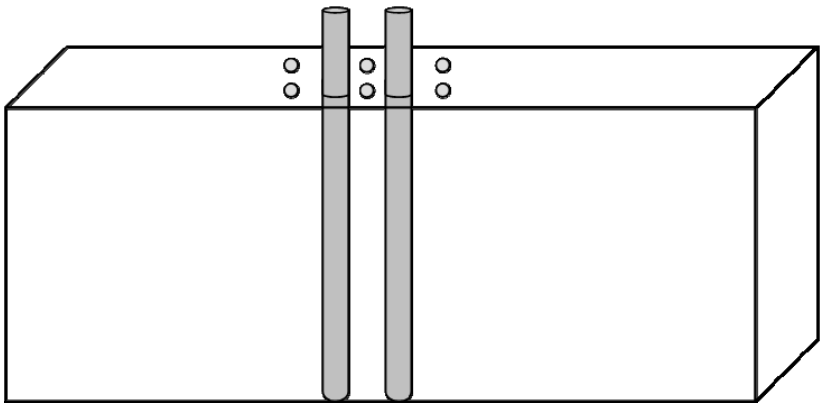

Figure 4.1 Tissue like phantom.

4.2 Preparation of liquid phantoms

Phantoms can be solid or liquid depending on the experiments that are going to be used. In our experiments we have used only liquid phantoms, as it was quite easy and fast to prepare them.

They were prepared by mixing the correct proportions of the scattering and absorbing media in a solvent, so that the resulting substance will have the desired intrinsic optical properties of the tissue we want to mimic [5]. These optical properties are the absorption coefficient (μ_α), the scattering coefficient (μ_b), the anisotropy factor (g), and the index of refraction (n). Phantoms usually consist of a scattering medium, an absorbing medium, a solvent and the fluorophores. In order to choose the most useful phantom materials and design, we need to think also about the geometrical properties of the sample we want to have, such as the thickness, the heterogeneities, the shape, and possible mechanical constraints.

In our experiments we have used Intralipid-20% as a scattering substance. Intralipid is a lipid emulsion that contains soybean oil, egg phospholipids and glycerol and is also used as an intravenously administered nutrient in hospitals. It is a polydisperse solution of particles with an average diameter of ~ 0.4 μm. The soybean oil micro particles determine the light diffusion inside the phantoms. The phospholipids and glycerol are responsible for the homogeneous distribution of the scattering particles in the solution. The benefit of using lipid micro particles emulsions, such as

Intralipid, is that they are biological similar to what is thought to cause scattering in tissue which is the bilipid membrane of cells.

As far as the absorption we want the phantoms to have, either organic like whole blood and haemoglobin or inorganic materials such as ink and other molecular absorbing dyes can be added in order to achieve the desired value of the absorption coefficient for each phantom. For our phantoms we used black India ink. Both these substances were added to distilled water. The concentration that we used was 5ml Intralipid and 4.88μl ink in a solution of 100ml, in order to achieve a solution with $\mu_a = 0.3cm^{-1}$ as the value of the absorption coefficient and reduced scattering coefficient with value $\mu_s^{'} = 16cm^{-1}$. In order to induce fluorescent concentration in specific positions inside the phantoms borosilicate micro capillary tubes (Drummond Scientific, US) with an outer diameter of 1.8 mm and an inner of 1.2 mm were embedded in the phantom.

As fluorophores we have used:

A Carboxyfluorescein succinimidyl ester (CFDA(5(6) -CFDA SE or CFSE) solved in 1×phosphate-buffered saline solution with pH of 9, quantum yield 0.93 and extinction coefficient 78.000 $(cmM)^{-1}$ at its absorption maximum. CFSE exhibits an absorption peak at 492nm and a fluorescence peak at 517nm and is widely used for simulating the emission of the Green Fluorescence Protein (GFP) molecule. We can see its excitation and emission spectra in Figure 4.2 taken from the invitrogen company [30].

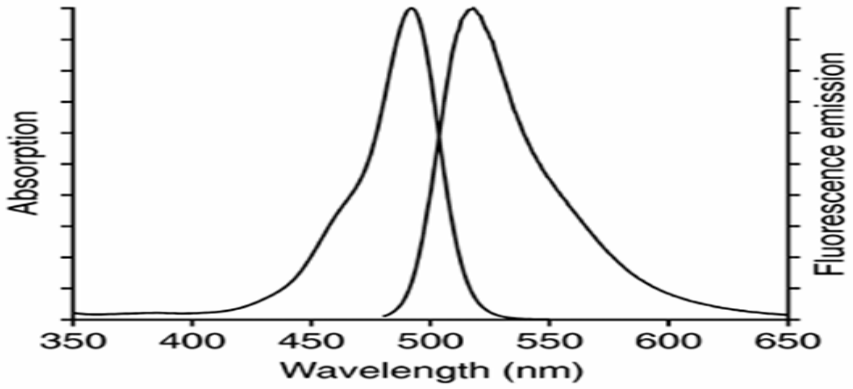

Figure 4.2 Absorption and Fluorescence Spectra for CFSE

The other fluorophore that we have used is Atto-590 (Atto-Tec, Germany) which is a new fluorescent label belonging to the class of Rhodamine dyes and was also solved in 1×phosphate-buffered saline solution with pH of 12 quantum yield 0.8 and extinction coefficient 120.000 $(cmM)^{-1}$ at its absorption maximum. Atto-590 exhibits an absorption peak at 594 nm and a fluorescence peak at 624 nm and is used for simulating the emission of the Red Fluorescence Protein DsRed. Important characteristics of the Atto-590 are its strong absorption, the high fluorescent quantum yield, the high photostability and the very little triplet formation. The excitation and emission spectra of Atto-590 is shown in Figure 4.3 taken from the Atto-tech company [31].

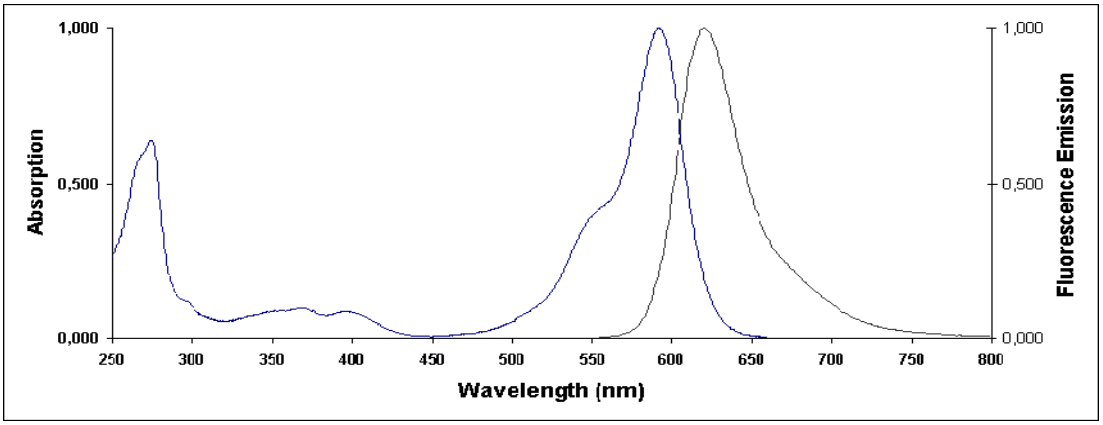

Figure 4.3 Absorption and Fluorescence spectra of Atto590

4.3 Experimental setup

The FMT system has been used in all the experiments. The system is suitable for applying non contact measurements, and acquiring tomographic information, and 3D reconstruction of the fluorescent region inside the volume of the illuminating sample. A schematic of the FMT and spectra acquisition hardware setup is shown in Figure 4.4.

4.3.1. FMT setup

As we can see from Figure 4.4, the Illumination is provided by a cw Argon-Ion Laser (Laser Physics, Reliant 1000m, West Jordan, UT 84088 USA) (i). The laser emits at several wavelengths through the visible spectrum. The main

lines of the laser are at 458nm, 488nm and at 514.5nm. In front of the laser there is a filter wheel, which enables us to choose the wavelength we want to excite the fluorophores. The laser light is directed to the box with the sample by a group of stable, moving and flip mirrors. Inside the box there is another pairs of mirrors which lead the beam into the laser scanning device (Scancube 7, Scanlab) which incorporates a system of mirrors mounted on miniaturized galvanometer motors (ii). These mirrors are being controlled by the software and the laser beam can be guided in two directions. The laser beam finally is guided to the sample by using large rectangular mirrors (first surface mirrors, 4-6 Wave, 73 mm 116 mm, Edmund Optics). The one mirror is mounted permanently on the ceiling of the box (iv), while the other lies on the optical table and can move along a rail between two fixed positions altering the geometry of the experiment between reflection and transmission. For measurements in the reflection geometry the bottom mirror is moved forth so that the laser beam is directed to the top mirror and then to the sample from the side of the camera (iiia). For measurements in transmission geometry the bottom mirror is moved to the back position, so that the laser light illuminates the sample from the bottom side (iiib).

The sample is placed on a transparent glass plate with an anti-reflection coating (Glassplate, High AR coated 96-99% (400-700nm)). The glass plate is mounted on a platform that is placed on an X-Y translation stage (v). The X-Y movement aligns the subject in respect to the camera axis. Depending on the desired resolution of each measurement the distance of the sample from the camera (height of the sample) can be modified by placing the glass plate in one of the different fixed positions along the Z axis. The plate is mounted to the stages with a simple custom-made clip system so that it can be easily removed and put back in the setup for the repetition of the measurements. Images are captured by a thermoelectrically cooled 16bit CCD camera with a chip size of 1024×1024 pixels (Andor Corp., DV434, Belfast, Northern Ireland), which is mounted on the upper plate of the imaging box (vi). The CCD camera is equipped with a SIGMA 50mm f/2.8 objective (Sigma Corporation, Tokyo, Japan) which was focused on the sample's surface.

4.3.2. Spectroscopy setup

For spectral data acquisition of our imaging samples we have used a Czerny-Turner optical spectrograph (Andor Technologies SR-163, 163mm focal length, numerical aperture f/3.6) (ix). A CCD camera identical to the one described above is attached to output of the spectrograph together while light is coupled by means of an optical fiber (viii). The end of the fiber is inside the box and is attached to the platform so that it can move together with the sample in the X-Y translation stage. In this way, we can have a constant distance between the fiber and the illuminated sample through out all the experiments.

4.4. Spectral and FMT acquisition

After placement of the sample in the imaging plate in front of the CCD camera, we choose the geometry of the measurements (transmission or reflection) and the height. Then we set the parameters of the experiment on the software developed in Labview environment.

Initially, we choose the temperature that the two CCD cameras want to reach. Then with the use of a piece of millimetre paper we fix the magnification of the CCD camera so as we can see clearly the lines of the paper. Then we calibrate the laser beam for the geometry we are going to use by choosing its movement in the two axis x and y. Then, we take a white light image of the sample that helps us to set the sources (illumination points) that we are going to use later in the experiments.

Finally, we choose an appropriate exposure time and power for each measurement so that the entire dynamic range is exploited. The arrangement of the sources is chosen according to the shape and the size of the sample, while the number of sources is determined by the resolution requirements of each experiment.

In front of the CCD camera there is also a filter wheel, with different bandpass interference filters to choose the correct wavelength range. We also use the appropriate filters in front of the laser to choose the correct excitation wavelength. In our case we have used the 488nm and 514.5nm laser lines. We record the excitation images by using the 480nm ± 30nm and 510nm ±

5nm filters respectively in front of the camera and for the fluorescence images by using 540nm ± 20nm and 615nm ±45nm filters respectively in front of the camera. Typical exposure time during the FMT acquisition for the excitation measurements was 0.1sec and for the fluorescence measurements 0.3sec. For the recording of the spectra a typical exposure time was 6sec. Data acquisition was performed with two computers, the one with a 3.0 GHz PC with 1 GB RAM and the other with a 3.0 GHz PC with 500 MB RAM. The two computers are connected together with a cable, so as we could achieve for the same position of the source to have simultaneously the FMT and the spectral image.

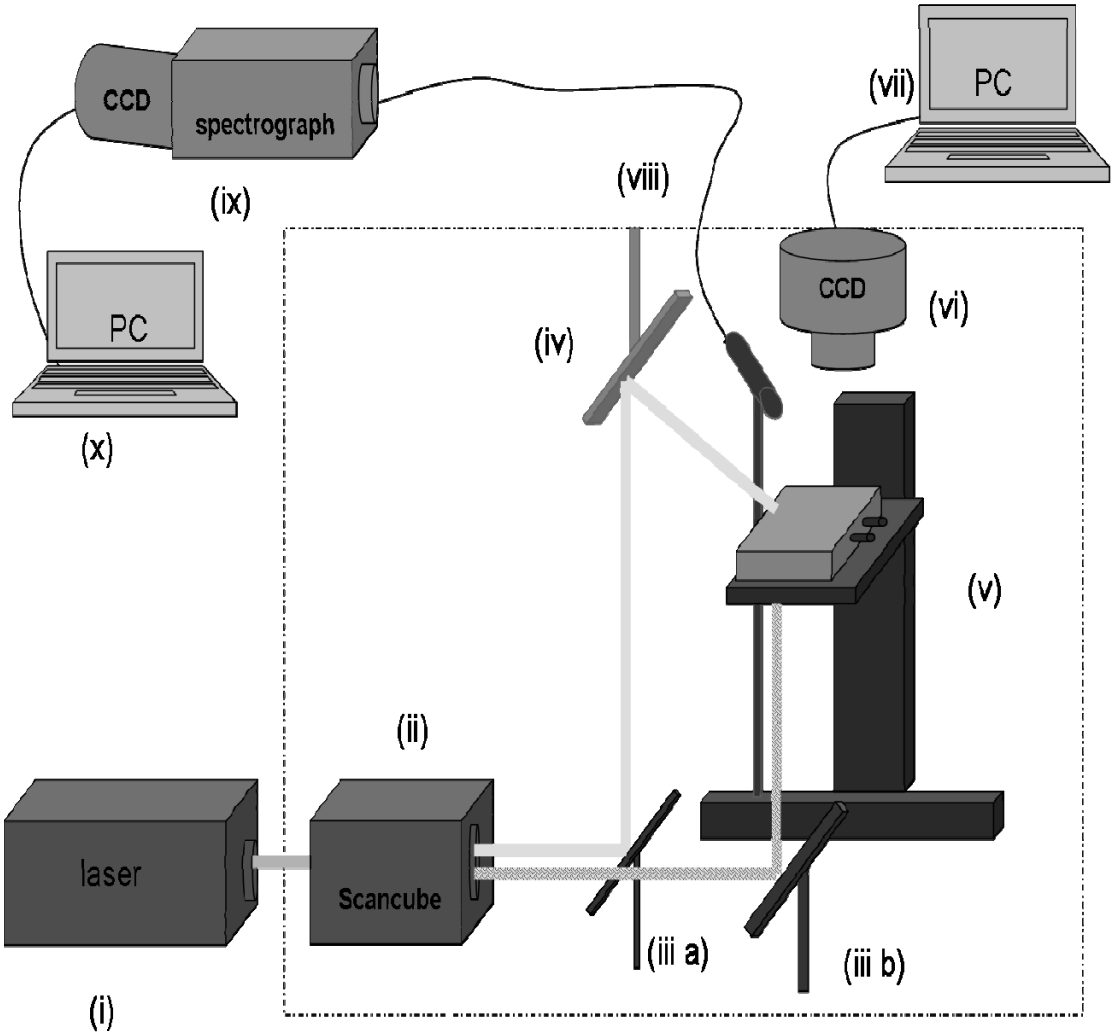

Figure 4.4 Experimental setup

4.5 Data processing

4.5.1 FMT reconstruction

The data from the experiment are stored in the form of a stack of two dimensional images $I(x, y)$, which will be processed in order to obtain a three dimensional reconstruction of the fluorescence in the sample. Reconstruction of the fluorescence tomography data utilized the normalized Born approximation. Data are processed through software developed in the Labview environment. We set the input parameters in the program which are the optical and the geometry parameters of the sample; the absorption and scattering coefficient and the width. According to the geometry we choose the number of the detectors in each axis, the area of the detector as well as the size and the number of the Mesh points in x, y and z. The number of the mesh points will form the volume of the voxels. We can see all these parameters in Figure 4.5 where a snapshot of the Labview processing program is depicted.

As described above (Chapter 3.1 the normalized Born approximation) the fluorescence signal is express at a position r_d as:

$$U^{fluo}(r_s, r_d) = QE^{\lambda b}\Theta_{\phi}^{fluo}\Theta_d(r_d)\frac{\sigma^{fluo} n}{4\pi D_{fluo}}\sum_{i=1}^{N} U^{exc}(k^{\lambda a}\left|r_i - r_s\right|)N_t(r)G_{fluo}(k^{\lambda b}\left|r_d - r_i\right|)\Delta V \qquad (4.1)$$

where $QE^{\lambda b}$ is the detector quantum efficiency at the emission wavelength λb, Θ_f is the attenuation caused by the emission filter used in order to collect the emission light, $k^{\lambda b}$ denotes the wavenumber for the optical properties of the medium at wavelength λb and $G(k^{\lambda b}\left|r_d - r_i\right|)$ is the Green's function solution to the diffusion equation in a slab and describes the propagation of the emission photon wave from the fluorophore to the detector in a slab configuration.

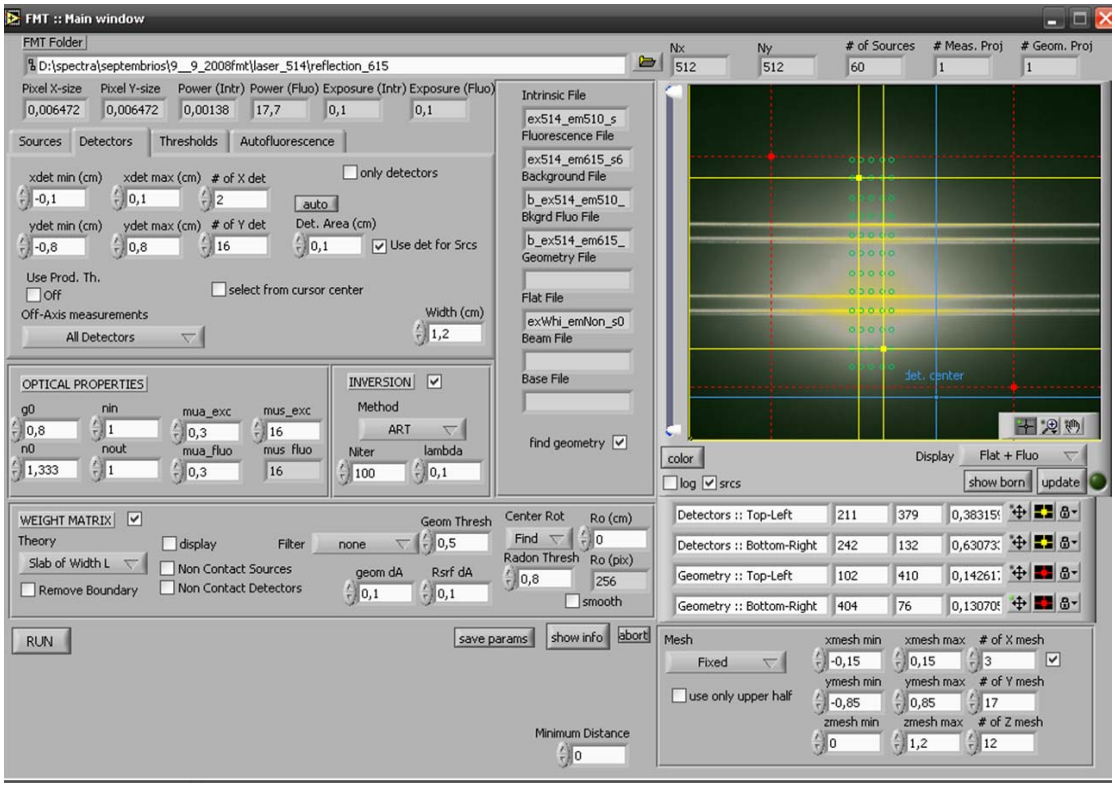

Figure 4.5 Main window of the Labview program for FMT data processing.

In an analogous way, the incident photon field detected at the position r_d, is express as:

$$U^{inc}(r_s, r_d) = QE^{\lambda a}\Theta_f^{exc}\Theta_d(r_d)U^{exc}(k^{\lambda a}|r_s - r_d|) \qquad (4.2)$$

where $QE^{\lambda a}$ is the detector quantum efficiency at wavelength λa, Θ_f is the attenuation caused by the emission filter used in order to collect the excitation light, $\Theta_d(r_d)$ accounts for the detector gain and $k^{\lambda a}$ denotes the wavenumber for the optical properties of the medium at wavelength λa.

Then the normalized Born approximation is calculated by dividing the fluorescence measurement with the excitation measurement. After that, the normalized measurements are inverted with the Algebraic Reconstruction Technique (ART) in order to create a map of the spatial distribution of the fluorescent concentration inside the reconstructed volume of our sample.

4.5.2 Spectral analysis.

The data from the spectrograph measurements are also stored in a form of two dimensional images $I(\lambda, y)$. These data give us the spectrum of each source in a certain wavelength area. They are processed by a code written in Matlab. Each stack of the raw data is stored in a new file. For each illumination point we reduce the 2D image $I(\lambda, y)$ to a spectrum $I(\lambda)$ by summing up the intensity values over y. Figure 4.6 shows spectra corresponding to different sources for a phantom containing CFSE and ATTO590.

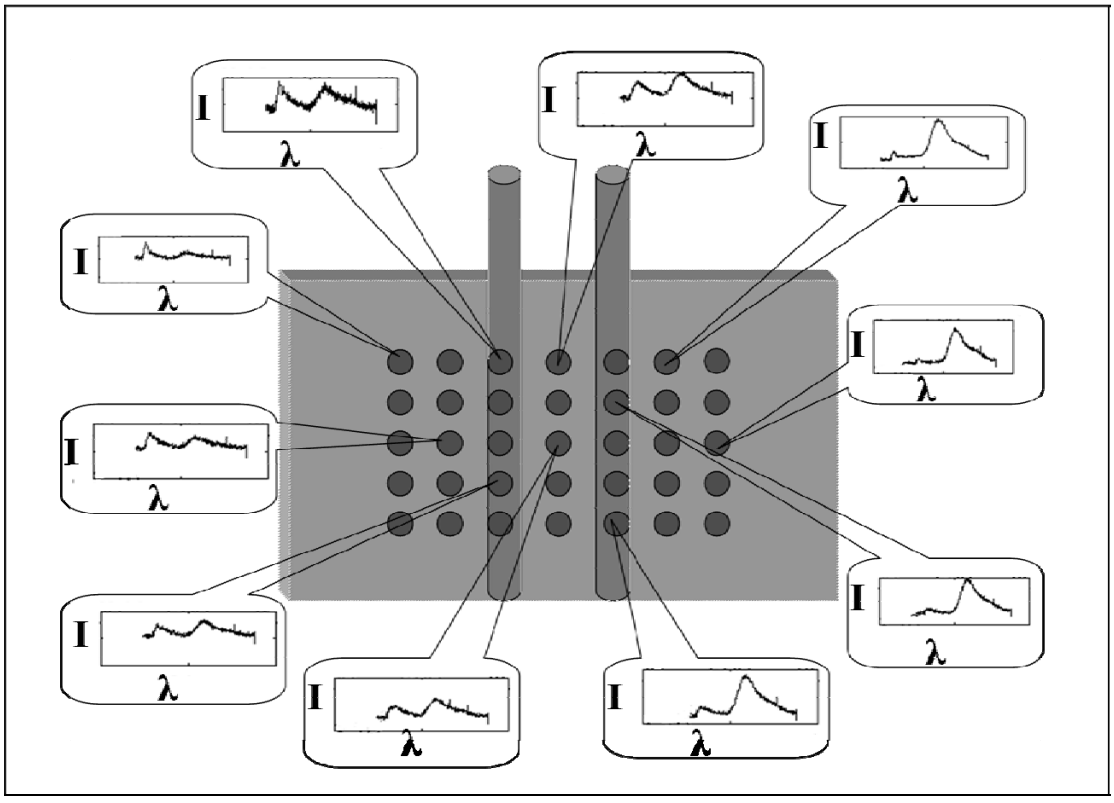

Figure 4.6 the different spectrum of each source

In Figure 4.7 we can see the different intensities for each source and for different concentrations of the ATTO590 when the phantom was illuminated at 488nm laser. (a) the ratio of 4μM CFSE and 5μM Atto590, (b) 4μM CFSE and 10μM Atto590 and finally (c) 4μM CFSE and 15μM Atto590.

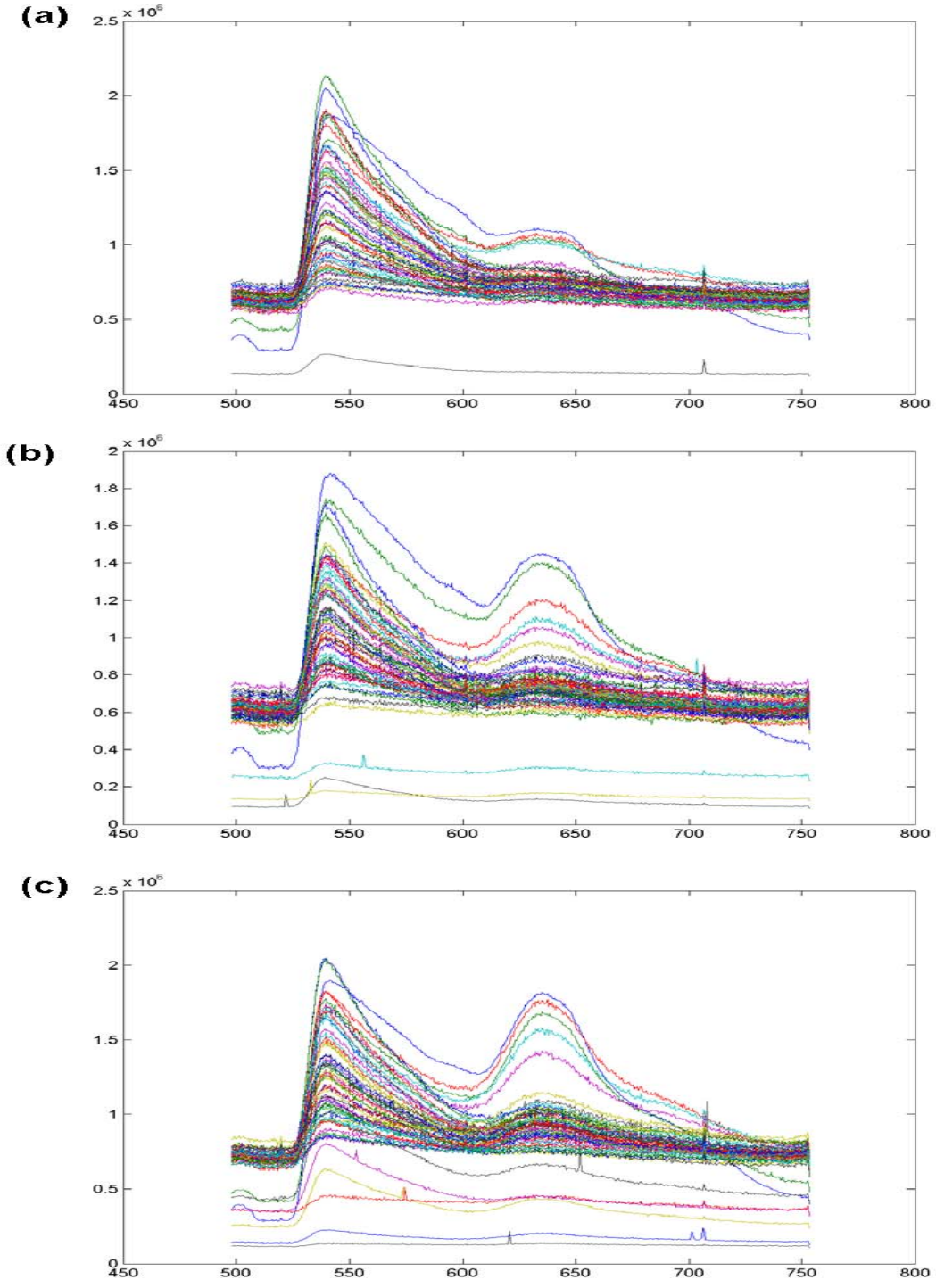

Figure 4.7 CFSE and Atto590 under 488nm illumination.

Chapter 5
Unmixing Experiments

The main aim of this thesis was the analysis of multispectral images, which means dealing with images that do not necessary correspond to the same fluorophore. In that case, in order to use the theory mentioned before, we need to separate the different fluorescent signal contained in an image. In this chapter, we are going to present spectral unmixing, a method that can separate the mixed fluorescent signal to its components, and finally separate the fluorophores.

5. 1 Spectral unmixing

We are going to examine the case of having more than one fluorophores with overlapping spectra in the investigated sample. The resulting fluorescent concentrations will include signal from all the fluorophores of the sample. In a similar way, as we have used two different fluorophores with close fluorescence spectra, the resulting fluorescence reconstruction which we will take after the Labview processing, will include signal from both the fluorophores. We want to have the fluorescence signal only of the one fluorophore each time, that's why we need a tool to do it. This tool is called unmixing spectra and is a simple code written in Matlab [7, 24]. The main idea of the method is the following:

We have two fluorophores (CFSE and Atto 590 in our case) and we have choose two spectral bands for detection the fluorescence signal emerged from the surface of the sample (we call them detection channel). Initially, we have to measure the fluorescence signal of each fluorophore separately and determine the contribution of the fluorophore to the detection channel we have (we call them spectral strengths). Then we express the fluorescence contribution of its fluorophore in each channel as a linear contribution of the two fluorescence concentration multiplied with the appropriate spectra strength.

For example in Figure 5.1 we can see the fluorescence spectra of our two fluorophores and the filters we have used.

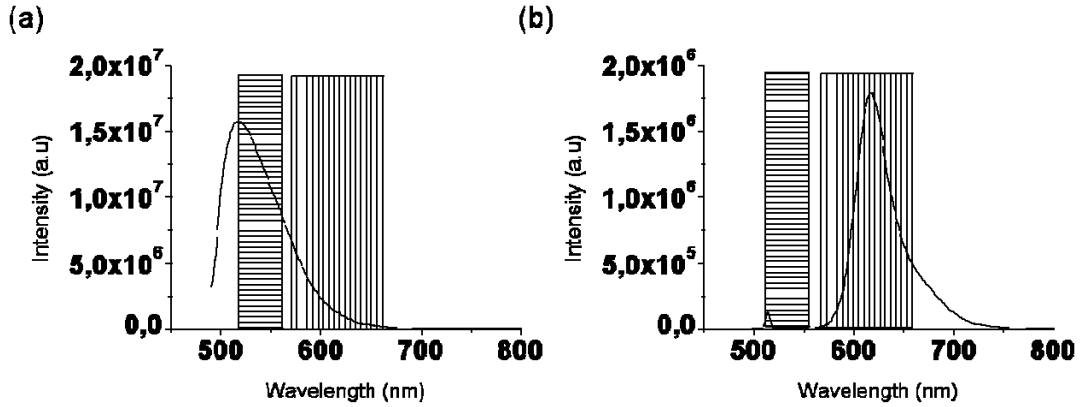

Figure 5.1 Spectra of (a) CFSE and (b) Atto590 with the detection channels of our experiments.

The fluorescence reconstructions in each detection channel will correspond to the following linear equations:

$$I_g = g_{CFSE} C_{CFSE} + g_{Atto590} C_{Atto590}$$
$$I_r = r_{CFSE} C_{CFSE} + r_{Atto590} C_{Atto590} \qquad (5.1)$$

where I_g, I_r are the fluorescence reconstructions in the detection channels for CFSE and Atto 590, g_{CFSE}, $g_{Atto590}$, r_{CFSE} and $r_{Atto590}$ are the spectral strengths of CFSE and Atto 590. C_{CFSE} and C_{Atto} are the unknown reconstructed fluorescence concentrations of each fluorophore.
If we wrote the previous system in the form of matrix we would take:

$$\begin{bmatrix} I_g \\ I_r \end{bmatrix} = \begin{bmatrix} g_{CFSE} & g_{Atto590} \\ r_{CFSE} & r_{Atto590} \end{bmatrix} \times \begin{bmatrix} C_{CFSE} \\ C_{Atto590} \end{bmatrix} \qquad (5.2)$$

The spectral strengths are calculated by integrating the signal under the part of the curve that corresponds to the spectral band allowed by each filter. In this way if we consider as $g(\lambda)$ the excitation signal for the CFSE and $r(\lambda)$ the excitation signal for Atto590, the spectral strengths could be defined as:

$$
\begin{aligned}
g_{CFSE} &= \int_{520nm}^{560nm} g(\lambda)d\lambda \\
g_{Atto590} &= \int_{520nm}^{560nm} r(\lambda)d\lambda \\
r_{CFSE} &= \int_{570nm}^{660nm} g(\lambda)d\lambda \qquad (5.3) \\
r_{Atto590} &= \int_{570nm}^{660nm} r(\lambda)d\lambda
\end{aligned}
$$

where in our case was:

$$
\begin{aligned}
g_{CFSE} &= 0.2058 \\
r_{CFSE} &= 0.000418 \\
g_{Atto590} &= 0.0761 \qquad (5.4) \\
r_{Atto590} &= 0.8798
\end{aligned}
$$

The solution of the system producing the unknown concentrations is:

$$
\begin{bmatrix} C_{CFSE} \\ C_{Atto590} \end{bmatrix} = \begin{bmatrix} g_{CFSE} & g_{Atto590} \\ r_{CFSE} & r_{Atto590} \end{bmatrix}^{-1} \times \begin{bmatrix} I_g \\ I_r \end{bmatrix} \qquad (5.5)
$$

5.2 Unmixing methods

Two different unmixing methods were studied for the separation of the two fluorophores differentiate by the type of data is applied on. The first is applied on the reconstructed 3D data while the second is applied on the raw 2D data. Each one of these methods was applied by using two different matrixes of spectral strengths one comes from the measured spectrums and one comes from the calculated spectrum. In this way, we finally have 2 different methods of unmixing, with each one of having two cases.

5.2.1 Unmixing the reconstructed data (UnmixRec)

In this method the unmixing process is applied on the reconstructed data. Reconstruction are performed separately for each detection channel providing the two reconstructed images for the green and the red detection

channel which correspond the two fluorophores. Then the unmixing calculations described above are performed to obtain the independent 3D images of the two fluorophores.

In order to process the reconstruction data in this mode, we have used two different ways. First we use the spectral strengths that we have calculated from measuring the two fluorophores in the fluorimeter (we will call this as unmix tubes I). Secondly, we have used the mean values of the spectral strengths that we calculate from the measurement of the spectra we take during the experiments (we will call this as unmix tubes II).

5.2.2 Unmixing the raw data (UnmixData)

In this method the unmixing process is performed directly on the raw experimental data before the reconstruction. The same algorithm described above is performed to get the unmixed raw data which are saved as an image stack. The processing is performed the same way as with FMT data producing though the final unknown unmixed fluorescence concentrations.

To process our data with this mode, we have used three different ways. First we use a matrix which consists of the spectral strengths that we have found from measuring the two fluorophores in the fluorimeter (we call this as unmix raw I). Secondly, we use the matrix with the mean spectral strengths that we calculate from the measurement of the spectra we took simultaneously with the FMT measurements (we call this unmix raw II).

Finally, we try to separate the fluorophores with the unmixing processing performed in the raw data source by source, taking into account the appropriate spectral strengths for each source. We will take the unmixed fluorescence concentrations (unmix source to source).

5.3 Spectral strengths

The spectral strengths that we used for our experiments are being calculated with two different methods:

5.3.1 Measured spectra

The first uses values which are fixed for each fluorophore through out all experiments. These values were calculated by measuring tubes with known concentration of each fluorophore in a commercial fluorimeter. Emission spectra were recorded by exiting the fluorophores at the same wavelength used in the FMT. Then from the emission curves, the four spectral strengths are obtained by integrating at the appropriate detection area for both fluorophores.

The emission spectrum for the CFSE is presented in Figure 5.2 while the equivalent for Atto590 is presented in Figure 5.3.

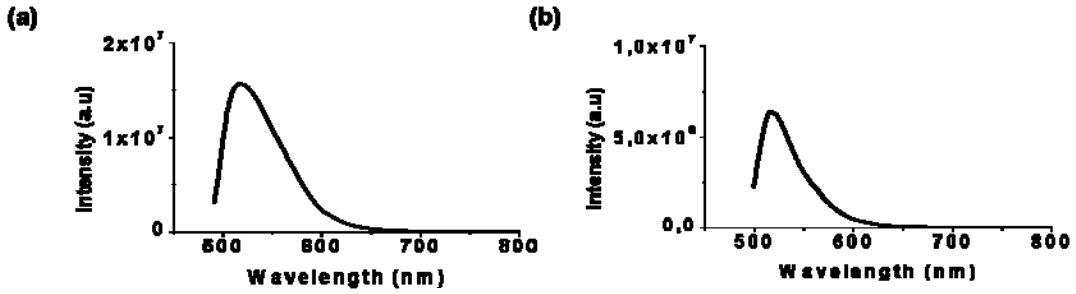

Figure 5.2 Emission spectrums for CFSE (a) at 488nm and (b) at 514nm

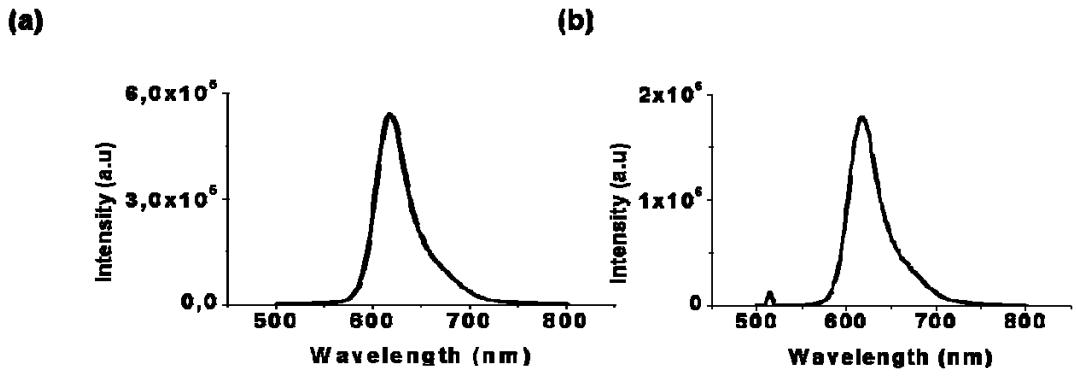

Figure 5.3 Emission spectrums of Atto 590 (a) at 488nm and (b) at 514nm

5.3.2 Calculated spectra

The second method employed a deconvolution process using the spectra that were obtained by the spectrograph in real time during the experiments and the spectra from the fluorimeter.

Deconvolution is an algorithm-based process used to reverse the effects of convolution on recorded data. Generally speaking, the polynomial multiplication and division correspond to the operations convolution and deconvolution. However, since convolving two sequences is the same as multiplying their Fourier transforms, the deconvolution process will be similar to the invere Fourier transform. This fact is very useful in recovering the input to a known filter, given the filtered output. In a similar way, we can deconvolve a spectrum in order to find out the different spectrum-components it is comprised of. We have used a matlab algorithm to process our multispectral data. The syntax in Matlab for deconvolution is given by:

$$[q, r] = deconv(a, b) \qquad (5.6)$$

where the a is the the polynomial dividend, b is the divisor, q is the quotient, and r is the remainder. As we can see this equation deconvolves vector b out of vector a, using long division.

In our experiments we have used two fluorophores with overlapping spectra. Let us assume that $g(t)$ is the real signal for the green fluorophore, $r(t)$ is the real signal for the red fluorophore and $s(t)$ the signal that the spectrograph measures. In fact, this will be the convolved spectrum of the two fluorophores and can be written as:

$$s(t) = g(t) \otimes r(t) = \int_{-\infty}^{\infty} g(t-v)r(v)dv \qquad (5.7)$$

This operation is equivelant to a multiplication of the Fourier transforms of the two spectra:

$$S(f) = G(f) \cdot R(f) \qquad (5.8)$$

In order to obtain its components (the separate spectra of CFSE and Atto590) we have to deconvolve it, in other words make the following divisions using the Fourier transforms:

$$G(f) = \frac{S(f)}{r(f)} \qquad (5.9)$$

and

$$R(f) = \frac{S(f)}{g(f)} \qquad (5.10)$$

where $S(f), G(f)\ and\ R(f)$ are the Fourier Transform of the signals $s(t), g(t)\ and\ r(t)$ respectively and $g(f)\ and\ r(f)$ are the Fourier transforms of

the fluorimeter spectra. The inverse Fourier Transform of this will give us the desired spectra.

Figures 5.4 and 5.5 show a sample of how the spectrum recorded at 488nm and at 514nm can be deconvolved respectively. The deconvolution for all the sources is shown in figure A1 of the Appendix.

In order to deconvolve the spectra recorded with the CCD camera, we use a custom developed program in Matlab. The process involves loading the recorded spectrum for the sample for each case of 488nm and 514nm illumination (experimental). The spectrum of Atto590 and CFSE recorded by a spectrofluometer at each wavelength is then loaded as well (theoretical).

Next, the true spectrum is deconvolved from the experimental and the theoretical spectra. In this way, the division of the fluorescence spectrum with the theoretical one of the one fluorophore, will give us the fluorescence spectrum of the other fluorophore. So, for each laser beam we will take two different spectrums, one for each fluorophore.

The spectral strengths for each source are calculated by integrating the area in each detection channel as above.

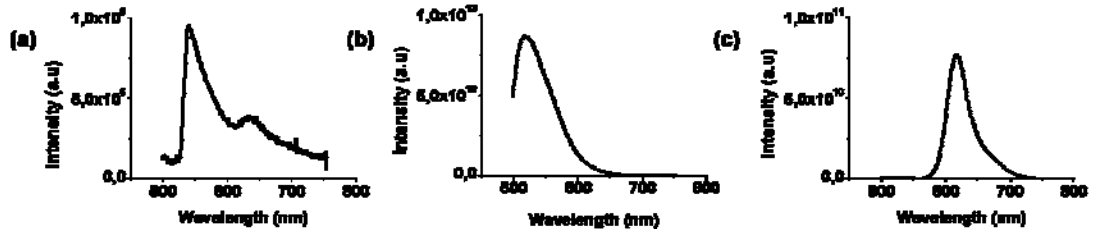

Figure 5.4 Deconvolution processing at 488 nm excitation.

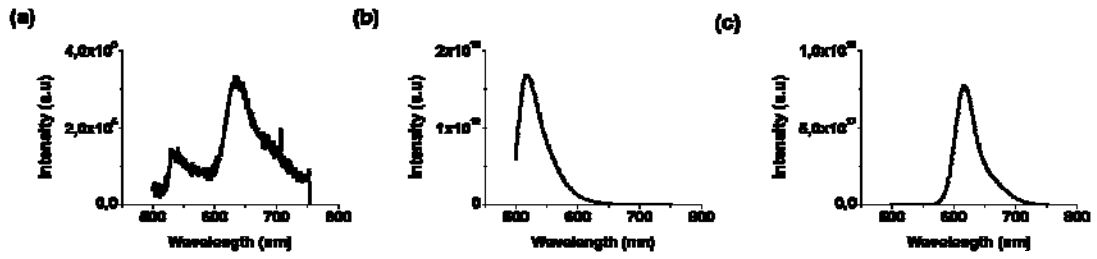

Figure 5.5 Deconvolution processing at 514 nm excitation.

5.4 Quantified data

In order to fully exploit the ability of FMT to calculate concentrations we converted the arbitrary values produced after the reconstruction into true concentration values. To that end, the unmixed raw reconstruction data were normalized by the quantum yield, the extinction coefficient and the path length of the tube for each fluorophore and for each excitation wavelength.

The fluorescence quantum yield (ΦF) is the ratio of photons absorbed to the photons emitted through fluorescence. In other words, the quantum yield gives the probability of the excited state being deactivated by fluorescence rather than by another, non-radiative mechanism. The extinction coefficient is the fraction of light lost to scattering and absorption per unit distance in the participating medium. Each fluorophore has a standard value for the quantum yield and for the extinction coefficient at a certain wavelength and certain environment.

In order to calculate these values for our experiments, we filled tubes with the fluorophores, and with the use of a spectro-fluorimeter we obtained the excitation spectrum of each fluorophore. From these curves by normalize with the max value of the curve, and by using the theoretically values from the manual of each fluorophore, we calculate the extinction coefficient and the quantum yield. The excitation spectra of the CFSE and Atto590 are shown in Figures 5.6.

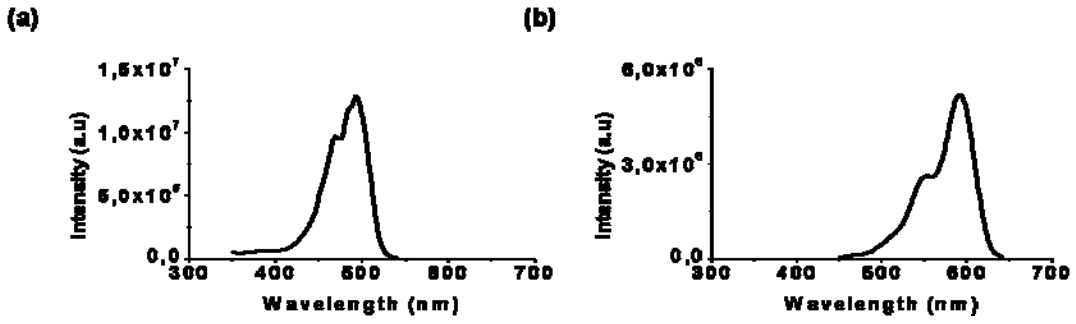

Figure 5.6 Excitation spectrums of (a) CFSE and (b) Atto590.

We found that the extinction coefficient for the CFSE was 75648 $(Mcm)^{-1}$ for the 488nm excitation and 5604 $(Mcm)^{-1}$ for the 514nm excitation. In an analogous way the extinction coefficient for the Atto590 was 22480 $(Mcm)^{-1}$ for the 488nm excitation and 18432 $(Mcm)^{-1}$ for the 514nm excitation. The path length that we used for both geometries was 1,2 cm.

Chapter 6

Results and Analysis

In this chapter we present the experiments we have performed. All experiments were made by using tissue like phantoms containing two different tubes since we wanted to compare and find the best method for spectral unmixing. A series of experiments was performed using mice with the two tubes inserted subcutaneously under the mammary fat pad in a study aiming at testing our algorithms in a realistic inhomogeneous environment.

In the first section, we present experiments concerning the spectrograph calibration and spectral resolution. Firstly, we present how the calibration is performed. Then, by using two different fluorophores, in two different distances between them and in two different heights according to the distance of the camera, we show how well the spectrograph can detect the fluorescence signal in two cases: when the same fluorophore is in both tubes, and when the tubes are filled with different fluorophores.

In the second section, we present the study of unmixing signals from different fluorophores that is based on the linear unmixing algorithm applied to spectral imaging as described in the previous chapter. Results of two fluorophores are presented: CFSE and Atto590.

Finally, we present results for the methods for the unmixing signal which are applied in a mouse model in order to test our previous results in a realistic situation.

6.1 Spectral calibration

Calibration is the process of establishing the relationship between a measuring device and the units of measure. In the case of the spectrograph the measured spectrum is given as intensity per pixel and thus we need to convert the pixel reading to the equivalent wavelength.

In order to do that, firstly, we set the null point of the spectrograph. (a null point is defined as the position where all spectral lines of the common mercury lamp are visible). At each position of the spectrograph we can see a specific region of wavelengths carefully chosen so that the fluorescence of both the fluorophores used in our experiments is visible.

For the calibration we have used the two characteristic lines of the mercury at 576.960nm and 579.066nm (double line) and at 546.074nm. We also used 2 laser lines at 514nm and 635nm for more accuracy. The results are presented below:

pixel	wavelength(nm)
481	514
415	546,074
353	578,013
238	635

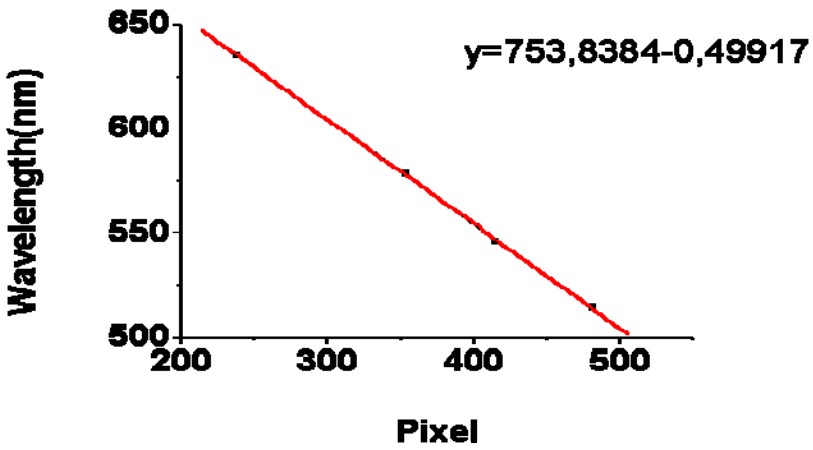

Figure 6.1 Calibration of the spectrograph using a mercury lamp and two laser lines

The relation between wavelength and pixels is calculated from the linear fit of the plot.

6.2 Spectrograph analysis

In order to see how well our spectrograph can detect the fluorescence signal we used two tubes filled with different fluorophores (CFSE and Atto590) in

three different pairs of concentrations (10μM CFSE and 20μM Atto590, 20μM CFSE and 20μM Atto590, and 20μM CFSE and 10μM Atto590) and at four different positions:

a) 3mm depth and 1mm distance
b) 3mm depth and 4mm distance
c) 6mm depth and 1mm distance and
d) 6mm depth and 4mm distance

We excited the fluorophores with the 488nm laser and the 514nm laser, signals recorded using a 60nm bandwidth filter centered at 480nm for the 488nm and a 10nm bandwidth filter centered at 510nm for the 514nm. The fluorescence signal using a 40nm bandwidth filter centered at 540nm and a 75nm bandwidth filter centered at 630nm was also recorded. The pattern of sources that we used was 5x9 sources, in a square of 100x200mm^2.

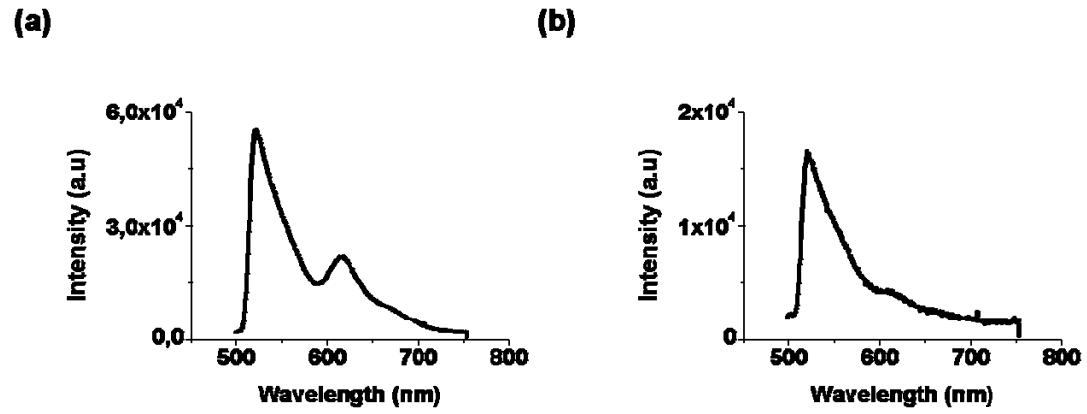

Figure 6.2 Representative spectrums at 488nm excitation (a) in the reflection geometry and (b) in the transmission geometry.

The results are shown in Figures 2-5 in the appendix A2. Representative measurements can be seen in figure 6.2 and 6.3 for the 488nm laser and for the 514nm laser respectively. Both measurements are for the case of the 4mm distance between the two tubes and at the 3mm depth under the surface of the sample. Index (a) corresponds to reflection geometry and index (b) to transmission geometry.

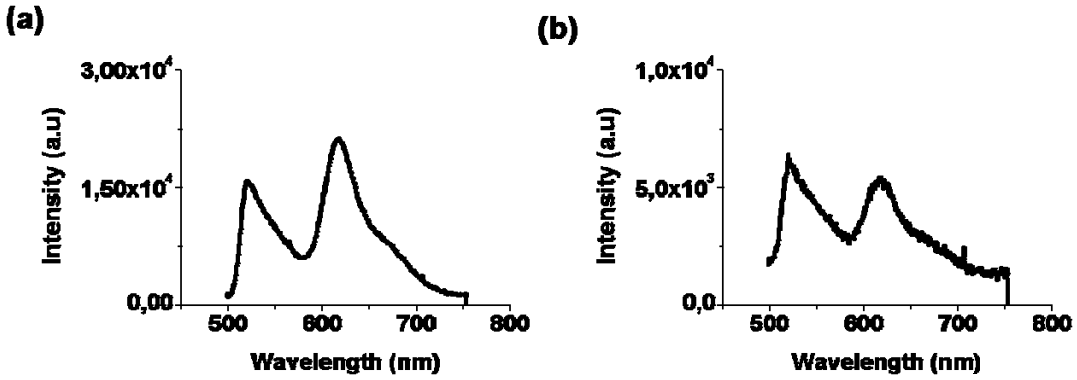

Figure 6.3 Representative spectrums at 514nm excitation (a) in the reflection geometry and (b) in the transmission geometry.

Then, we tried to see how well our spectrograph can detect the fluorescence signal if we put the same concentration of the same fluorophores together in two different tubes. In order to do this, we used again two tubes filled with the same concentration of the green fluorophore (CFSE) 4μM this time in the same positions:

a) 3mm depth and 1mm distance
b) 3mm depth and 4mm distance
c) 6mm depth and 1mm distance and
d) 6mmdepth and 4mm distance

We excited the fluorophores with the 488nm laser. The pattern of sources that we used was 5x9 sources, in a square of 100x200mm^2. The results are shown in figures 6 and 7 in the appendix A3. Again we can see representative spectra in figure 6.4 where index (a) is for the reflection geometry and index (b) for the transmission geometry.

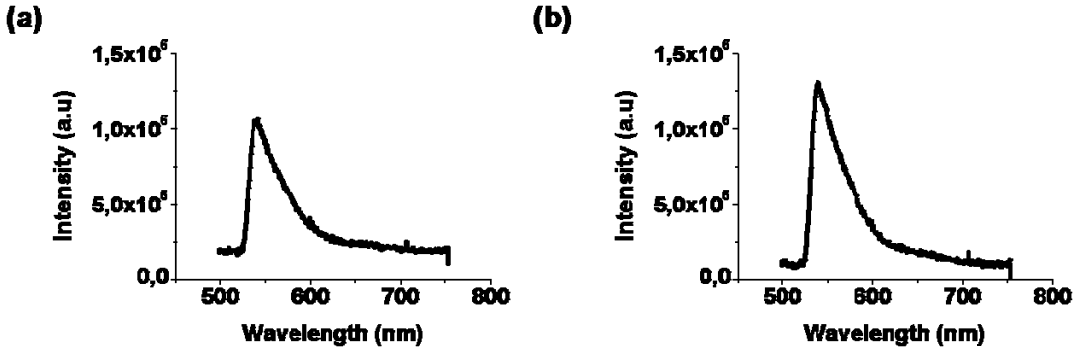

Figure 6.4 Representative spectrums at 488nm excitation in (a) reflection geometry and (b) transmission geometry.

Finally, we check the ability of the spectrograph to detect the signal from two tubes that were in the same position but in different depths. Therefore, we filled the tubes with the same concentration of the fluorophore (4μM) and we put the tube filled with CFSE at 3mm depth under the surface of the sample and the one filled with Atto 590 at 6mm depth under the surface. The sample was excited with the 488nm laser and the 514nm laser, and we took measurements from both geometries. The pattern of sources that was used was 4x15 sources in a square of 60x300mm^2.

Representative spectra of the results are seeing in figure 6.5 for the 488nm laser, while the results for the 514nm laser are shown in figure 6.6. The results for all sources are shown in the appendix A4 in figure 8.

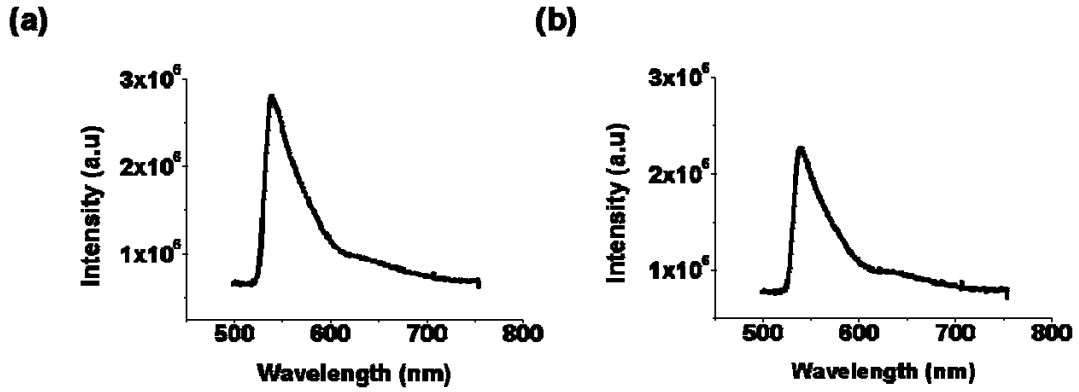

Figure 6.5 Representative spectrums at 488nm excitation for the (a) reflection geometry and for the (b) transmission geometry.

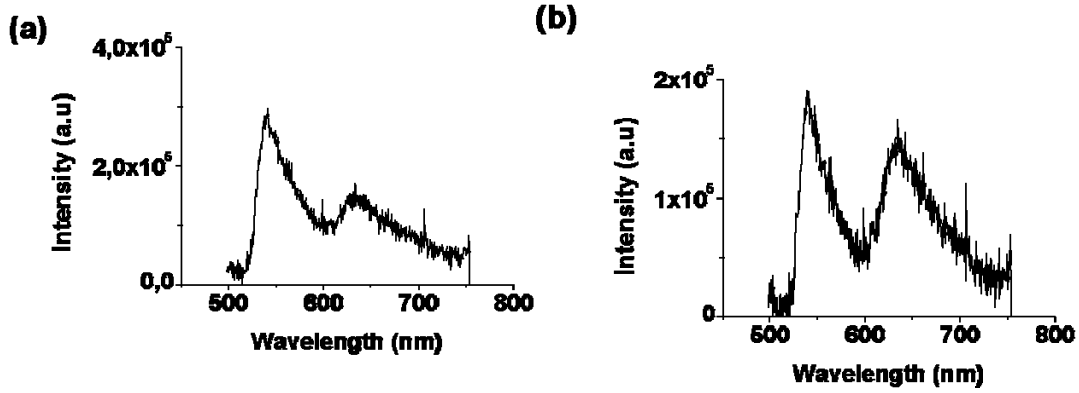

Figure 6.6 Representative spectrums at 514nm excitation for the (a) reflection geometry and for the (b) transmission geometry.

6.3 Unmixing process in vitro.

In order to asses and compare the different ways of unmixing we used two fluorophores with overlapping spectra. The CFSE had a fixed concentration of 4μM and the Atto 590 in three concentrations 5μM, 10μM and 15μM. The experiments were performed both in reflection and transmission geometry, using a 5 x 12 sources in an area of 100mm x 250mm. The height from the CCD camera was 15cm, and the two tubes were placed in the sample at 7mm distance and 3mm below the surface.

We illuminated the sample by using two different wavelengths at 514nm and at 488nm while fluorescence was recorded using two filters: a 40nm bandwidth filter centered at 520nm and a 90nm bandwidth filter centered at 615nm for green and red respectively. The excitation signal of the laser was taken by a 10nm bandwidth filter centered at 510nm in the case of the 514nm illumination, and with a 60nm bandwidth filter centered at 480nm for the case of the illumination at 488nm.

The results are seeing in figures 6.7-6.10. In figure 6.7 we see the reconstructions for 4μM concentration of CFSE and 5μM concentration of Atto 590 at the reflection geometry at 514nm excitation. Figure 6.8 shows the reconstructions for 4μM concentration of CFSE and 5μM concentration of Atto 590 at the reflection geometry at 488nm excitation. Figure 6.9 show the reconstructions for 4μM concentration of CFSE and 5μM concentration of Atto 590 at the transmission geometry for the 514nm excitation and finally figure 6.10 shows the results for the 488nm excitation for the transmission geometry.

All figures correspond to the 4μM concentration of CFSE and 5μM concentration of Atto 590, while the other pairs of concentrations are seeing in appendix A5 respectively. For all figures, (a) and (b) show the reconstructions of the two fluorophores before the unmixing for the green and red detection channel respectively. (c) and (d) show the reconstruction results after UnmixRec (see Chapter 4) using the fixed spectral strengths for the green and red detection channels respectively. (e) and (f) represent the results for the UnmixRec using the mean deconvolved spectral strengths for the green and red detection channels respectively. (g) and (h) show the

results after UnmixData using the fixed spectral strengths for the green and red channels respectively. Finally, (j) and (i) represent the unmixing after UnmixData using the mean deconvolved spectral strengths for the green and red channels respectively.

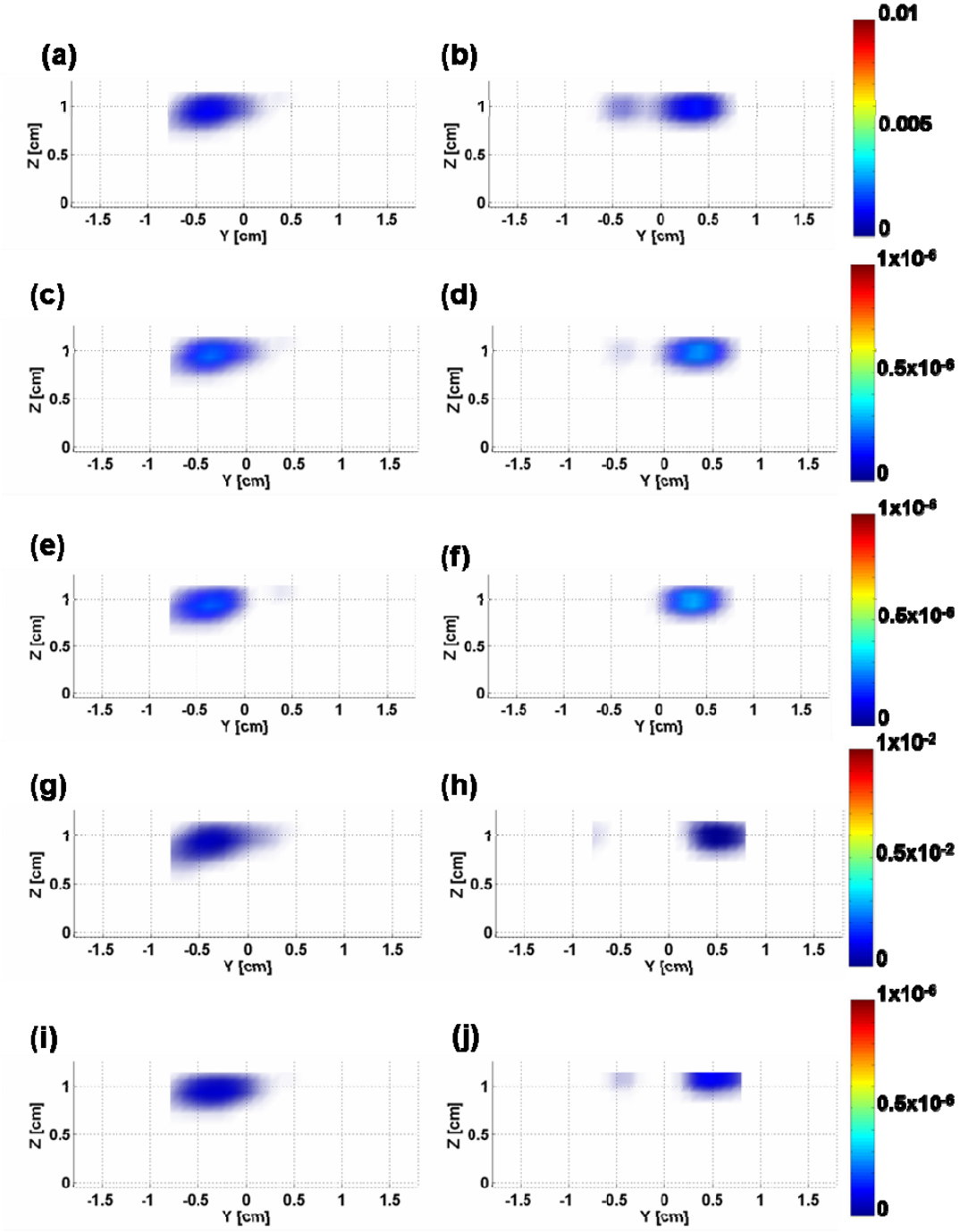

Figure 6.7 Reconstructions for the illumination at 514nm in the reflection geometry for 4μM CFSE and 5μM Atto590.

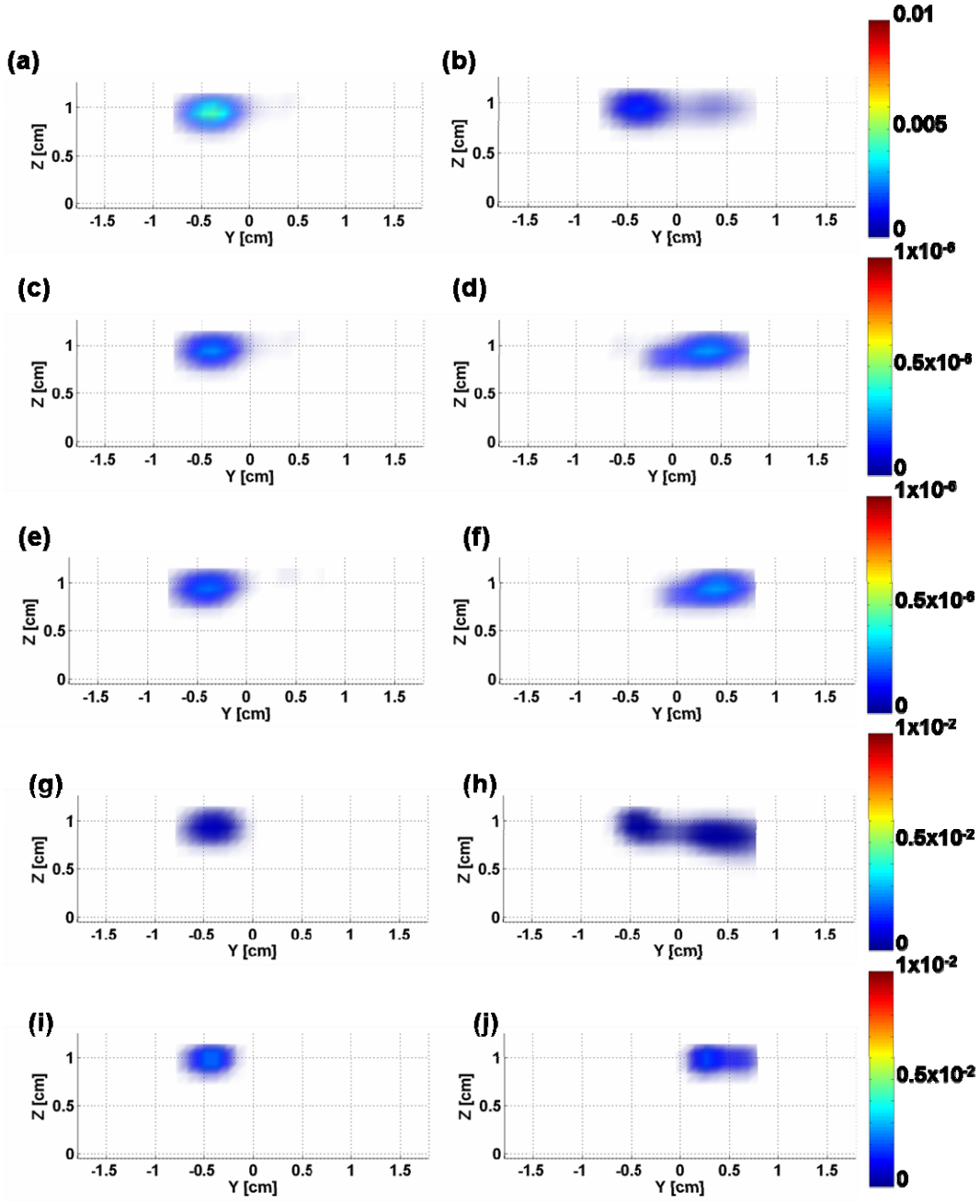

Figure 6.8 Reconstructions for the illumination at 488nm in the reflection geometry for 4µM CFSE and 5µM Atto590.

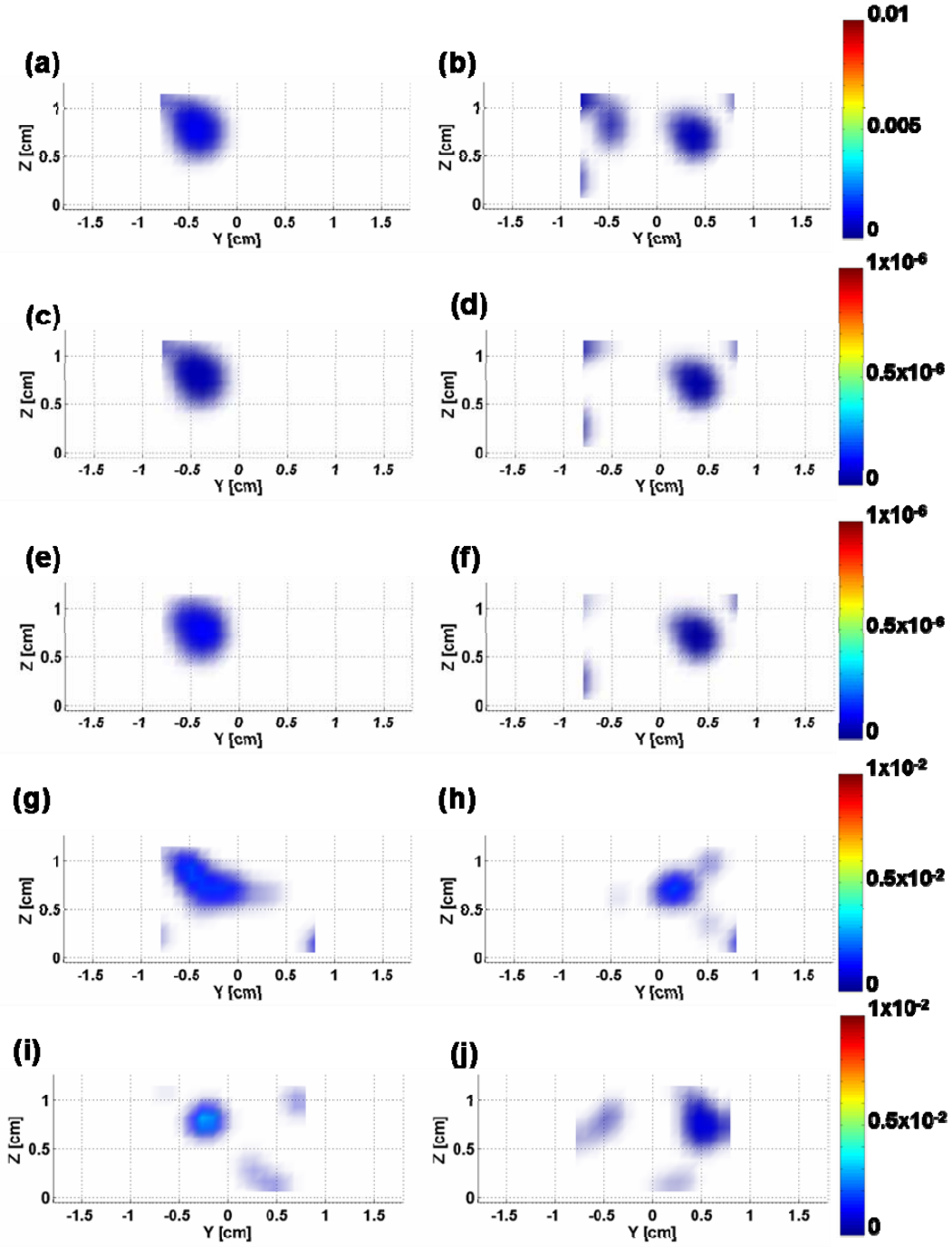

Figure 6.9 Reconstructions for illumination at 514nm in the transmission geometry for 4μM CFSE and 5μM Atto590.

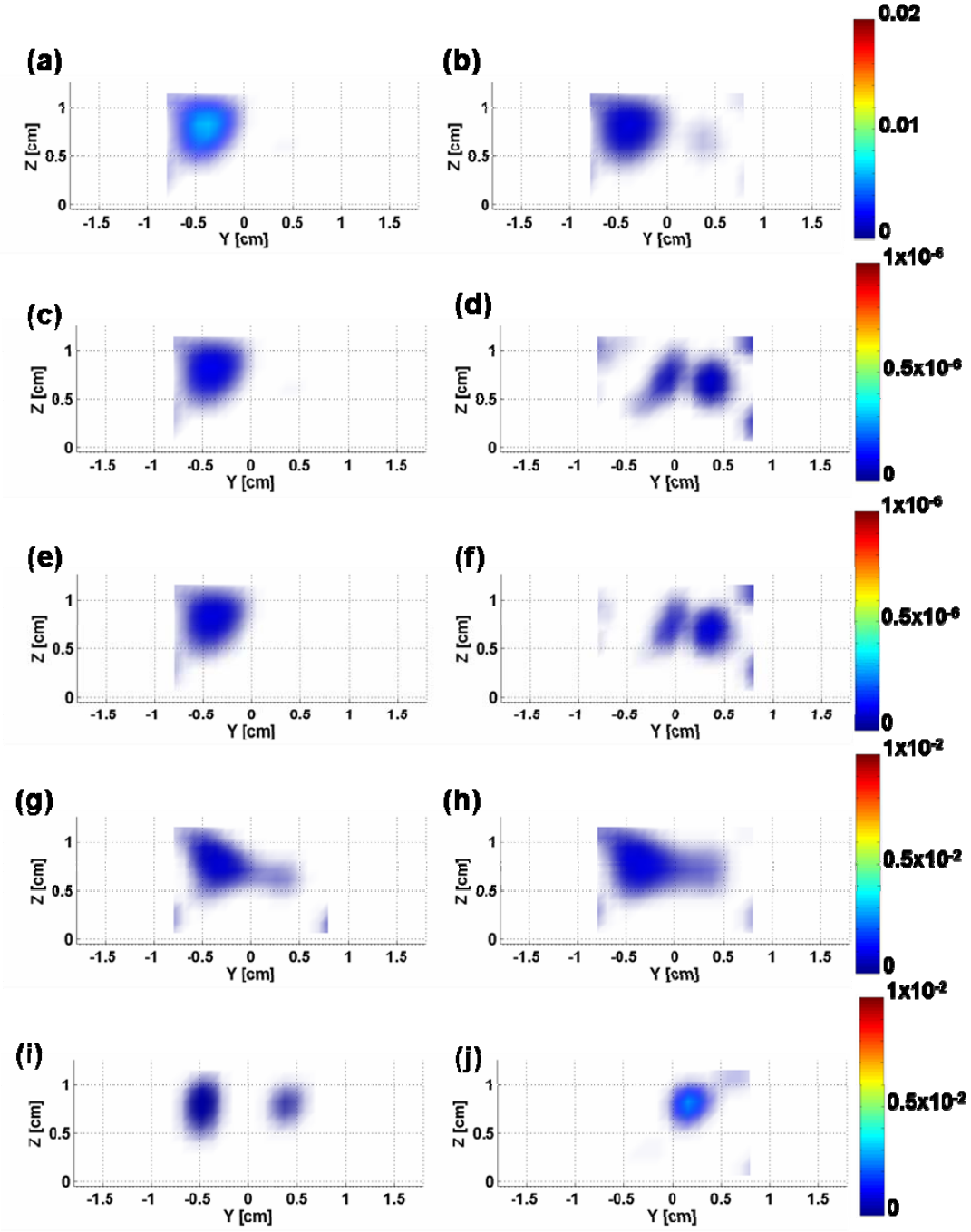

Figure 6.10 Reconstructions for illumination at 488nm in the transmission geometry for 4μM CFSE and 5μM Atto590.

The concentrations obtained from ROIs from the above 3D reconstructions are presented in Figure 6.11- 6.14 for the 4μM concentration of CFSE and for the 5, 10, and 15 μM concentrations of Atto590. Figure 6.11 corresponds to the reflection geometry for the 514nm excitation, Figure 6.12 deals with the reflection geometry at 488nm excitation. Figures 6.13 and 6.14 are for the transmission geometry at 514nm and 488nm respectively.

The y axis shows the mean reconstructed concentrations, as they were calculated from the 3D images, and the x axis shows the pairs of the two fluorophores. At each graph there is also the equation for the linear fit for the concentration of Atto 590. In picture (a) we see the mixed fluorescence signal before the unmixing processing. In picture (b) we can see the concentrations show the reconstruction results after UnmixRec using the fixed spectral strengths. In picture (c) represent the concentration for the UnmixRec using the mean deconvolved spectral strengths. In picture (d) we can see the concentrations after UnmixData using the fixed spectral strengths. Finally, figures (e) represent the concentrations from the unmixing after UnmixData using the mean deconvolved spectral strengths for the green and red channels respectively.

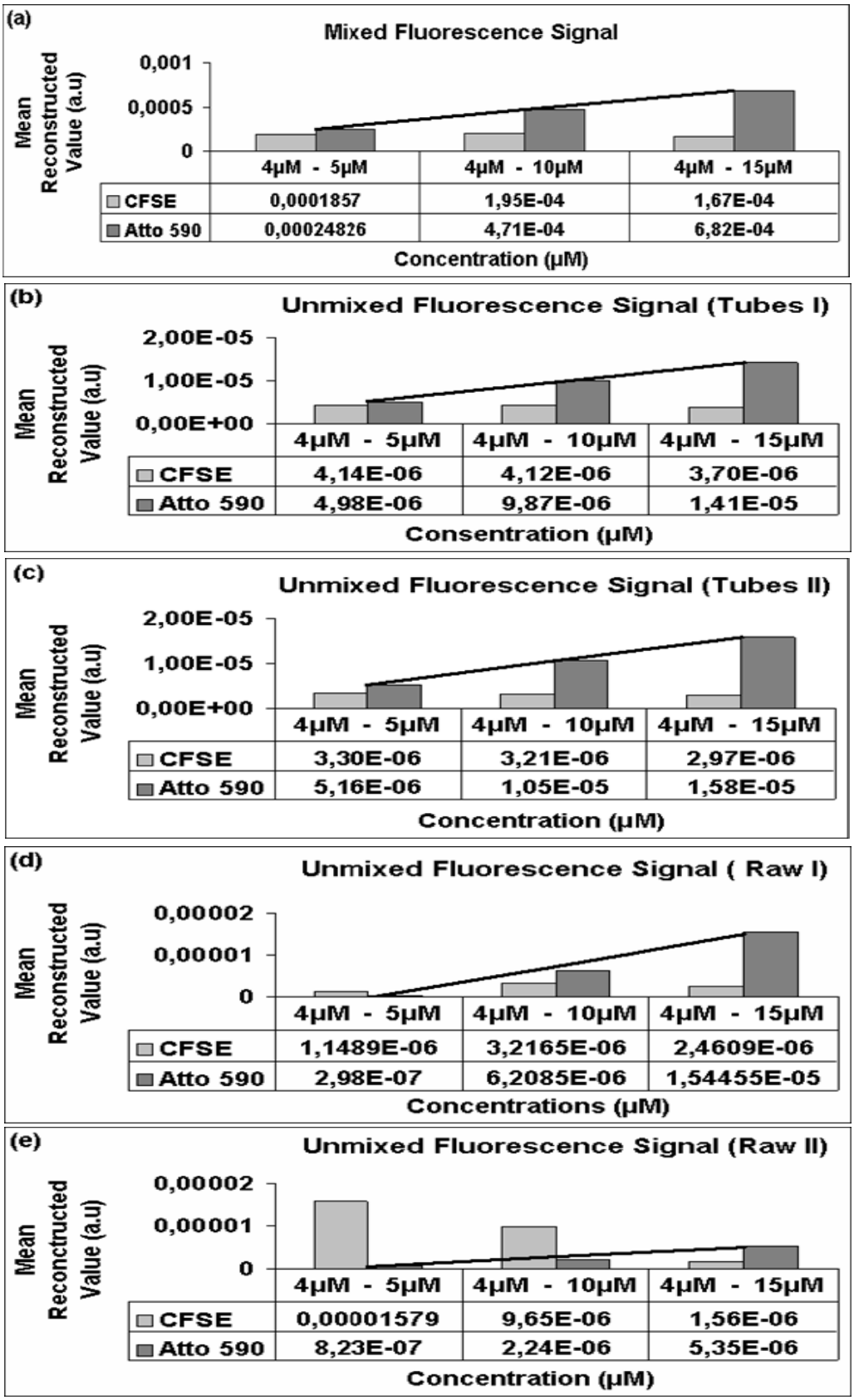

Figure 6.11 Graphs of the mean reconstruction values versus the concentration in the reflection geometry for the illumination at 514nm.

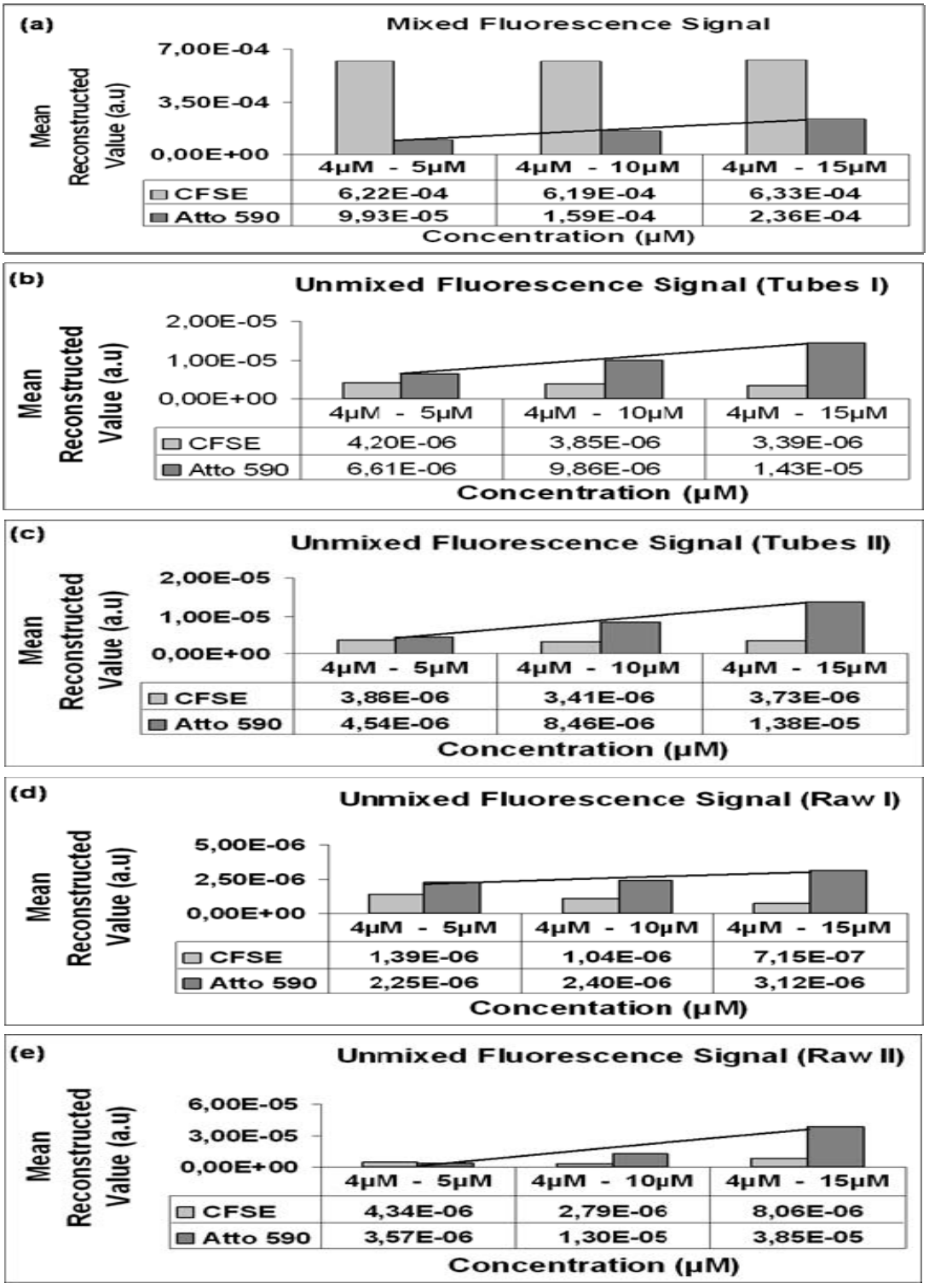

Figure 6.12 Graphs of the mean reconstruction values versus the concentration in the reflection geometry for the illumination at 488nm.

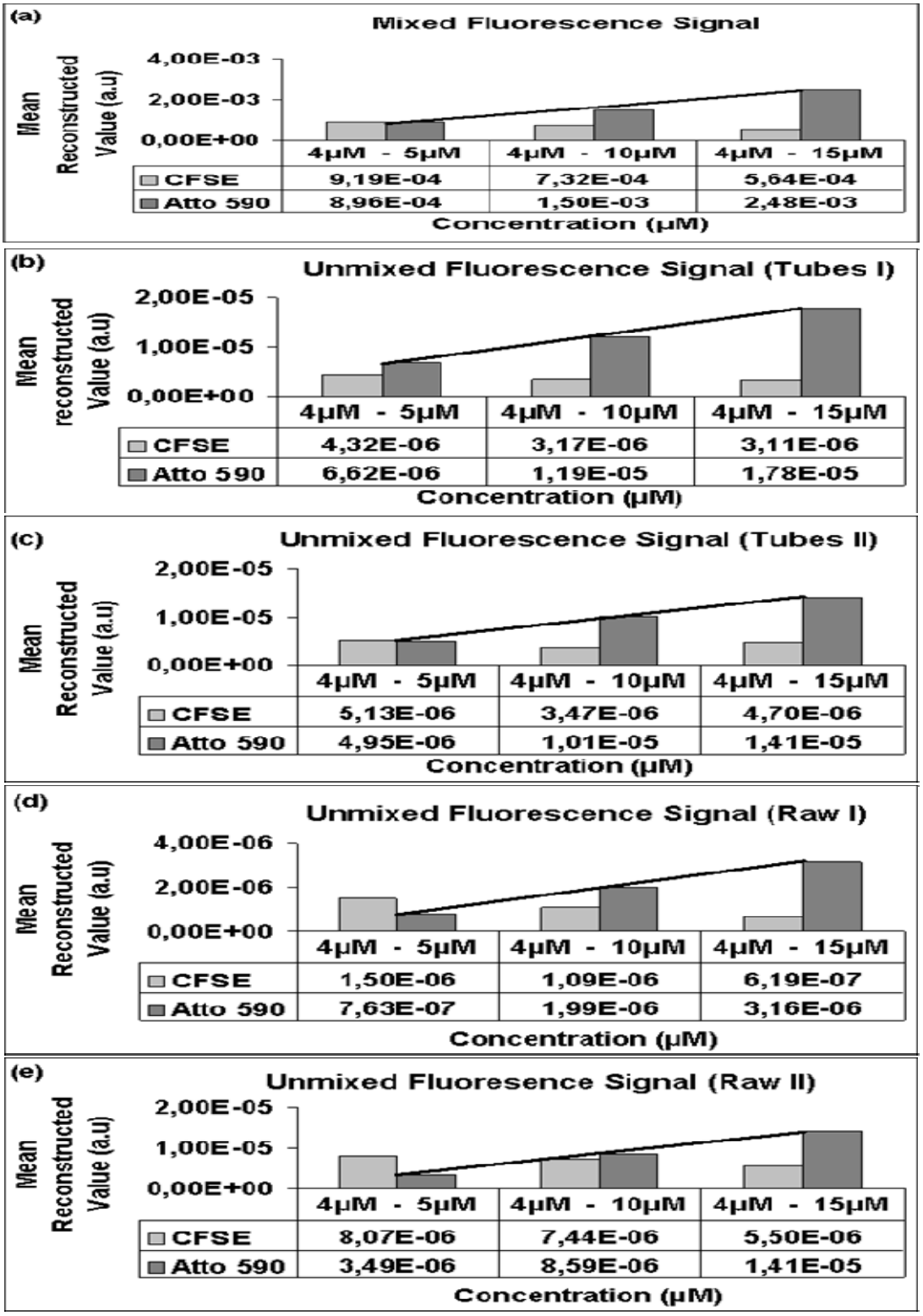

Figure 6.13 Graphs of the mean reconstruction values versus the concentration in the transmission geometry for the illumination at 514nm

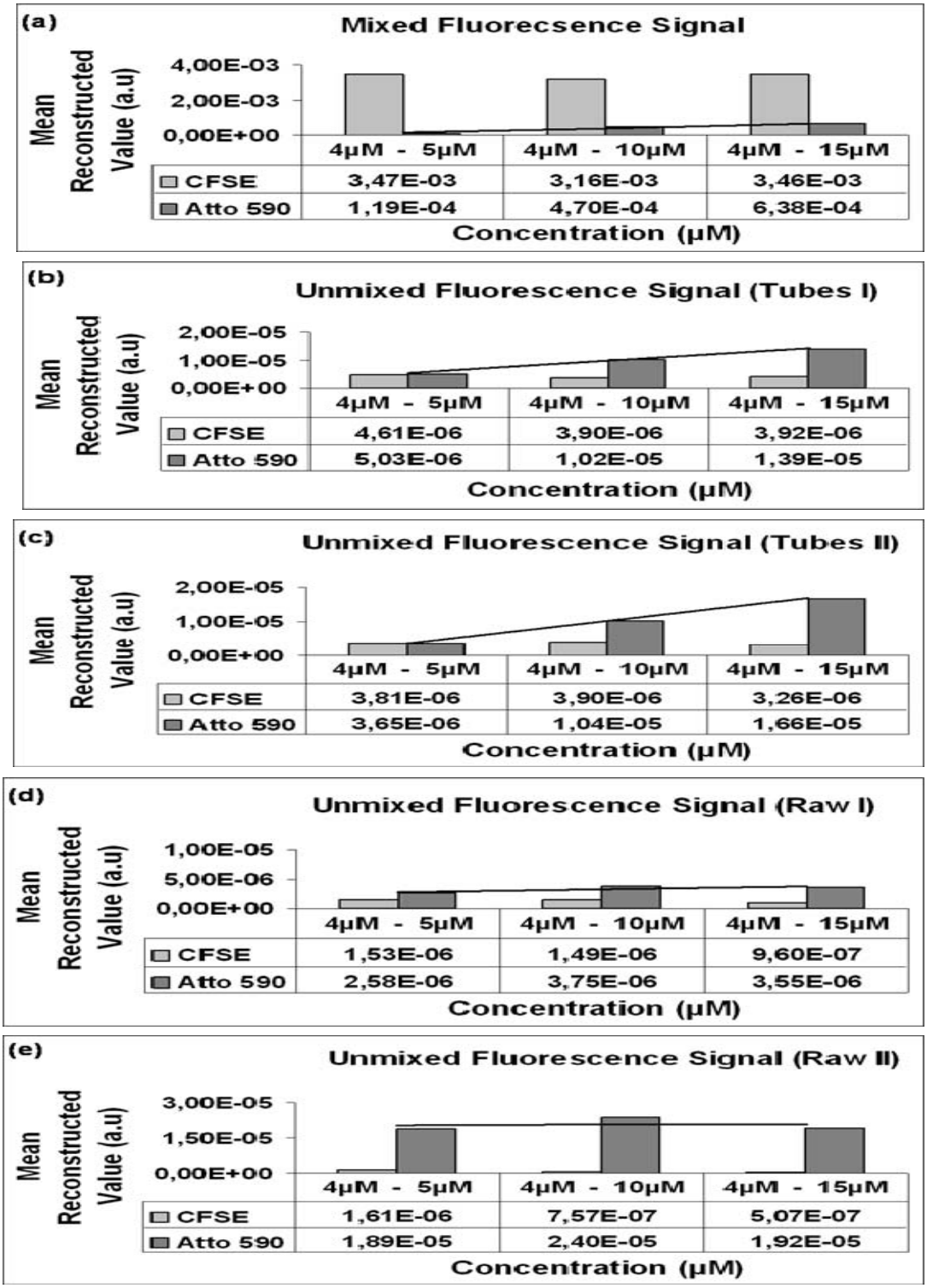

Figure 6.14 Graphs of the mean reconstruction values versus the concentration in the transmission geometry for the illumination at 488nm

As we already know from previous studies [29] when we use one fluorophore at a time we can have a very accurate quantification of the recovered concentration. Also when using two tubes with the same

fluorophore the setup can distinguish the two tubes with sub millimeter resolution. Let us see what happened when the two tubes are filled with different fluorophores.

So, In order to control and compare our results, we first had to perform some checks, such as the distance between the two tubes and the depth below the surface of the phantoms. As we can see from the reconstruction figures, the distance between the two tubes is correct, in both reflection and transmission. As far as the depth where the tubes were placed is concerned, we noticed that it is different, depending of the geometry. In the reflection geometry, the tubes are reconstructed at 0.3mm under the surface of the phantom, while in the transmission geometry they are reconstructed at 0.45mm under the surface. This is quite normal, as usually in the reflection geometry the signal tends to appear in a smaller distance from the surface of the sample than the real one, due to the fact that more reflections happen in the surface of the phantom. On the other hand, in transmission geometry the depth can be more accurate, but with more noise, as the laser beam is propagating through the sample.

Next step was to compare and contrast the reconstruction figure that we took after the data processing. Let us start with the illumination of the sample with the 514nm laser beam. First of all, we noticed that we could see the mixed fluorescence signal from both fluorophores only in the red detection channel. In the green detection channel, we can see the mixed signal only for the CFSE. This is quite logical, because the illumination of our sample with the 514nm laser, excites both fluorophores. According to the excitation measurement of the dyes, Atto590 begins to emit at 510nm with a peak of maximum excitation at 624nm, in contrary to the CFSE which is begins to emit at 480nm and has the maximums excitation at 517nm. This means that in the green detection channel, which is from 520nm to 560nm the most signal comes from the CFSE and only little signal we there was from the fluorescence of Atto 590, which is not enough for both tubes to appear. On the other hand, the red detection channel is from 570nm to 660nm and in this region of wavelengths we could see clearly the signal from both fluorophores. Of course, appears Atto 590 to be stronger.

As we can see from the pictures above, in the reflection geometry when we do the unmixing processing in the reconstruction data with the fix spectral strengths we have a very good separation of the two fluorophores, even thought there is a very low residual signal of the green fluorophore in the red detection channel. Of course, if we use the mean spectral strengths the unmixing is better and the residual green signal has disappeared. From the reconstructions in the raw data, we can see that if we use the fix values of spectral strength even thought in the red detection channel the separation exists, in the green detection channel there is a signal from the red fluorophore, which there was not before. As far as the unmixing with the mean values of the spectral strengths is concerned, we have a very good separation in both detection channels.

If we look at the concentrations we take in each case we can see that the unmix in the reconstruction data, not only gives us the proportion in the concentration of the Atto 590 but also gives us the right concentrations. Unfortunately, we can not tell the same in the unmixing in the raw data, were we the concentration of CFSE is reconstructed much bigger than that of Atto 590. Furthermore, the proportion of Atto 590 is not correct as we do not have the increase we want. Interesting is also the fact that when we tried to do the unmix processing with the mean values of the spectral strengths we did not take a constant concentration for the CFSE.

Similar conclusions can be reached, if we examine the data obtained at the 488nm illumination. As we can see from the mixed fluorescence reconstruction signal, the concentration of CFSE is much bigger than that of Atto 590. Moreover, we can say that although in the green detection we can see the signal only from the CFSE; in the red detection channel we have clearly the fluorescence signal from both tubes. In fact, the tube filled with the green fluorophore is more profound than the Atto590 one. This can be easily explained because the absorption peak for the CFSE is at 480nm and we illuminate it at 488nm, very close to that peak. In this way, we expect to have a very strong fluorescence signal from the CFSE. On the other hand, as at 488nm illumination our red fluorophore does not absorb very much, it is expected that the fluorescence signal in the red detection channel will be low, especially for the 5μM.

Let us start from the reflection geometry. As we can see from the unmixed reconstruction pictures when we do the unmixing processing in the reconstruction data with the fix spectral strengths we have a good separation of the two fluorophores, even thought there is a very little signal of the green fluorophore in the red detection channel. In contrary to this if we use the mean values of spectral strengths in the matrix, the unmixing is much better and the green signal in the red detection channel does not exist. We can not say the same for the unmixing processing in the raw data. From the reconstructions in the raw data, we can see that if we use the fix values of spectral strength there is no separation of the tubes in the red detection channel. Furthermore, in the green detection channel there is a signal from the red fluorophore (especially for values more than 5μM concentrations), which was not there before. As far as the unmixing with the mean values of the spectral strengths, we can say that we have a good separation in both detections channels.

If we look at the concentrations we take in each case, we can see that at this laser beam at 388nm illumination, the concentration of the CFSE before the unmixing is almost four times bigger than those of Atto590. Notable is the fact that after the unmixing process both fluorophore have almost the same concentrations. To be more specific, the unmixing processing in the reconstruction data, gives us the right proportion in the concentration of the Atto 590 and also the right ratio of concentrations between the two fluorophores. This happens not only if we use the fix values of the spectral strengths but also if we use the matrix with the mean values. Again, we can not tell the same in the unmixing in the raw data. If we use the matrix of the fix values of spectral strengths we obtain a constant concentration for both CFSE and ATTO590. Furthermore, if we use the mean values the concentration of the CFSE is not constant and Atto590 increases much quickly than in reality.

As we can see from the pictures, in the transmission geometry for the 514nm excitation, the reconstructions before the unmixing have more noise than that we had in the reflection geometry. The processing of unmixing in the reconstruction data was very good, as the separation of the fluorophores is successful, for both cases of the matrix with the spectral strengths we had.

Unfortunately, we can not say the same and for the noise, which continues to exist in our pictures. The unmixing processing in the raw data not only did not separate the fluorophores in the red detection channel, but neither did in the green. This also happens for both cases, not only for the fix values of spectral strengths but also for the mean values of spectral strengths.

If we look at the concentrations we take for each case, we see that the concentrations from the unmixing in the reconstruction data represent the real concentrations even thought if we use the fix spectral strength we take a little bit bigger concentration for the Atto 590. The concentrations from the unmixing processing in the raw data are bigger for CFSE than Atto 590 in both cases. To be more specific, if we use the fix spectral strength we have a decrease in the concentration for CFSE, and the concentration for Atto 590 is not increasing proportional. If we see the mean spectral strength, the concentration for CFSE is constant but the concentrations for the red fluorophores did not have the real increasing.

As we can see from the pictures in the transmission geometry for the 488nm illumination, the reconstruction pictures before the unmixing again have more noise than that we had in the reflection geometry. Also, it is quite hard to see the tube with the red fluorophore in the red detection channel, especially for the lower concentration of Atto590. The processing of unmixing in the reconstruction data was not very good, as the separation of the fluorophores is not happened. In contrary to this in the red detection channel we can see more clearly the two tubes. There is no difference of this in both cases of the matrix of spectral strengths. Moreover, the unmixing processing in the raw data also gives similar results. If we use the matrix with the fix values of spectral strength the tubes can not be separated in the red detection channel. The only good thing is that the signal that came from the Atto590 is a little bit bigger than that before the unmixing. Finally, if we do unmix in the raw data with the mean values of spectral strengths we can see the Atto590 in the red detection channel, but now there are two tubes in the green detection channel.

If we look in the concentrations in the transmission geometry we can see that also in this geometry the concentration of the CFSE before the unmixing is much bigger that that of Atto 590. Furthermore, after the

unmixing processing in the reconstruction data for both cases the concentrations are correct. We have the right proportion of the increase in the concentration of the Atto 590. Also, the ratio between the two fluorophores is correct. This is very strange, as the reconstruction for these unmixing were not correct. What is more, if we do unmix in the raw data for both cases, we take that not only the concentration of the CFSE is constant but also the concentration of the Atto590. Of course, we can not accept this.

6. 3 Unmixing Process in vivo.

In order to compare the previous results, we try to repeat the same experiment with the same concentrations of the two fluorophore but inserted in a mouse. The first thing was to shave the area that was going to be exposed to the laser, because the mouse has a black fur that could lead to an attenuation of the detected fluorescence light. Then, the mouse was placed in anesthesia with the use of Isoflurane, and the two tubes were placed under the mouse's skin in upper torso area. Finally, the living sample was placed inside the imaging system.

The pattern of sources that we used was 5x8 sources, in a square of 100x300mm^2. For the excitation of the sample 3 laser lights were used. The sample was excited at 514nm, 488nm and 458nm. The last excitation was taken in order to take the autofluorescence signal from the sample. The geometry that was used was the reflection only as in such low values of illumination is too difficult for the light to propagate the body of the sample and reach the surface so as the camera to detect the emission signal. The results are seeing in the following figures.

Figures 6.15-6.16 correspond to the 514nm and 488nm excitation respectively. To be more specific, 6.15 shows the reconstructions for 4μM concentration of CFSE and 5μM concentration of Atto 590, while Figure 6.16 is the reconstruction pictures for 4μM concentration of CFSE and 5μM concentration of Atto 590 at 488nm excitation. The rest of the pairs of concentrations are seeing in the appendix A6 in Figures 17-20.

In both figures, in picture (a) and (b) we can see the reconstructions of the two fluorophores before the unmixing processing where in picture (a) is

the signal from the green detection channel and picture (b) is the signal we take from the red detection channel. Pictures (c) and (d) show the reconstruction results after the unmixing in the raw data using the fix matrix of spectral strengths. In picture (c) we see the results from the green detection channel and in picture (d) the results from the red detection channel. Pictures (e) and (f) represent the results for the unmixing in the raw data by using the mean matrix of spectral strengths, where picture (e) is again from the green detection channel and picture (f) is for the red detection channel. Next two pictures (g) and (h) show the results after the unmixing processing in the reconstruction data using the fix matrix of spectral strengths; (g) and (h) are the green and red channel of detection respectively. In a analogous way, pictures (j) and (i) represent the unmixing processing in the reconstructed data with the mean weights of spectral strength, (i) for the green detection channel and (j) for the red one. Next 4 pictures (k), (l), (m) and (n) show the unmixing in the reconstructed data after the autofluorescence signal has been removed. Picture (k) has to do with the green detection channel and picture (l) with the red one, when in the unmixing algorithm we have used the fix matrix of spectral strengths. Finally, picture (m) and (n) are for the mean values of spectral strengths and is for the green and the red detection channel respectively.

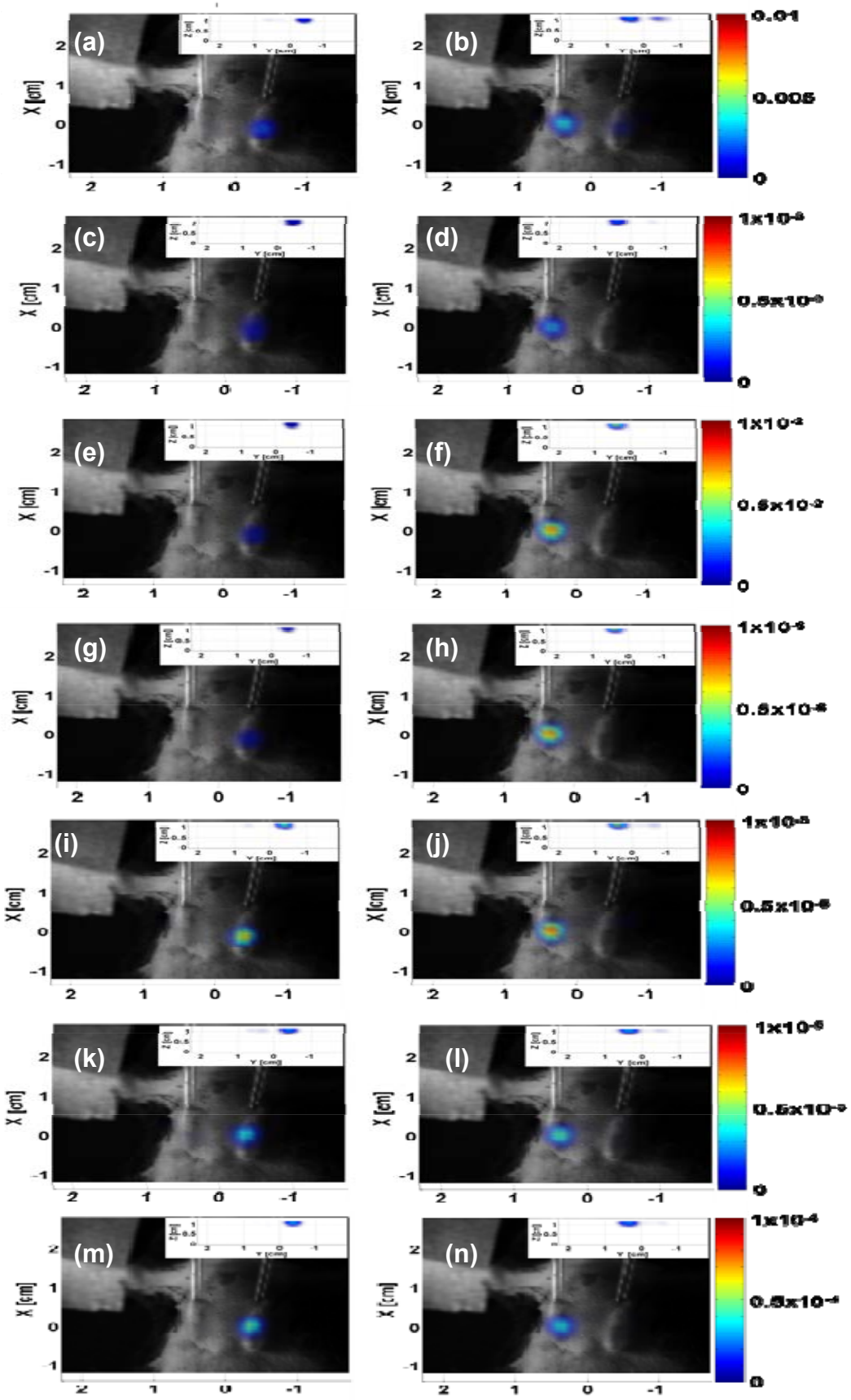

Figure 6.15 illumination at 514nm, 4μM CFSE and 5μM Atto590

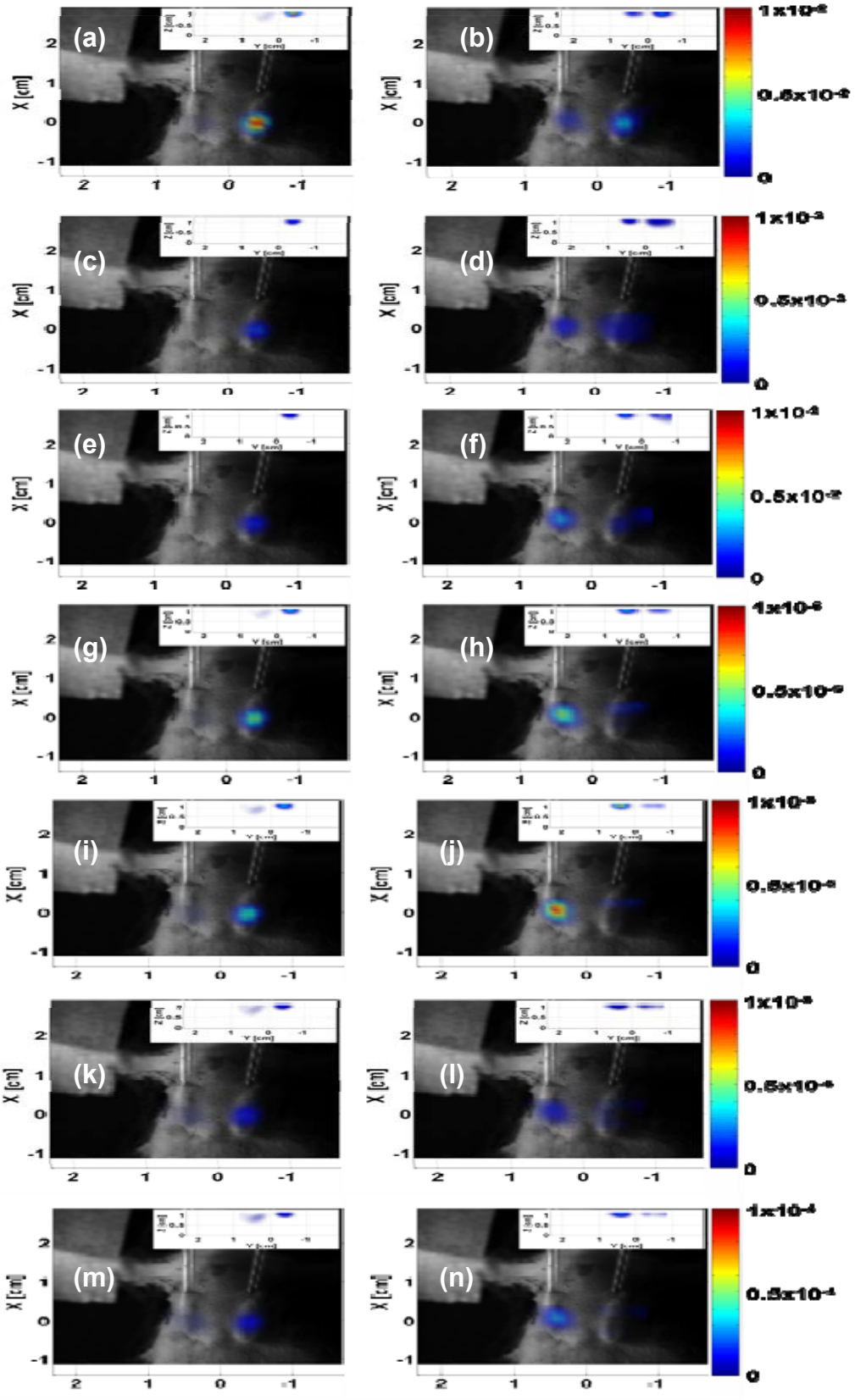

Figure 6.16 illumination at 488nm, 4μM CFSE and 5μM Atto590

In figures 6.17 and 6.18 we can see the graphs for the reflection geometry for 4μM concentration of CFSE and 5, 10, and 15 μM concentrations of Atto 590 in the form of histograms for the 514nm excitation and 488nm excitation respectively. In the y axis there are the mean reconstructed concentrations, as they were calculated by the Labview environment, and in x axis there are the pairs of the two fluorophores. At each graph there is also the equation for the linear fit for the concentration of Atto 590. In picture (a) we see the mixed fluorescence signal we took before the unmixing processing. In picture (b) and (c) we can see the concentrations after the unmixing in the raw data, where picture (b) has to do with the fix values of the matrix and picture (c) is for the matrix with the mean spectral strengths. The concentrations we took from the unmixing in the reconstructed data of the experiments and for the fix values of the matrix with the spectral strengths are shown in picture (d), while the concentrations for the unmixing in the raw data for the mean spectral strengths are shown in picture (e). Finally, in pictures (f) and (g) we can see the concentrations we take after the unmixing in the reconstructed data when we have removed the autofluorescence signal, and picture (f) is with the use of the matrix with the fix values of spectral strengths and picture (g) is when we used the mean values of spectral strengths. Finally, picture (m) and (n) are for the mean values of spectral strengths and is for the green and the red detection channel respectively.

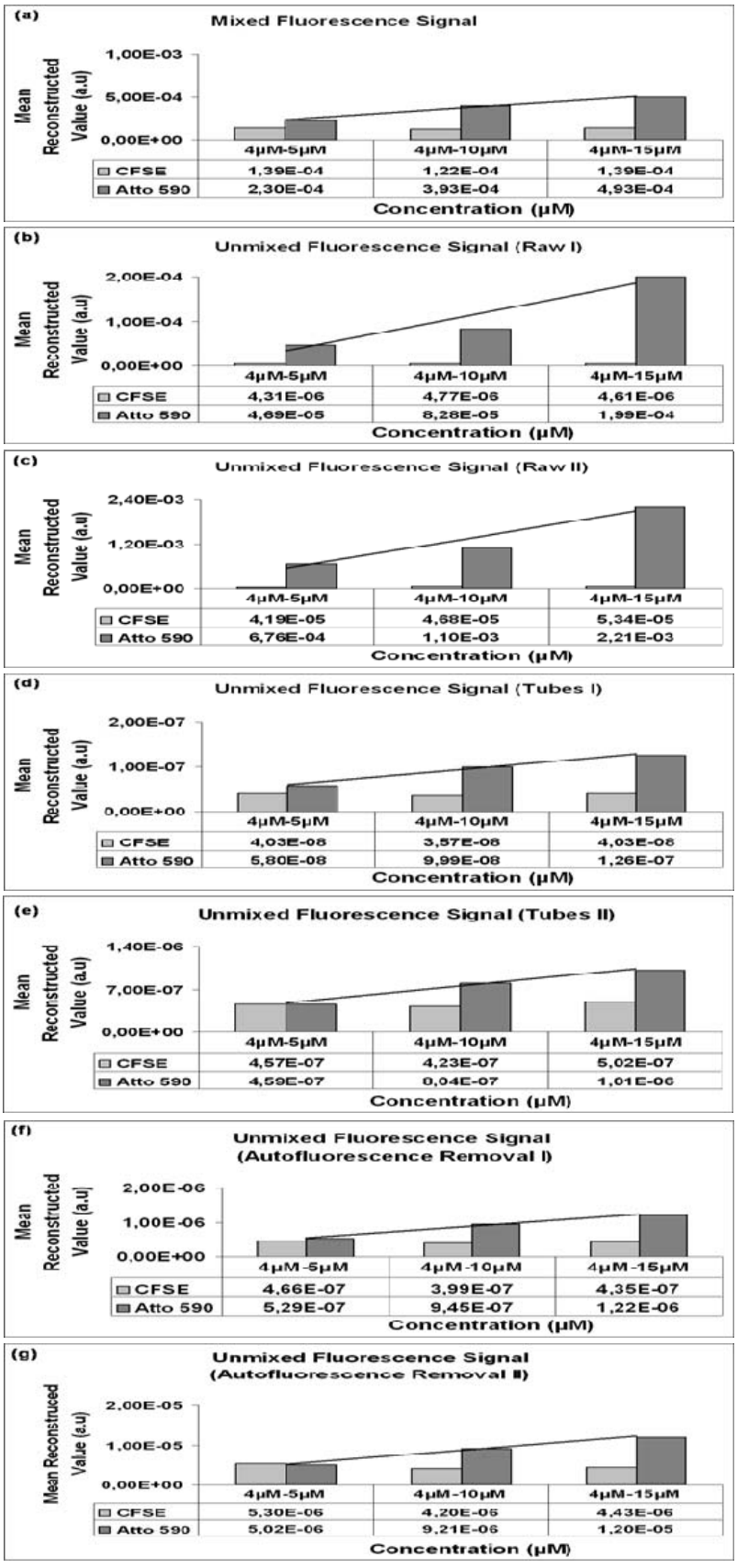

Figure 6.17 Graphs of the mean reconstruction values versus the concentration in the transmission geometry for the illumination at 514nm.

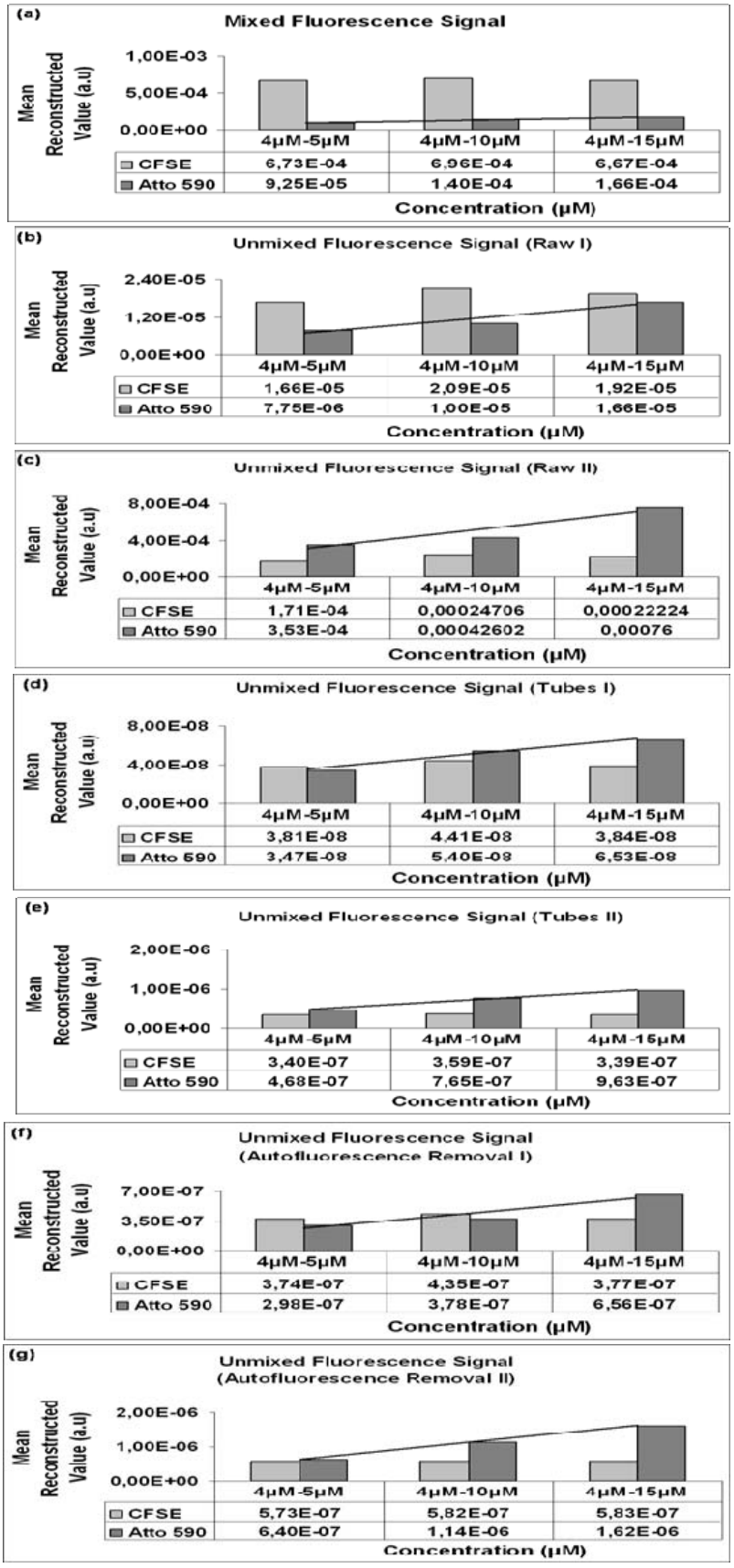

Figure 6.18 Graphs of the mean reconstruction values versus the concentration in the transmission geometry for the illumination at 488nm

We can reach similar conclusions with the unmixing processing in tubes if we look the experiments with the mouse. As we can see for the 514nm excitation again we can see signal from both tubes only in the red detection channel. According to the reconstructed pictures the unmixing processing is generally good. Even if the signal does not totally disappear, there is an obvious decrease of its value, especial when we use the mean values of the spectral strengths. Even though, the best way for the unmixing was this time when we do the unmixing processing in the reconstructed data after the autofluorescence signal has been removed.

If we look at the concentration that the processing gives us, we can see the concentrations after the unmixing in the raw data is not good. The Atto590 is almost four times bigger than the CFSE for both case of the matrix of the spectral strengths. The proportion for the Atto590 exists, but does not increase with the right rhythmus. However, it is much closer to the reality than that of the phantom. In contrary to this, the concentrations for the other cases are much better. We take almost the right values for both fluorophores and the right proportion for the Atto590.

As far as the 488nm laser is concerned, the mixed fluorescence signal that we take appears not only in the red detection channel but also in the green especial for the biggest values of the concentration of the Atto590. Unfortunately, none of the unmixing methods could give us the result we wanted, the separation of the two fluorophore.

Chapter 7
Conclusions and future studies

In this chapter we are going to present some conclusions about our study. Firstly, we will discuss the ability of our spectrograph to detect the emission spectrum of our sample. Then, we present the general result from the unmixing process that we have used in order to separate the two fluorophores and we will suggest the best way of spectrally unmixing in the overlapping spectrum of the fluorophores depending the sample we have.

7.1 Spectrograph

For the case that we have two tubes filled with different fluorophore, we can see that when the illumination of the sample happened at 514nm, both tubes can be detected even if the distance between them is 1mm. We can reach the same conclusion for the bigger depth under the surface of the phantom. The spectrograph can detect them clearly in both geometries: reflection and transmission. On the other hand, we should notice that in the transmission geometry lower values of intensity were detected.

The illumination at 488nm, did not give us such a good results. In fact only the green fluorophore (CFSE) could be easily detected. We could hardly see the red fluorophore in all sources. Although, we could have a satisfied signal for 3mm depth independently the distance between the two tubes. Unfortunately, the increase of the depth below the surface of the phantom makes the intensity to decrease. Especially in transmission geometry the optical fiber could not detect any signal.

What is more, we can say that the spectrograph can detect the fluorescence signal even if comes from the same fluorophore in two different tubes. This is quite clear from the difference in the intensity for each source. We can see that the intensity between the two tubes takes much lower values than those when the laser beam is on one of the two tubes. This happens for both geometries and for all the position we tried it.

Finally, we can see that the spectrograph not only can detect the fluorescence signal when the tubes are in different position but also when they are in the same position. In figure 6.8 we can see that the illumination at 514nm gives us a clearly separation of the fluorescence signal for both geometries. Of course, when the illumination happens with the 488nm laser this can not be happened as the Atto590 absorbs very little.

7.2 Unmixing experiment

As we see from the pictures, each laser represents one of our two fluorophore. In this way, we can see the difference in the fluorescence spectrum for each fluorophore depending on the illumination wavelength. So, at the 488nm illumination of the sample we take a very strong signal for the CFSE in comparison to the 514nm illumination of the sample that give us a good (not strong) signal for Atto590. In fact, we can say that with the 514nm laser we can almost take portion between the two fluorophore if we look the quality, not the quantity. Moreover, another common characteristic is that in both cases the red detection channel can give us signal from both tubes. However, for reasons that we have already been mentioned, at the 488nm laser the tubes are clearly than those of the 514nm laser.

Comparing the two different ways of unmixing, we could say that finally the unmixing processing when is applied in the reconstruction data is more effective and accurate when it is applied in the raw data, for both geometries. This may happen because it is more difficult two separate the signal of the fluorophores in the raw data, as the new raw data we will take, have to be divided, with the intrinsic signal of the laser, which will not have been changed. In this way, maybe the signal, which will be measured, will not be correct. Furthermore, unmixing in reconstruction data is more simple and quickly, because we have already reconstructed the data by values, which are experimentally correct, as they are the values which we had measured in the lab, and suit well.

Last but not least, we could also say that the unmixing using the experimental values of the matrix with the spectral strength is more accurate

than the fix values. This happens because the values for the strengths are taken directly for each experiment, and represents the unique situation of our sample for its source. They are taken for the right concentration of the fluorophores and the scattering and absorption medium which are taken part in our experiments. The fix values, which are come from the measurements in the spectrofluometer, represent a more ideal system where no other factor such as the absorption coefficient, the scattering coefficient will exist. Of course, in the case of the in vivo experiment the best way of unmixing is that when we have taken also into consideration and remove the autofluorescence signal that came from the skin of the mouse.

If we look for a next step for this kind of experiments, we can wonder of how the reconstruction map and the unmixing processing can be applied when the two tubes are placed in different depths under the surface of the phantom. It would see if the quantification of the fluorophore continues to exist, and we could compare we the previous one. Furthermore, it will be interesting of we could try the same technique but we 3 tubes this time. Perhaps the usage of 3 different fluorophores will not work, but I believe that if there were only to fluorophores in the three tubes alternately, we could do again applied successfully the unmixing algorithm.

Ευχαριστίες

Η παρούσα διπλωματική εργασία εκπονήθηκε στο εργαστήριο της ομάδα ‘’In vivo optical imaging group’’ του Ιδρύματος Τεχνολογίας και Έρευνας (ΙΤΕ) στα πλαίσια του μεταπτυχιακού προγράμματος του Τμήματος Φυσικής του Πανεπιστημίου Κρήτης: Μικροηλεκτρονική – Οπτοηλεκτρονική. Μέσα από την εργασία αυτή απέκτησα γνώσεις και εμπειρίες που πιθανόν να μου αποβούν σημαντικές στην μετέπειτα πορεία μου.

Θα ήθελα να ευχαριστήσω για αυτό το λόγο καταρχάς τον επιβλέποντα καθηγητή μου Δρ. Jorge Ripoll, που με εμπιστεύτηκε επιτρέποντας μου τη είσοδο στα εργαστήρια και με δέχτηκε στην ομάδα του.

Έπειτα θα ήθελα να ευχαριστήσω τον Στέλιο Ψυχαράκη, ο οποίος ήταν αυτός που με ενημέρωσε σχετικά με τα πειράματα και το εργαστήριο γενικότερα και μου έλυνε τις απορίες μου από την αρχή της ένταξης μου στην ομάδα.

Πάνω από όλα οφείλω ένα μεγάλο ευχαριστώ στον Δρ. Ιωάννη Ζαχαράκη, ο οποίος με καθοδηγούσε σε όλα τα σταδία της εργασία. Ήταν υπομονετικός και ανεκτικός μαζί μου. Κοιτούσε πάντα τα αποτελέσματα μου. Με συμβούλευε ώστε να διορθώνω τις ελλείψεις μου και να προχωρήσω με περισσότερες γνώσεις, αυτοπεποίθηση και με την δυνατότητα για καλύτερα αποτελέσματα. Στην πραγματικότητα χωρίς αυτόν δεν θα είχε ολοκληρωθεί ποτέ αυτή η εργασία.

Επίσης δεν θα μπορούσα να παραλείψω να ευχαριστήσω την Rosy Favvichio, τον Ανίκητο Γαροφαλάκη και τον Juan Aguirre που με βοήθησαν στην κατανόηση της πειραματικής διαδικασίας στα εργαστήρια.

Γενικότερα, χαίρομαι παρά πολύ που ήμουν μέλος στην συγκεκριμένης ομάδας καθώς όλα τα μέλη της ήταν αξιόλογα, πολύ ευγενικά, συνεργάσιμα και έτοιμα πάντα να με βοηθήσουν σε κάθε δυσκολία που προέκυπτε.

Τέλος θα ήθελα να ευχαριστήσω τον μπαμπά μου Στυλιανό και τους φίλους μου για την υπομονή και ανοχή που κάνανε μαζί μου όλο αυτό τον καιρό.

References

1. Graves, E.E., et al., *A submillimeter resolution fluorescence molecular imaging system for small animal imaging.* Med. Phys., 2003. **30**: p. 901-911.
2. Zacharakis, G., et al., *Volumetric tomography of fluorescent proteins through small animals in vivo.* Proc. Natl. Acad. Sci. U.S.A, 2005. **102**: p. 18252 - 18257.
3. Ntziachristos, V., et al., *Looking and listening to light: the evolution of whole-body photonic imaging.* Nat. Biotechnol., 2005. **23**: p. 313 - 320.
4. Pogue, B.W. and M.S. Patterson, *Review of tissue simulating phantoms for optical spectroscopy, imaging and dosimetry.* J Biomed Opt, 2006. **11**(4): p. 041102.
5. Cubeddu, R., et al., *A solid tissue phantom for photon migration studies.* Phys Med Biol, 1997. **42**(10): p. 1971-9.
6. Pogue, B.W., et al., *Image analysis methods for diffuse optical tomography.* J Biomed Opt, 2006. **11**(3): p. 33001.
7. Themelis, G., J.S. Yoo, and V. Ntziachristos, *Multispectral imaging using multiple-bandpass filters.* Opt Lett, 2008. **33**: p. 1023-1025.
8. Tsurui, H., et al., *Seven-color fluorescence imaging of tissue samples based on Fourier spectroscopy and singular value decomposition.* J Histochem Cytochem, 2000. **48**(5): p. 653-62.
9. Ntziachristos, V., et al., *In vivo tomographic imaging of near-infrared fluorescent probes.* Molecular Imaging, 2002. **1**: p. 82 - 88.
10. Ntziachristos, V., *Fluorescence molecular imaging.* Annu Rev Biomed Eng, 2006. **8**: p. 1-33.
11. Ntziachristos, V., C. Bremer, and R. Weissleder, *Fluorescence imaging with near-infrared light: new technological advances that enable in vivo molecular imaging.* Eur Radiol, 2003. **13**(1): p. 195-208.
12. Weissleder, R. and U. Mahmood, *Molecular imaging.* Radiology, 2001. **219**(2): p. 316-33.
13. Popescu, G. and A. Dogariu, *Optical path-length spectroscopy of wave propagation in random media.* Opt Lett, 1999. **24**(7): p. 442-4.
14. Chang, J.H., H.L. Graber, and R.L. Barbour, *Imaging of fluorescence in highly scattering media.* IEEE Trans. Biomed. Eng., 1997. **44**: p. 810-822.
15. Aronson, R. and N. Corngold, *Photon diffusion coefficient in an absorbing medium.* J. Opt. Soc. Am. A, 1999. **16**: p. 1066-1071.
16. Corlu, A., et al., *Diffuse optical tomography with spectral constraints and wavelength optimization.* Appl Opt, 2005. **44**(11): p. 2082-93.
17. Culver, J.P., et al., *Three-dimensional diffuse optical tomography in the parallel plane transmission geometry: evaluation of a hybrid frequency domain/continuous wave clinical system for breast imaging.* Med Phys, 2003. **30**(2): p. 235-47.
18. Ripoll, J., et al., *The Kirchhoff approximation for diffusive waves.* Phys. Rev. E, 2001. **64**: p. 051917.
19. Oleary, M.A., et al., *Fluorescence lifetime imaging in turbid media.* OPt. Lett., 1996. **21**: p. 158-160.
20. Aronson, R., *Boundary conditions for the diffusion of light.* J. Opt. Soc. Am. A, 1995. **12**: p. 2532-2539.

21. Ntziachristos, V. and R. Weissleder, *Experimental three-dimensional fluorescence reconstruction of diffuse media using a normalized Born approximation.* Opt. Lett., 2001. **26**: p. 893-895.
22. Kak, C. and M. Slaney, *Principles of Computerized Tomographic Imaging*. 1988, New York: IEEE.
23. Zimmermann, T., *Spectral imaging and linear unmixing in light microscopy.* Adv Biochem Eng Biotechnol, 2005. **95**: p. 245-65.
24. Dickinson, M.E., et al., *Multi-spectral imaging and linear unmixing add a whole new dimension to laser scanning fluorescence microscopy.* Biotechniques, 2001. **31**(6): p. 1272, 1274-6, 1278.
25. Garini, Y., I.T. Young, and G. McNamara, *Spectral imaging: principles and applications.* Cytometry A, 2006. **69**(8): p. 735-47.
26. Swartling, J., et al., *Fluorescence spectra provide information on the depth of fluorescent lesions in tissue.* Appl Opt, 2005. **44**(10): p. 1934-41.
27. Srinivasan, S., et al., *Spectrally constrained chromophore and scattering near-infrared tomography provides quantitative and robust reconstruction.* Appl Opt, 2005. **44**(10): p. 1858-69.
28. Dehghani, H., et al., *Three-dimensional optical tomography: resolution in small-object imaging.* Appl Opt, 2003. **42**(16): p. 3117-28.
29. Stelios, P., *Χαρακτηρισμός της ευαισθησίας και ποσοτικοποίηση της Τομογραφίας Φθορισμού*, in *Μ.Π.Σ Μικροηλεκτρονικής- Οπτοηλεκτρονικής*. 2008, Πανεπιστήμιο Κρητής: Ηράκλειο.
30. www.invitrogen.com/site/us/en/home/References/Molecular-Probes-The-Handbook/Antibodies-Avidins-Lectins-and-Related-Products/Secondary-Immunoreagents.html
31…….www.atto-tec.com/attotecshop/product_info.php?info=p105_ATTO-590.html&XTCsid=fjf68akjee4bkuhpn91eca4n45
32. www.andor.com/spectrographs/czerny-turner_spectrographs/

Appendix

A1) Deconvolution of experimental spectra

As we can see in Figure 1, index (a) and (b) indicate the mixed fluorescence spectrum at 488nm and 514nm respectively. Index (c) and (e) represent the deconvolved spectrum for CFSE and ATTO590 with illumination at 488nm. In a similar way, index (d) and (f) shows the deconvolved spectrum for CFSE and ATTO590 at 514nm illumination.

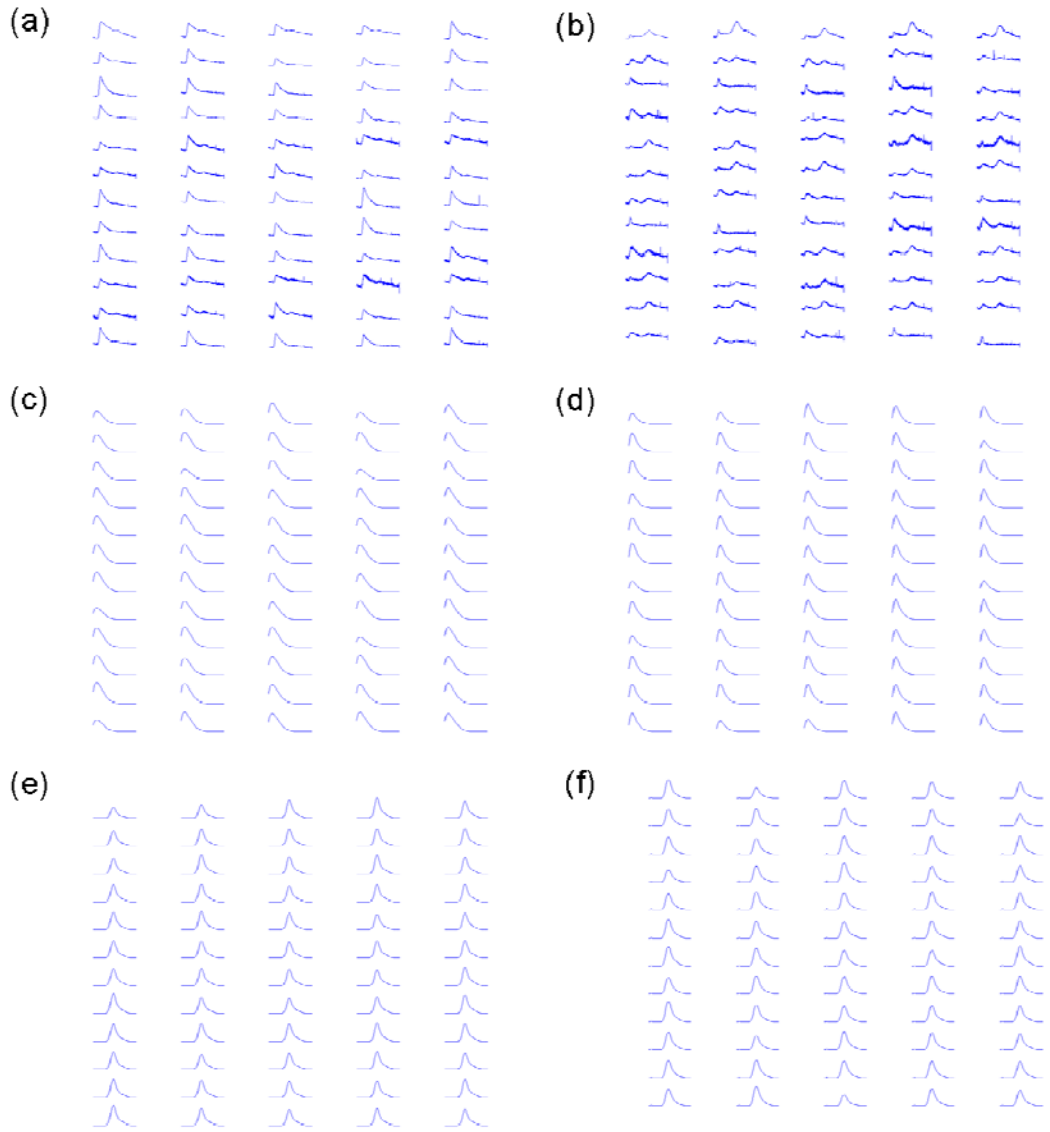

Figure 1 Spectra Deconvolution for 4µM CFSE and 5µM Atto590

A2) Source-by-source spectra of CFSE+Atto590 in four positions

In the following figures, we can see the results for two tubes filled with the same concentration of CFSE and ATTO590. Figure 2 shows the spectra for the four positions after excitation with the 514nm laser in the reflection geometry. Figure 3 represents the spectral results after excitation with the 488nm laser again in the reflection geometry. Figures 4 and 5 are from transmission geometry, and represent the spectral results for the different position with the excitation from the 514nm laser and 488nm laser respectively. In all figures the indices represent the different position of the two tubes. Index (a) corresponds to a distance of 1mm and a 3mm depth from the surface of the sample, index (b) to a distance of 4mm and a depth of 3mm. Index (c) shows the results for 6mm depth under the surface of the phantom and 1mm distance, and finally in index (d) the tubes are also in 6mm under the surface of the sample but the distance between the two tubes was 4mm.

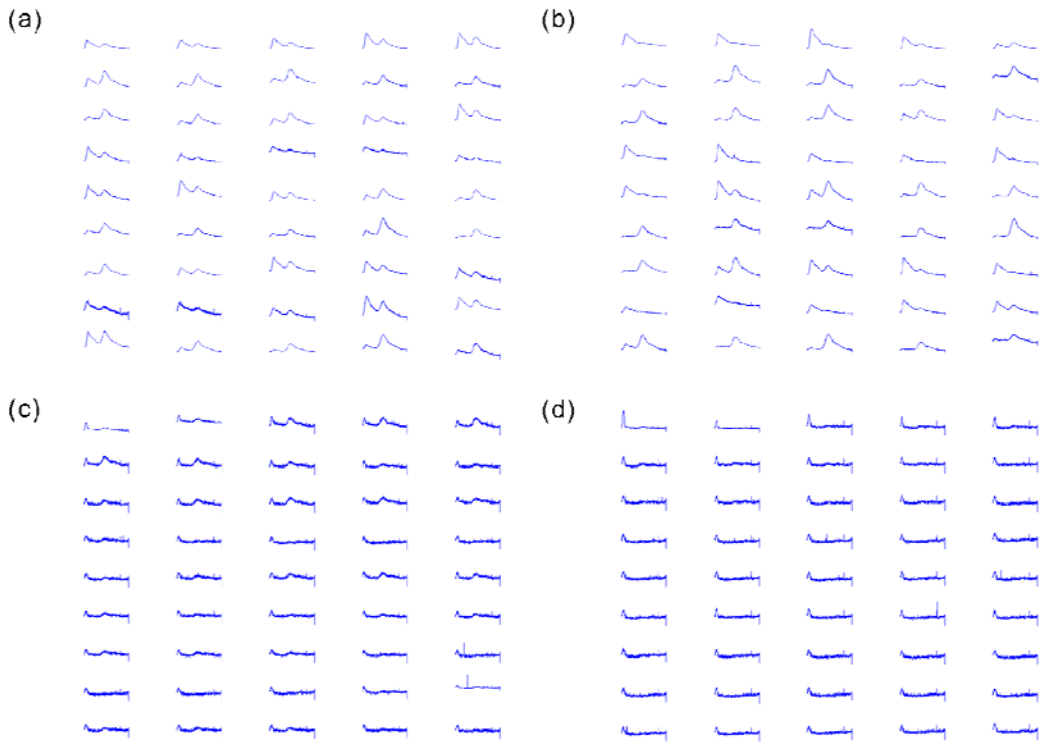

Figure 2 Reflection for 514nm laser

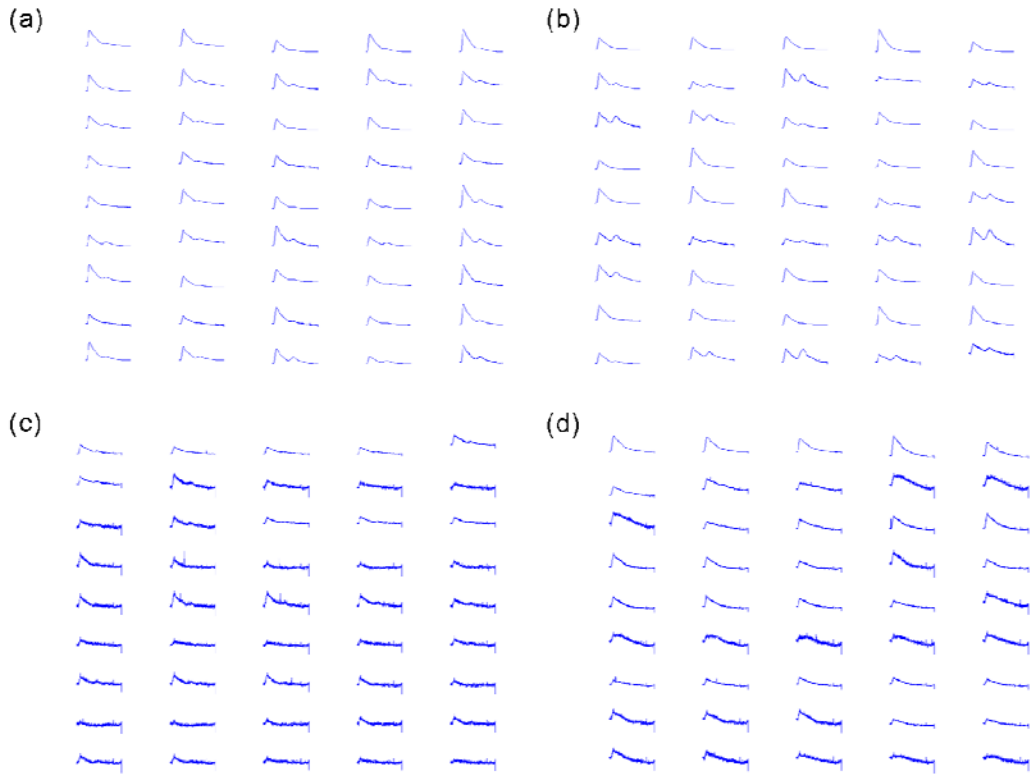

Figure 3 Reflection for 488nm laser

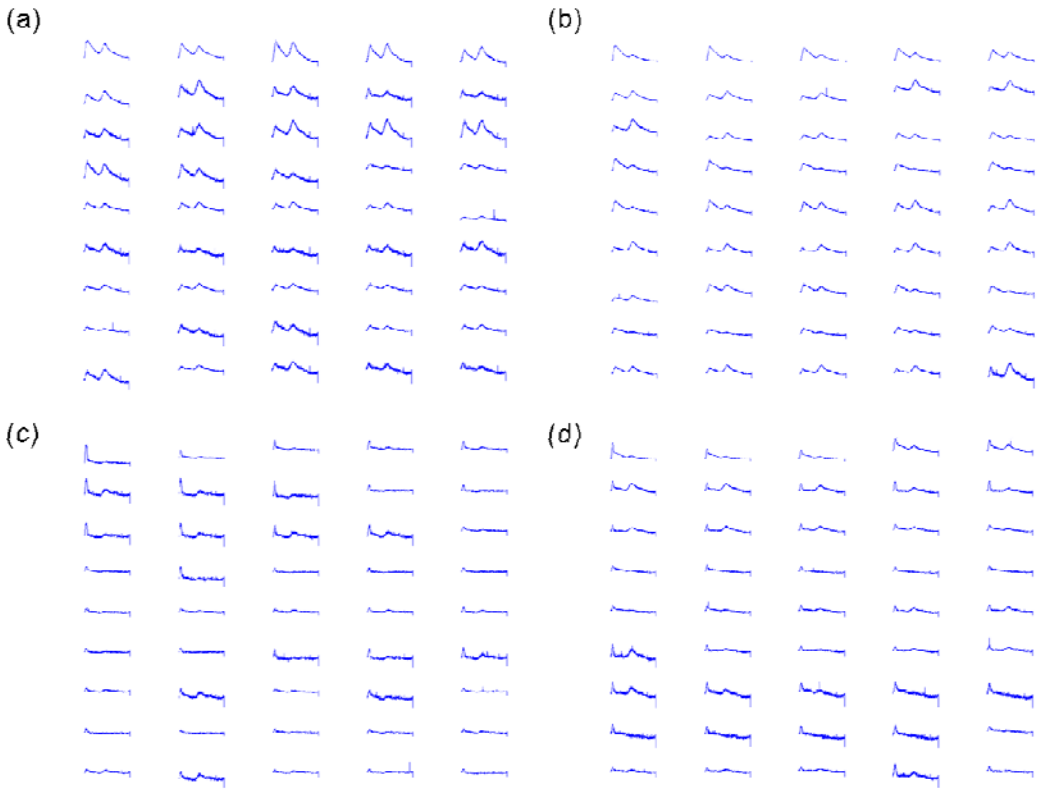

Figure 4 Transmission for 514nm laser

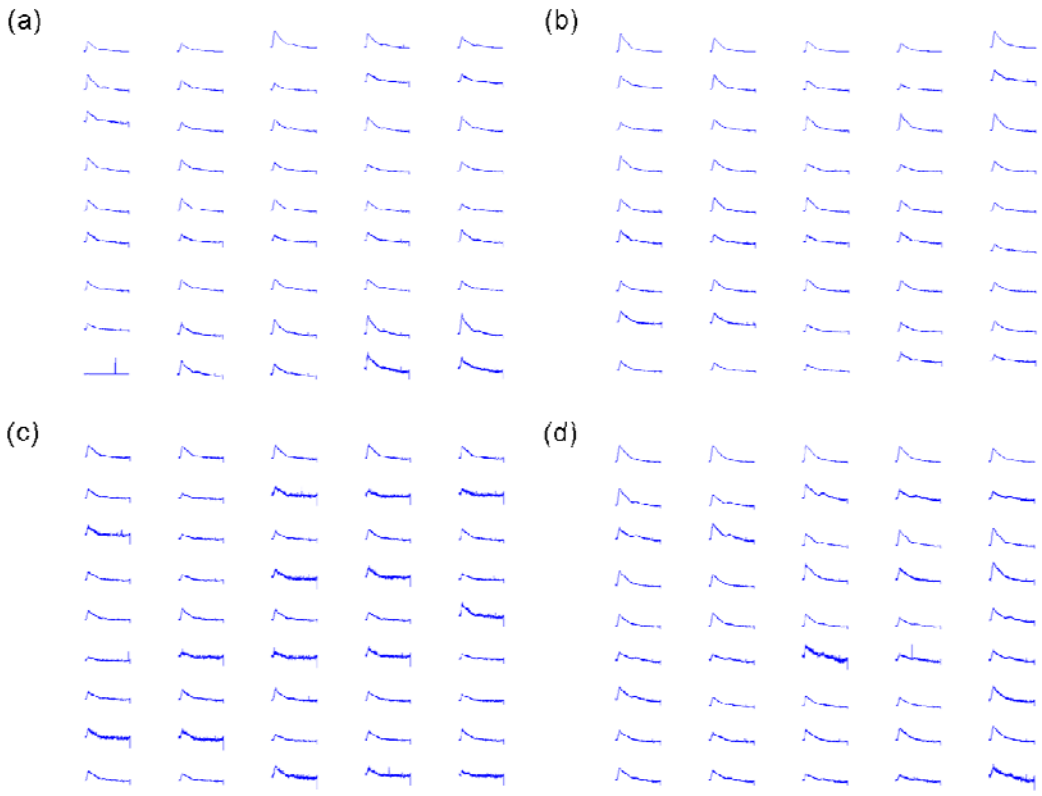

Figure 5 Transmission for 488nm laser.

A3) Source-by-source spectra of CFSE in four positions

The following pictures show spectra from two tubes with the same concentration of CFSE. Figure 6 shows the spectra for the four positions after excitation with the 488nm laser in the reflection geometry while Figure 7 shows the corresponding spectra for the transmission geometry. In both cases, the different indices represent the different position of the two tubes. Therefore, index (a) corresponds to 1mm distance and 3mm depth from the surface of the sample. Index (b) corresponds to a distance of 4mm and depth of 3mm. Index (c) shows the results for 6mm depth under the surface of the phantom and 1mm distance between the two fluorophores, and finally in index (d) the tubes are also in 6mm under the surface of the sample but the distance between them was 4mm.

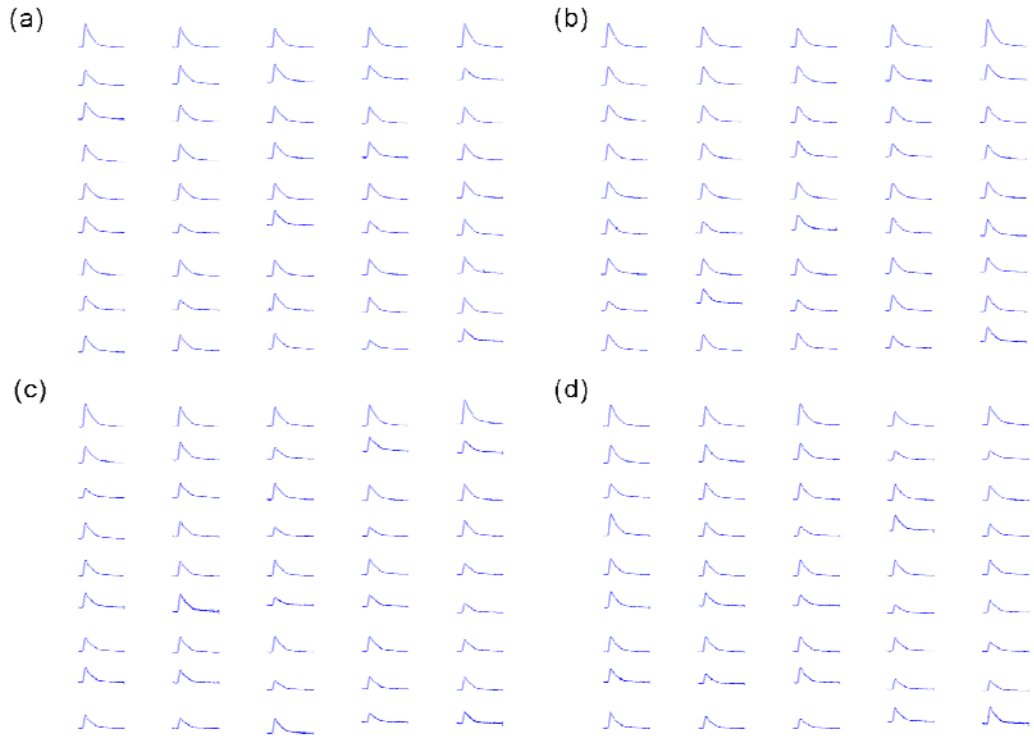

Figure 6 tubes of CFSE in reflection geometry

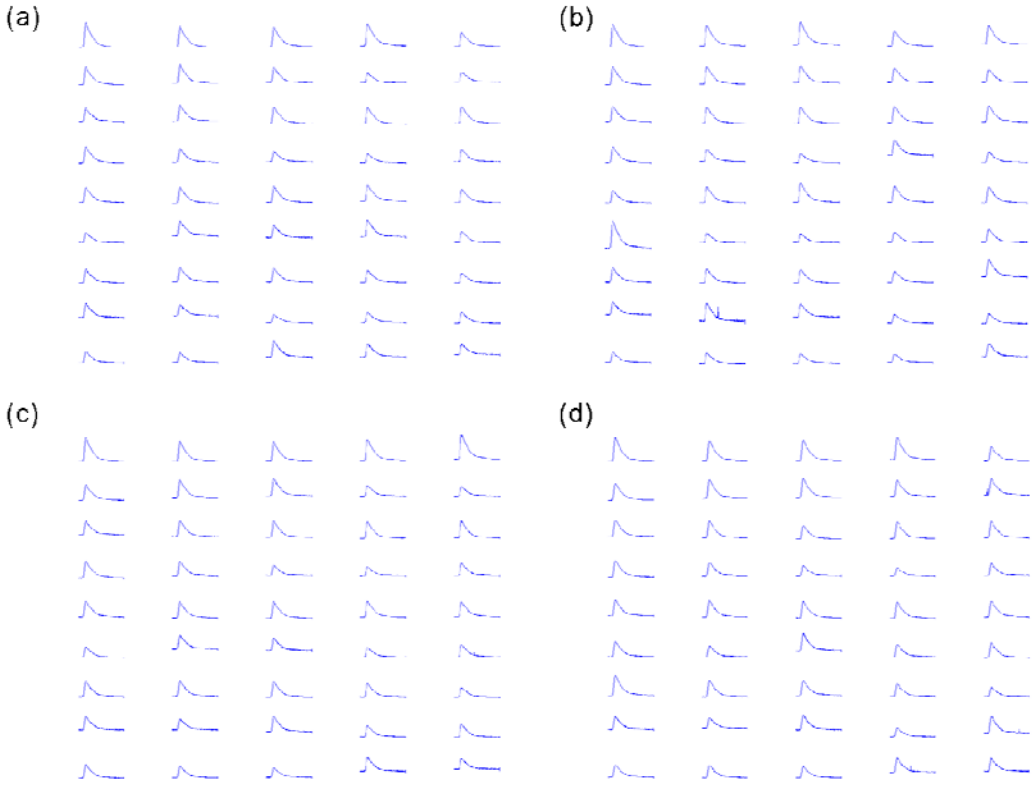

Figure 7 tubes of CFSE in transmission geometry

A4) Source-by-source spectra of CFSE and Atto590 in the same position

In this part we can see the results for both tubes filled with different fluorophore and put in the same position, but different depth under the surface of the phantom. The results are seeing in Figure 8 were index (a) and (c) correspond to the 488nm laser, index (a) for the reflection geometry and index (c) for the transmission geometry. In a similar way, indices (b) and (d) are for the excitation with the 514nm laser, (b) for reflection and (d) for transmission.

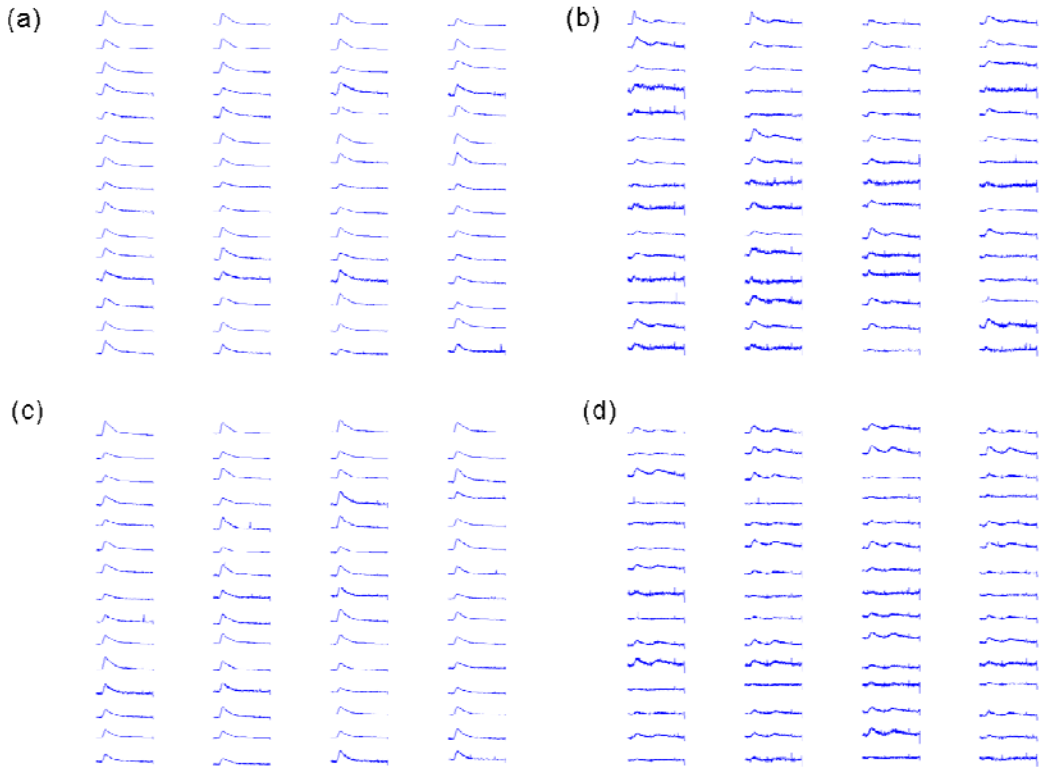

Figure 8 Tubes in the same position

A5) CFSE and Atto590 phantom experiments

In this part we can see the results for the phantom experiments involving CFSE and ATTO590. For all figures, (a) and (b) show the reconstructions of the two fluorophores before the unmixing for the green and red detection channel respectively. (c) and (d) show the reconstruction results after UnmixRec (see Chapter 4) using the fixed spectral strengths for the green and red detection channels respectively. (e) and (f) represent the results for the UnmixRec using the mean deconvolved spectral strengths for the green and red detection channels respectively. (g) and (h) show the results after UnmixData using the fixed spectral strengths for the green and red channels respectively. Finally, (j) and (i) represent the unmixing after UnmixData using the mean deconvolved spectral strengths for the green and red channels respectively.

- **illumination at 514nm in reflection geometry**

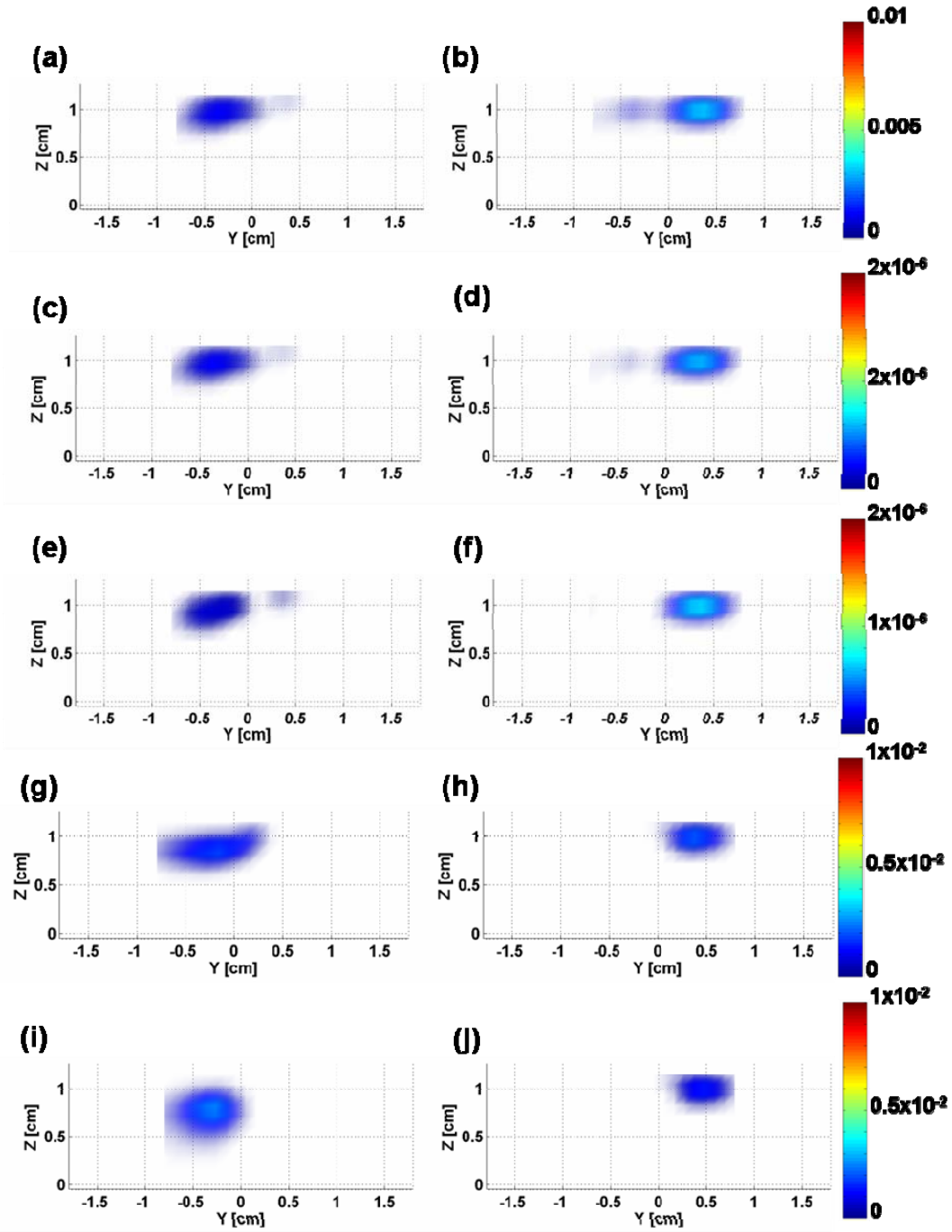

Figure 9 Reconstructions at 514nm in the reflection geometry for 4µM CFSE and 10µM Atto590.

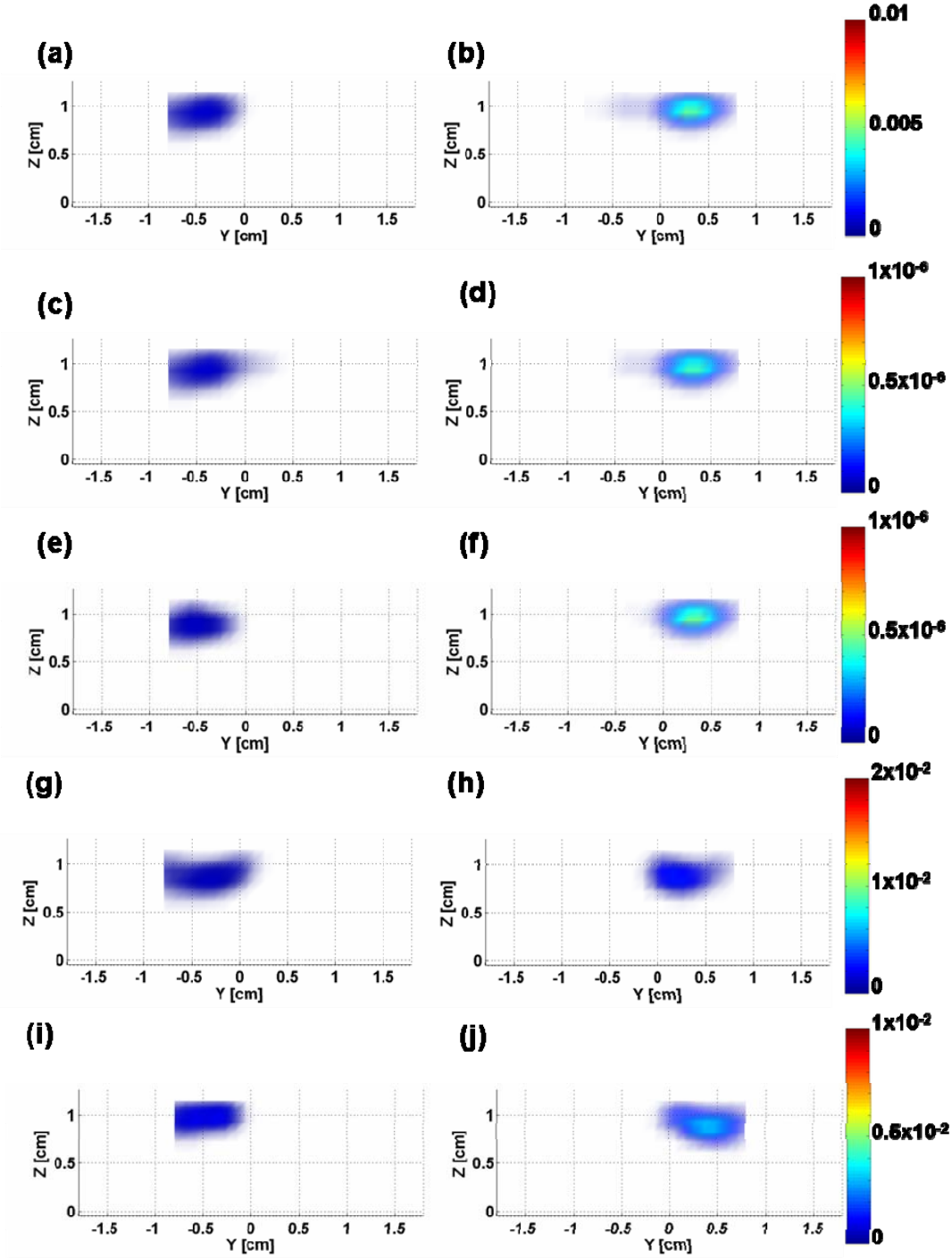

Figure10 Reconstructions at 514nm in the reflection geometry for 4μM CFSE and 15μM Atto590

- **illumination at 488nm in reflection geometry**

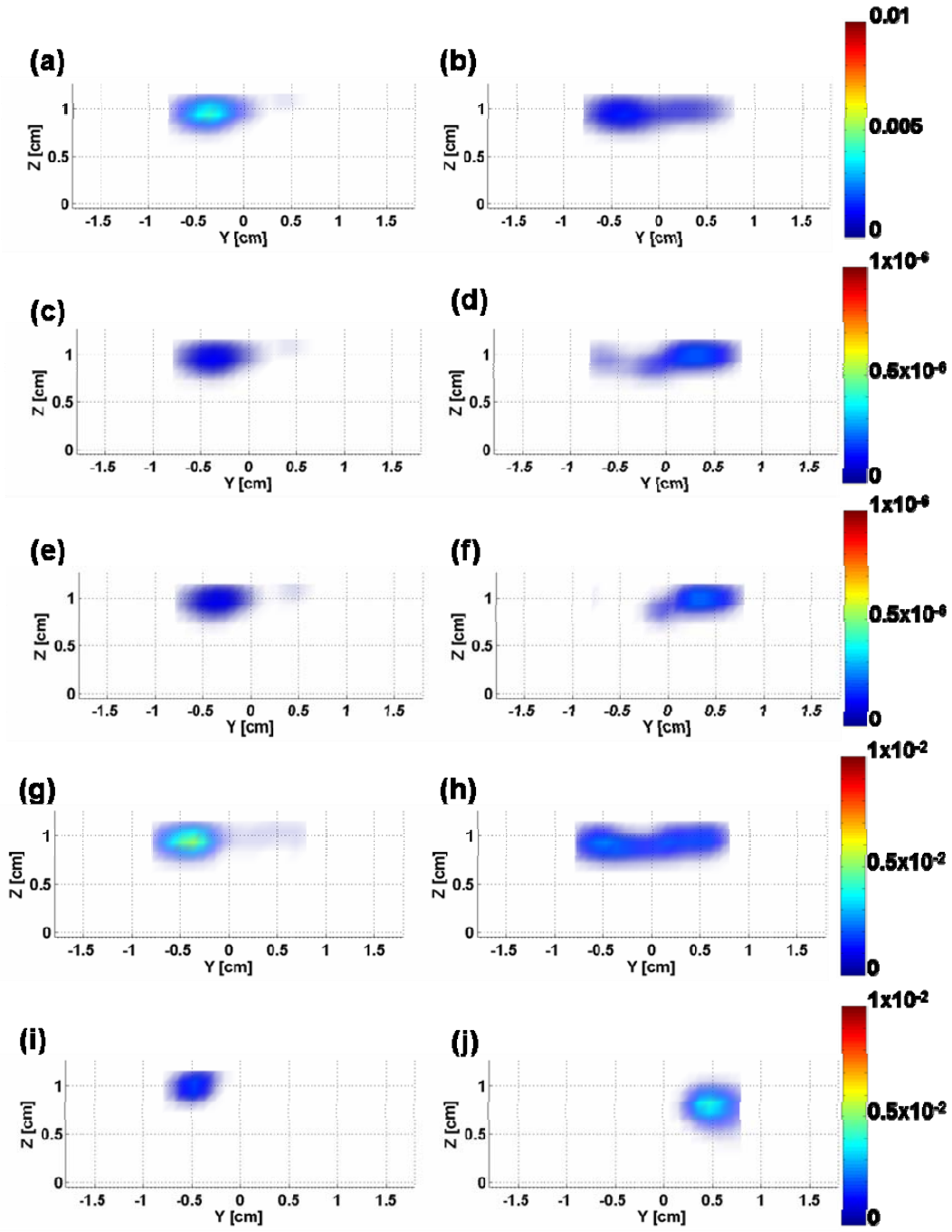

Figure 11 Reconstructions at 488nm in the reflection geometry for 4μM CFSE and 10μM Atto590.

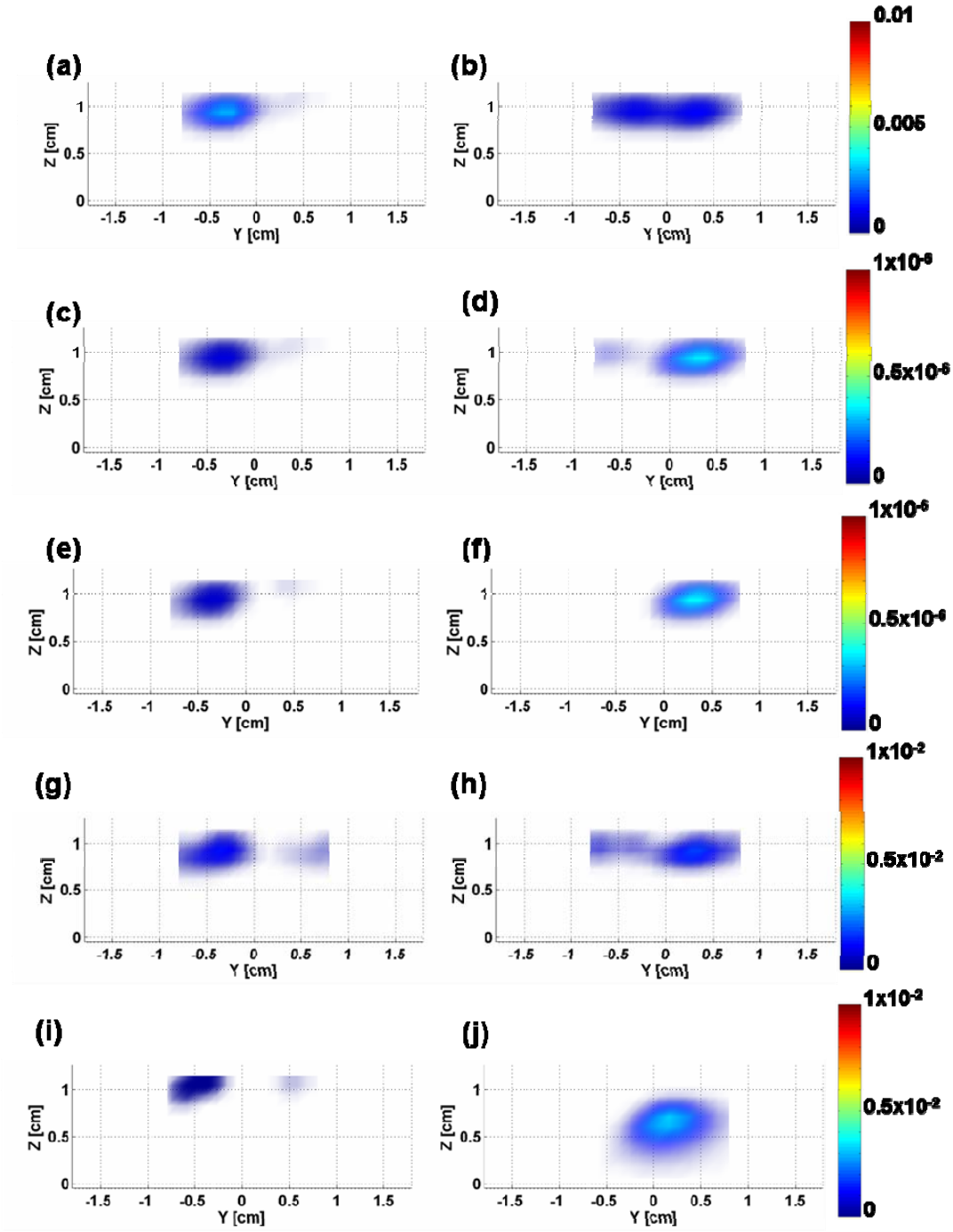

Figure 12 Reconstructions at 488nm in the reflection geometry for 4μM CFSE and 15μM Atto590.

- **illumination at 514nm in transmission geometry**

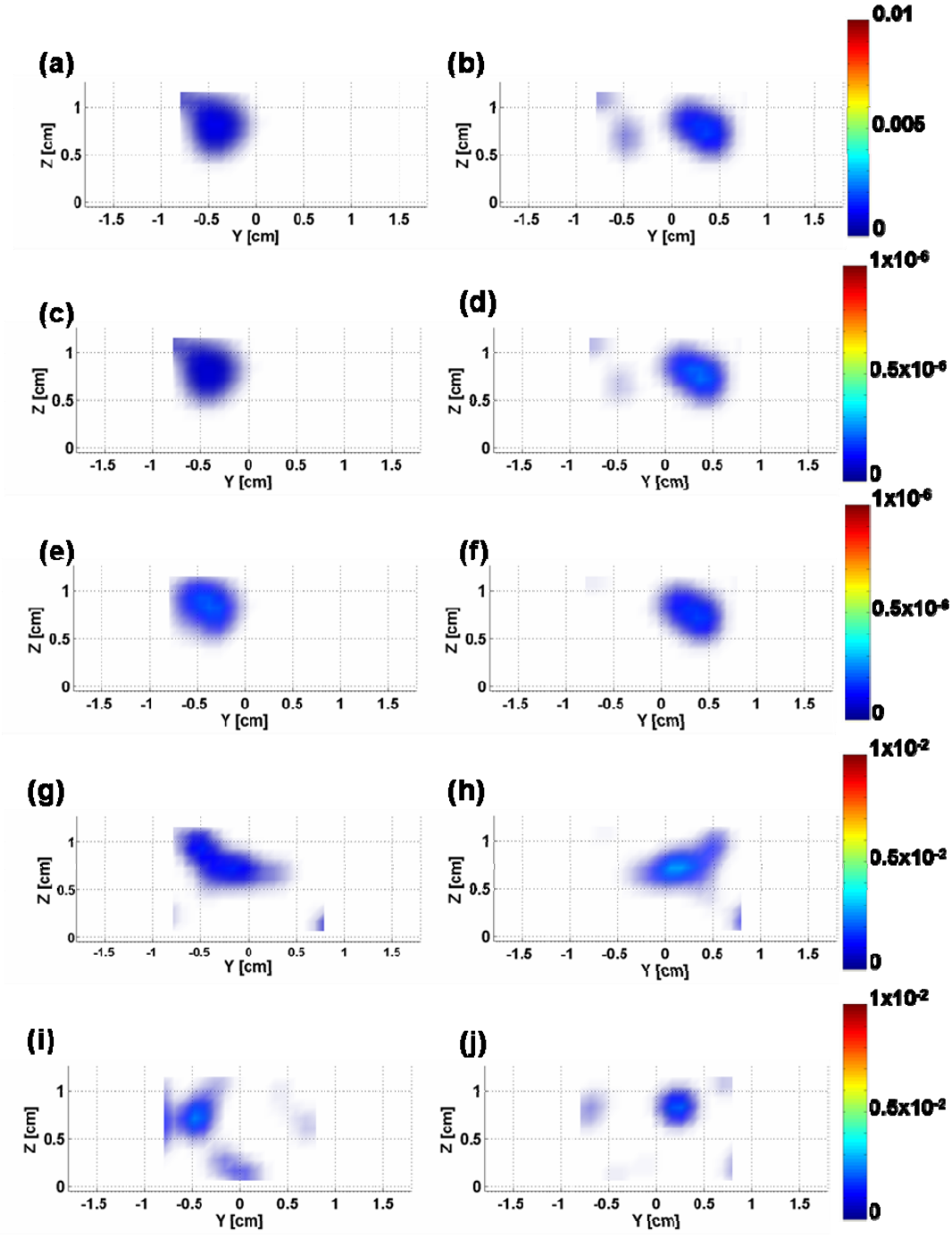

Figure 13 Reconstructions at 514nm in the transmission geometry for 4μM CFSE and 10μM Atto590.

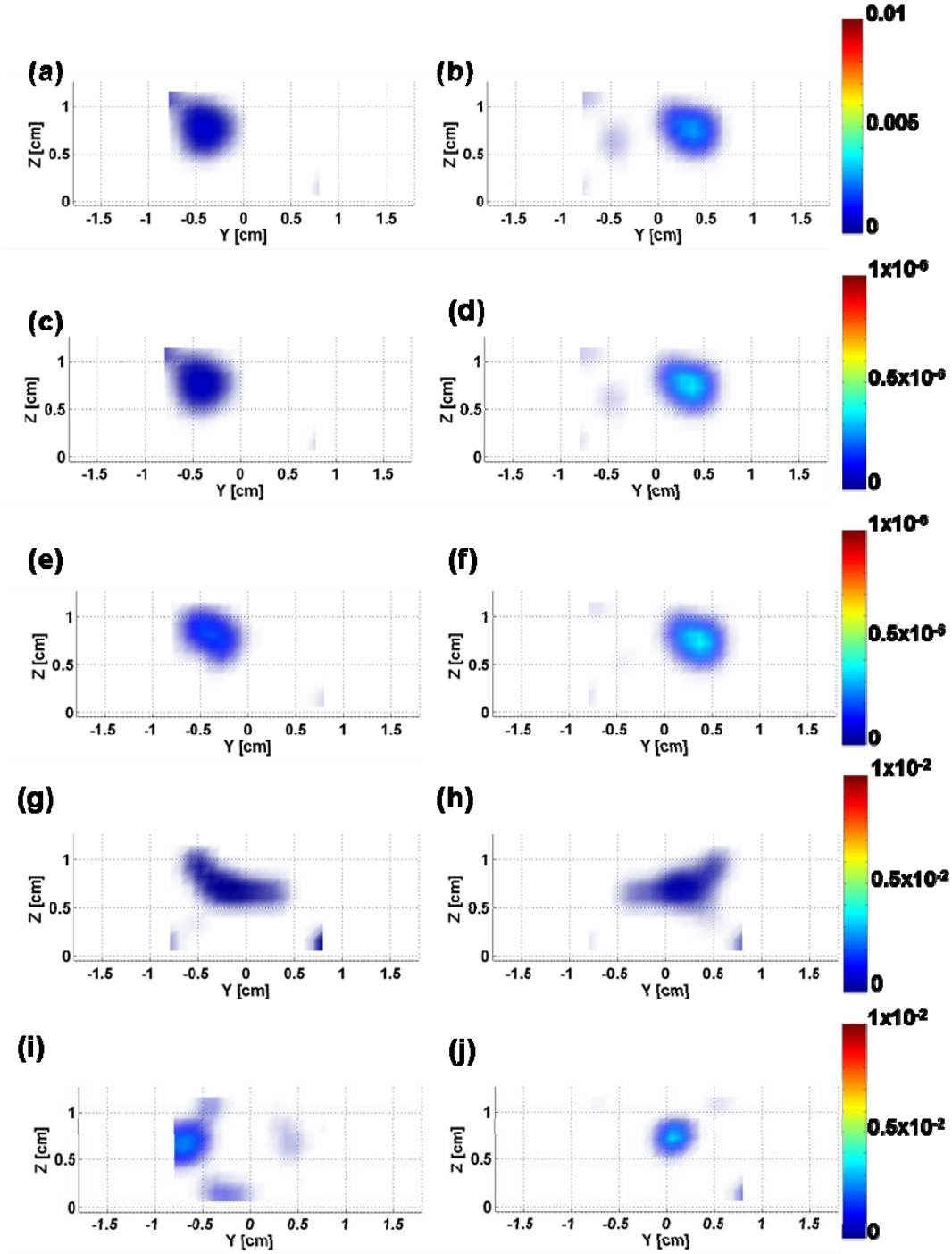

Figure 14 Reconstructions at 514nm in the transmission geometry for 4μM CFSE and 15μM Atto590.

- **illumination at 488nm in transmission geometry**

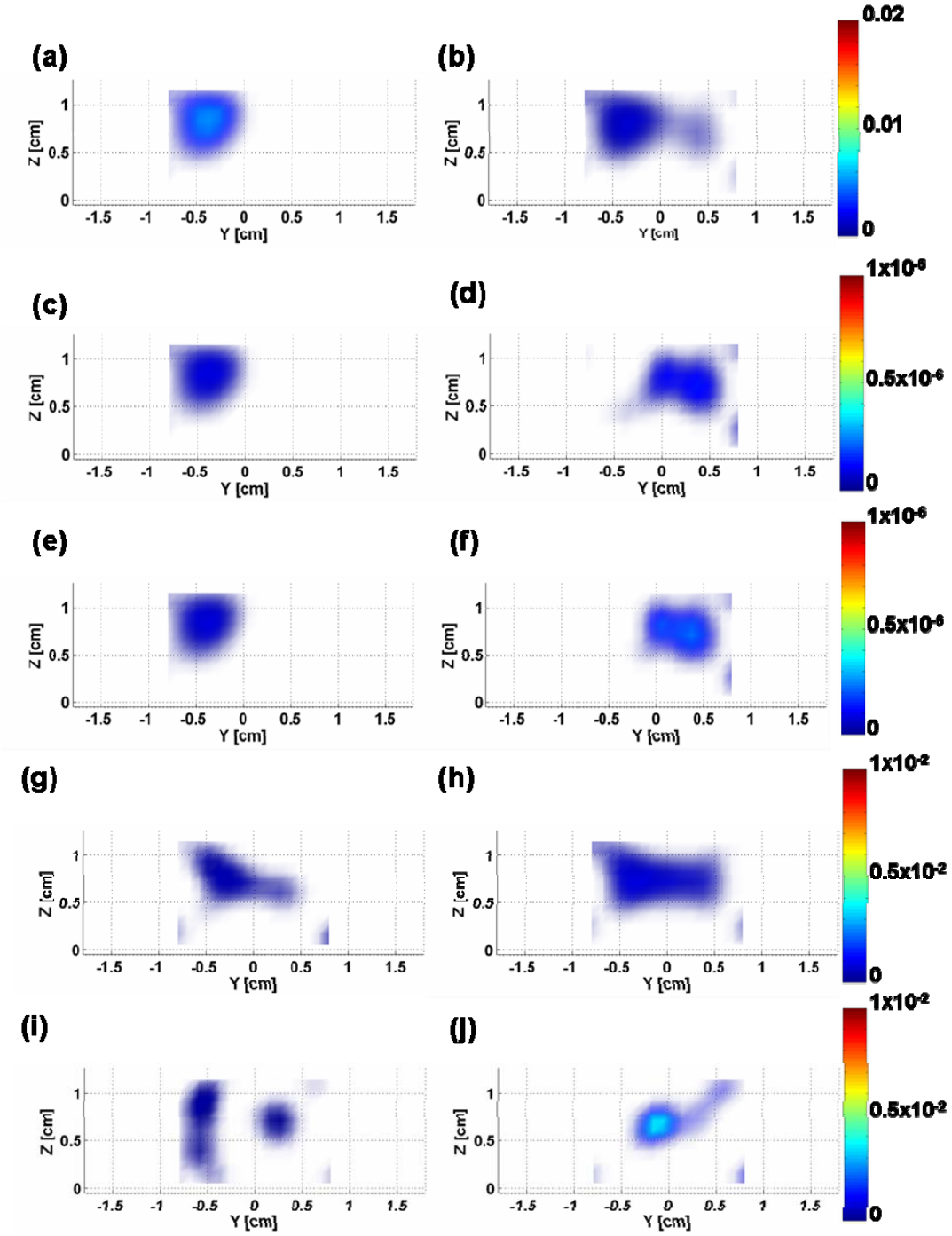

Figure 15 Reconstructions at 488nm in the transmission geometry for 4µM CFSE and 10µM Atto590.

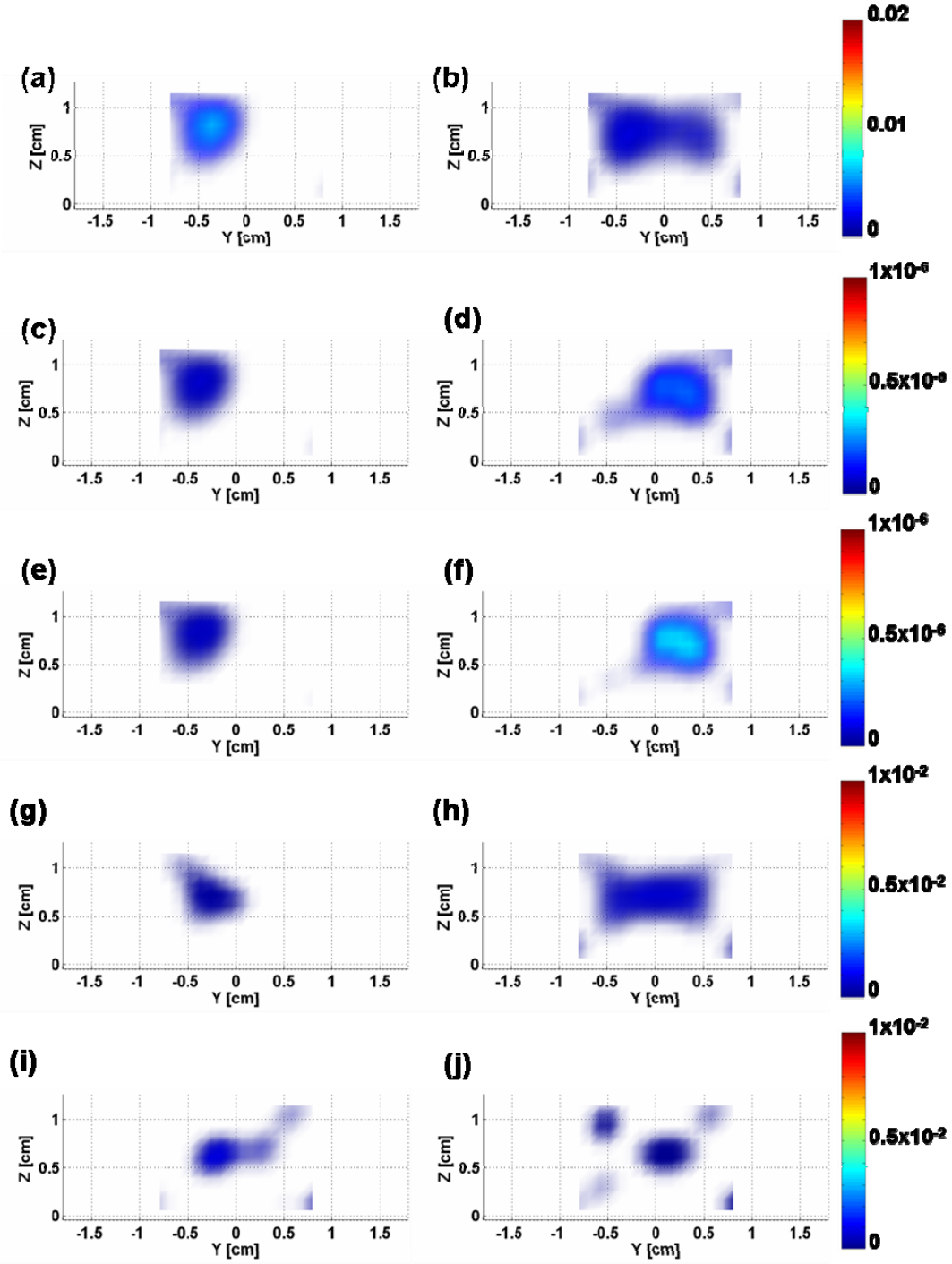

Figure 16 Reconstructions at 488nm in the transmission geometry for 4μM CFSE and 15μM Atto590.

A6) CFSE and Atto590 in vivo experiments

In this part we can see the results for the in vivo experiment with the subcutaneously injected tubes with CFSE and ATTO590. Again, in picture (a) and (b) we can see the reconstructions of the two fluorophores before the unmixing processing where in picture (a) is the signal from the green detection channel and in picture (b) is the signal from the red detection channel. Pictures (c) and (d) show the reconstruction results after the unmixing in the raw data using the fix matrix of spectral strengths. In picture (c) we see the results from the green detection channel and in picture (d) the results from the red detection channel. Pictures (e) and (f) represent the results for the unmixing in the raw data by using the mean matrix of spectral strengths, where picture (e) is again from the green detection channel and picture (f) is for the red detection channel. The next two pictures, (g) and (h) show the results after the unmixing processing in the reconstruction data using the fix matrix of spectral strengths; (g) and (h) are the green and red channel of detection respectively. In an analogous way, pictures (j) and (i) represent the unmixing processing in the reconstructed data with the mean weights of spectral strength, (i) for the green detection channel and (j) for the red one. Next four pictures (k), (l), (m) and (n) show the unmixing in the reconstructed data after the autofluorescence signal has been removed. Picture (k) corresponds to the green detection channel and picture (l) to the red one, while in the unmixing algorithm we have used the fix matrix of spectral strengths.

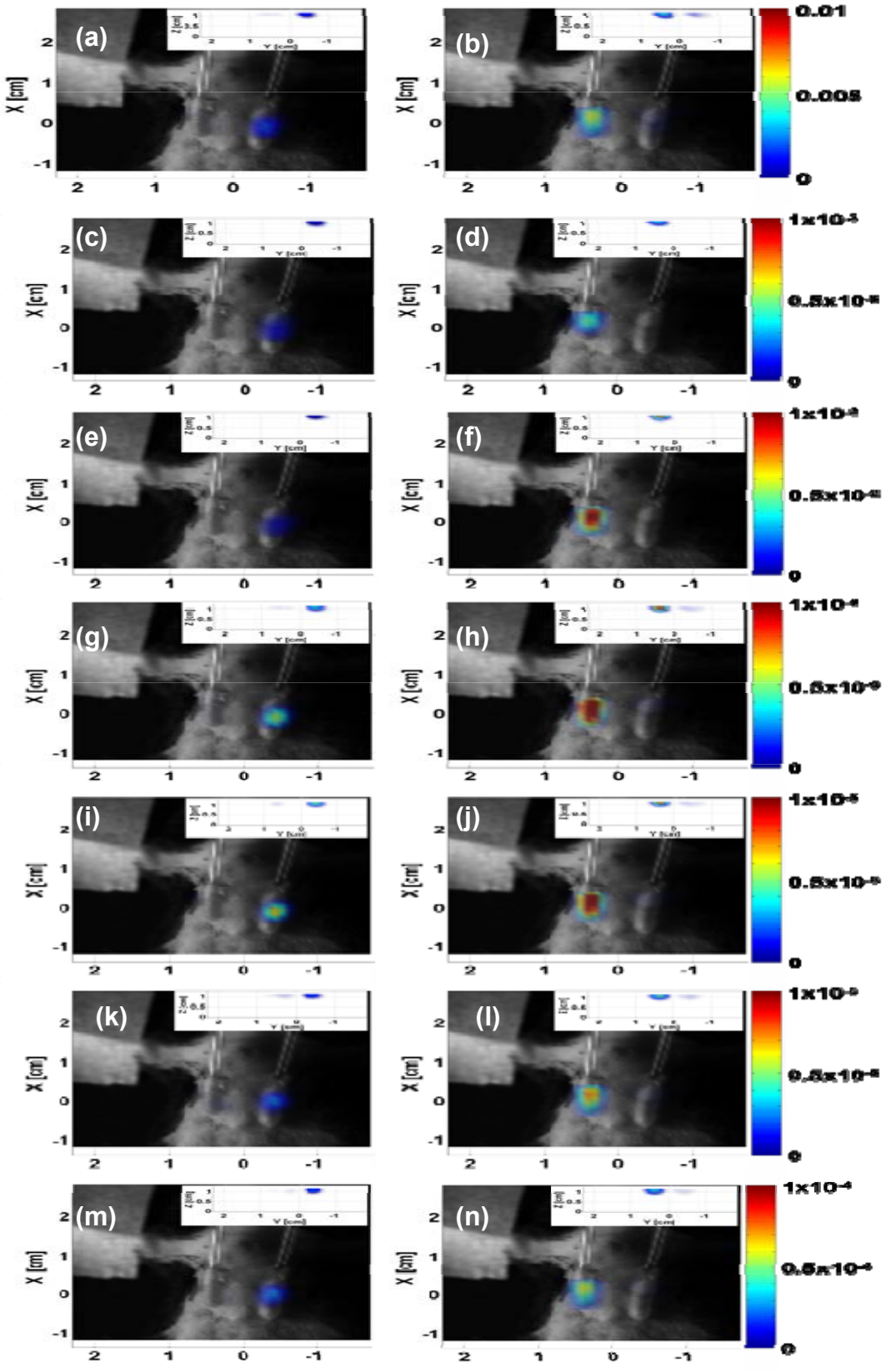

Figure 17 Illumination at 514nm, 4μM CFSE and 10μM Atto590

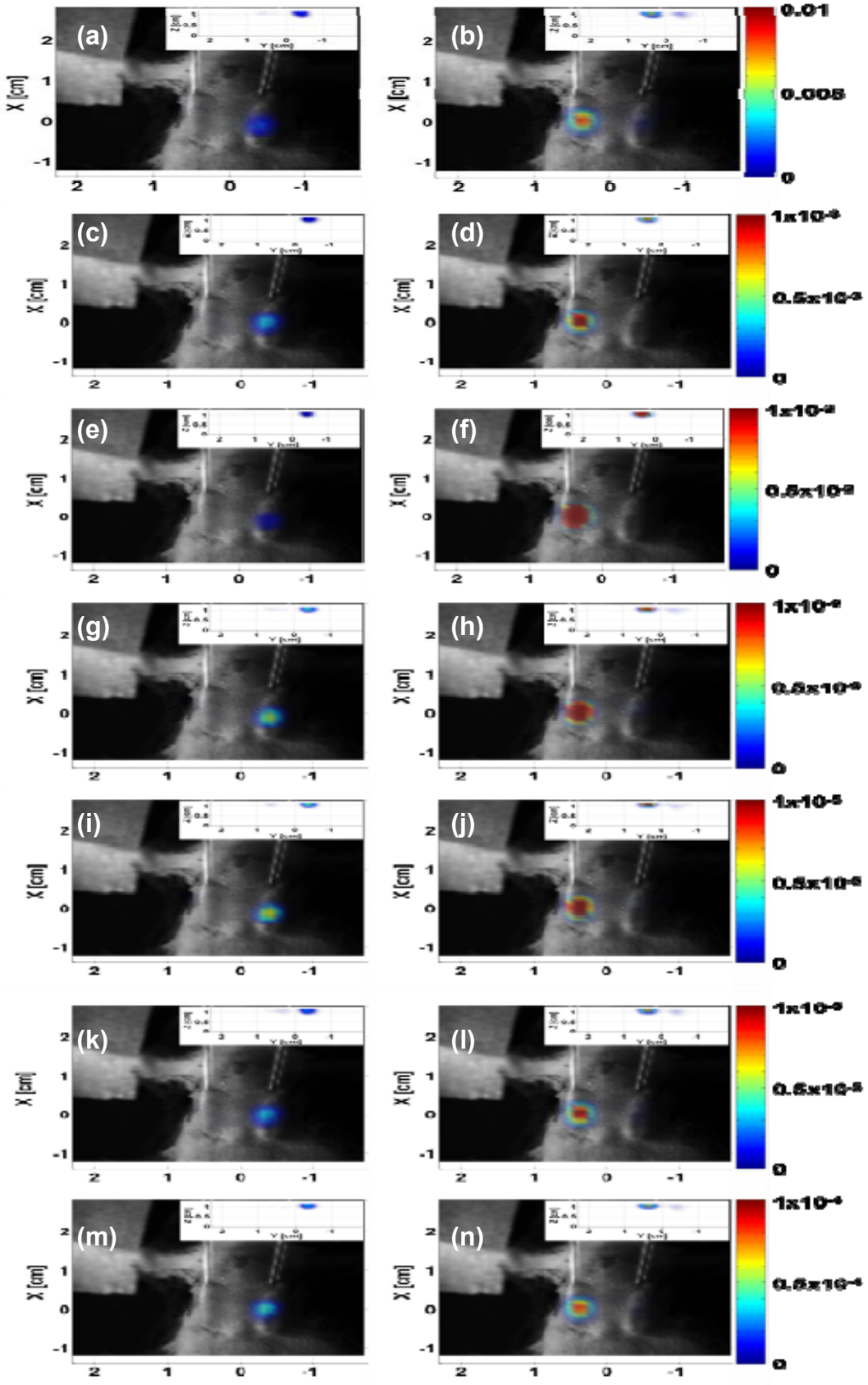

Figure 18 illumination at 514nm, 4μM CFSE and 15μM Atto590

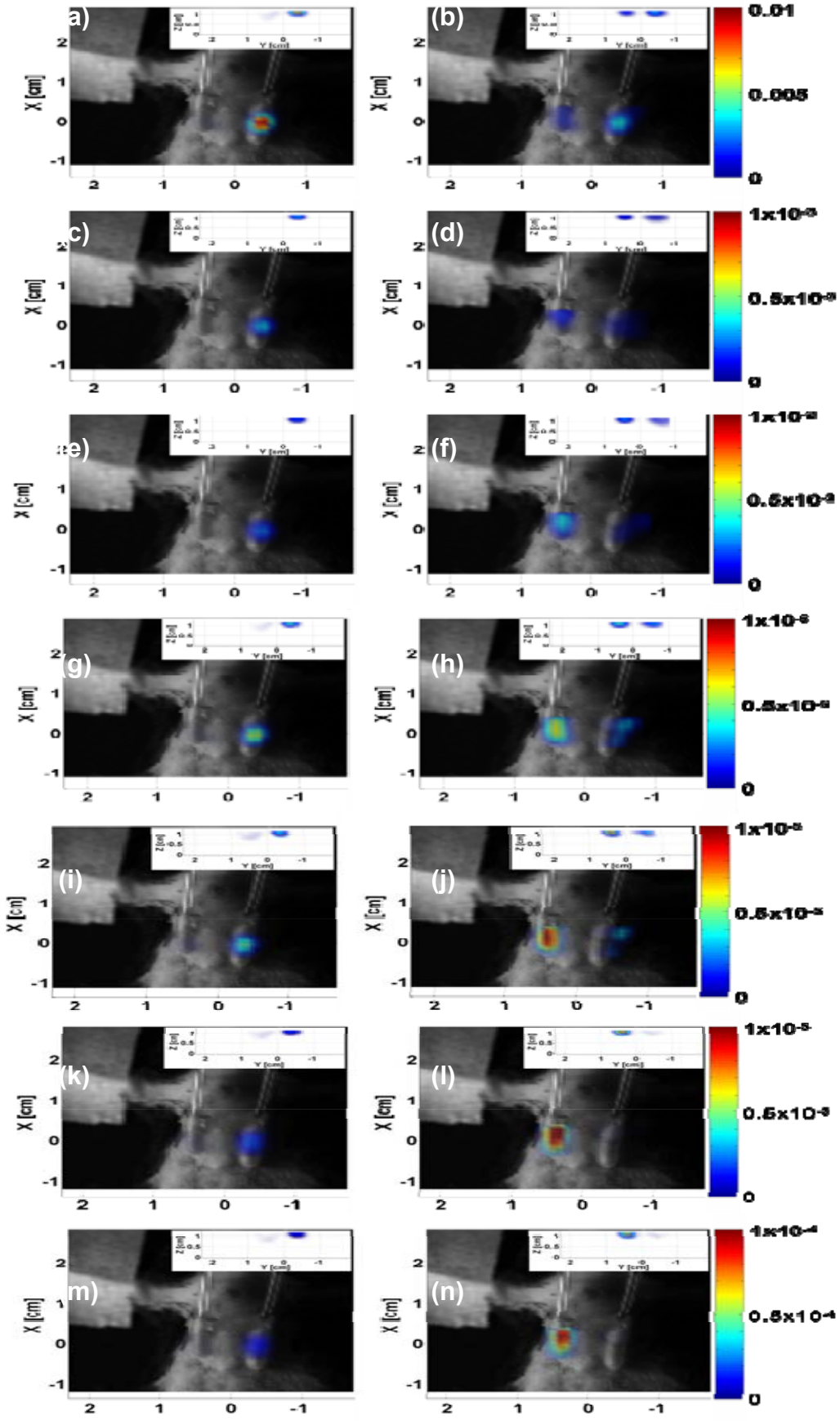

Figure 19 illumination at 488nm, 4μM CFSE and 10μM Atto590

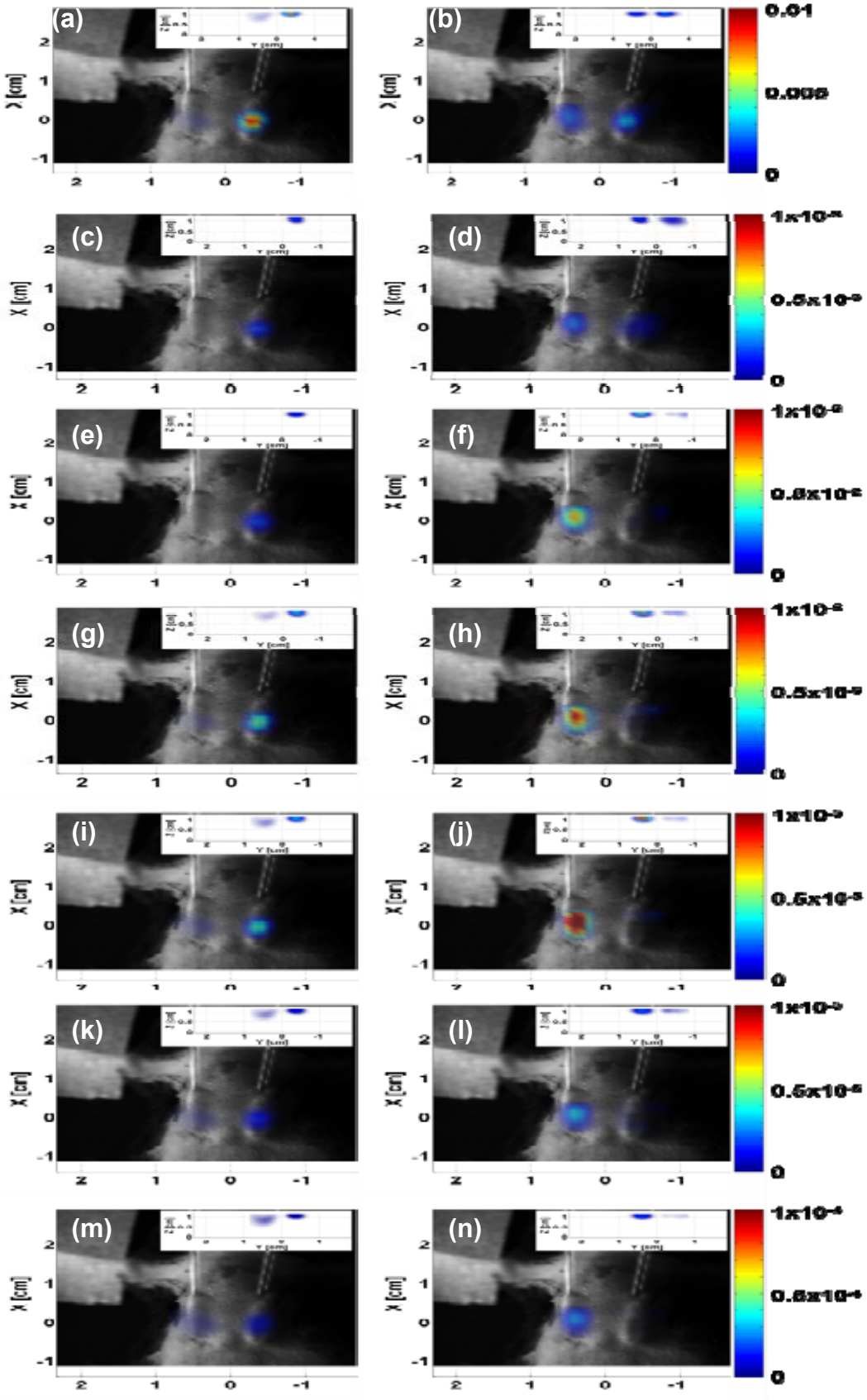

Figure 20 illumination at 488nm, 4µM CFSE and 15µM Atto590